Dissertation

Lipid Hydrolysis in Cancer Metabolism

submitted by

Sophie Elisabeth HONEDER

BSc., MSc.

for the Academic Degree of

Doctor of Philosophy

(PhD)

at the

Medical University of Graz

Diagnostic and Research Institute of Pathology

under the Supervision of

Univ. Prof. Dipl.-Ing. Dr. techn. Ruth Birner-Grünberger

2023

Statutory Declaration

I hereby declare that this thesis is my own original work and that I fully acknowledge by name all those individuals and organizations that have contributed to the research for this thesis. Due acknowledgment has been made in the text to all other material used. Throughout this thesis and in all related publications, I followed the guidelines of “Good Scientific Practice and Ombuds Committee at the Medical University of Graz”.

Wien, November 2023 _____

Sophie Elisabeth Honeder

Disclosures

This thesis is divided into two chapters, which are preceded by a common introduction to (lung) cancer, cancer metabolism, and lipid hydrolysis. The first chapter summarizes work on lung cancer cell lines deficient in intracellular lipolysis, which is - in part - published in Honeder S., et al. "Adipose Triglyceride Lipase Loss Promotes a Metabolic Switch in A549 Non–Small Cell Lung Cancer Cell Spheroids" in Molecular and Cellular Proteomics (2021) (1). The second chapter is focused on results from bioanalytical analyses of paired tumor and normal-tumor adjacent tissue derived from lung cancer patients.

Additionally, my contribution to several publications can be viewed in the following co-authorships (2, 3, 4, 5, 6, 7, 8, 9).

All co-authors whose work contributed to this thesis have given their consent about the use of their data in this thesis.

All figures sourced or adapted from other publications are subject to the Creative Commons license CC BY 4.0[1], permitting the utilization of the content for any purpose in compliance with the publisher's guidelines. Appropriate attribution for specific figures is provided within the respective figure legends.

Funding

This research was funded by the Austrian Science Fund FWF (grant numbers W1226 (Doktoral School "DK-Metabolic and Cardiovascular Disease") and F73 (SFB "Lipid Hydrolysis")), and by the Marshall Plan Foundation (Marshall Plan Foundation Scholarship 2022/23), and by the Austrian Agency for Education and Internationalisation OeAD (Marietta Blau Scholarship 2022/23).

[1] https://creativecommons.org/licenses/by/4.0/

Acknowledgments

First and foremost, I want to express my deepest gratitude to Ruth for her invaluable guidance and enduring support throughout this journey, and for believing in my abilities and putting her trust in me. Despite running two labs at once and a global pandemic that caused some difficulties in the past years, she has never failed to provide stability and guidance for all of us, and I am proud to be a part of her crew, the Proteomics Pirates.

I would also like to express my immense gratitude to the current and former crew members of the Proteomics Pirates without whom I could not have succeeded in this journey. Special thanks are owed to Tam for the constant support and expertise with pretty much anything, but more importantly, thank you for being a true role model and friend. To Matthias, thank you for your valuable scientific input and for keeping the lab running with your MS knowledge and great ideas. Thank you, Laura and Babsi, for being there from the beginning, for your kind way of teaching me your ways around the lab and introduction to proteomics, and for being great colleagues. Thanks to Stefan for always helping me with instrument questions, and for managing to fix all the broken instruments. I am also thankful for all the help with experimental work that Jürgen has provided over the years, especially considering his microscopy skills. I am very grateful for my peer Max, who has brightened up the lab with his personality and jokes; you were a great colleague to share a large portion of this journey with. I also want to express my gratitude to all the newer lab members in Vienna: Vici, thanks for helping with any bureaucratic task and anything TU-related, and for making our lab feel a bit more like home with your delicious food. Thank you, Isa, for always being so kind and helpful with any chromatography and MS-related questions, and for being a great lab mate and friend. Finally, thank you, Julia, Dominik, and Raphi for being great colleagues and friends and for all the fun times in and out of the lab.

My sincere gratitude extends to Matt Vander Heiden and his whole research group at the Koch Institute at MIT for amicably hosting me in their lab for almost a whole year. It was a truly incredible experience that helped me grow both personally and professionally. I am especially grateful for the welcoming and kind lab mates and for the friends that I made during this amazing journey.

Special thanks are owed to my thesis committee members, Luka Brcic and Andelko Hrzenjak, for their valuable consultation with my thesis project during these last few years.

I want to extend my appreciation to my doctoral school - the DK-MCD - and the SFB Lipid Hydrolysis, not only for the financial support and for providing me with the opportunity to do this thesis, but also for the great community, the collaborations, and all the outstanding people I met along the way.

I want to express my genuine gratitude to all my friends who have been by my side throughout the past years and who have supported and believed in me. Finally, my family deserves my wholehearted appreciation for their unwavering support and unconditional love throughout my entire life and through my PhD journey. Mama, Papa, Franz, and Johannes, I am beyond thankful for all the support and all the love. Above all, I want to thank my partner, Benni; thank you for always cheering me up, making me laugh, keeping me grounded, and at the same time believing in me, especially when I don't – I owe you my deepest gratitude.

Table of Contents

Abbreviations

2AG	2-arachidonoylglycerol
ABP	activity based probe
ACC	acetyl-CoA carboxylase
ACS	acyl-CoA synthetase
ACSS2	acetyl-CoA synthetase 2
ACTA	acyl-CoA:cholesterol acyltransferase
ACTH	adrenocorticotropic hormone
ADP	adenosine diphosphate
AGPAT	acylglycerol-3-phosphate acyltransferase
ALDOA	aldolase A
ATP	adenosine triphosphate
CAA	chloroacetamide
CAF	cancer-associated fibroblast
cAMP	cyclic adenosine monophosphate
CE	cholesterol ester
CoA	coenzyme A
CPT	carnitine palmitoyltransferase
CSC	cancer stem cells
DCM	dichloromethane
DDA	data dependent acquisition
DG	diacylglycerol
DGAT	acyl-CoA:diacylglycerol acyltransferase
DIA	data independent acquisition
EC	endothelial cells
EGFR	epidermal growth factor receptor
EMT	epithelial to mesenchymal transition
ENO	enolase
ER	endoplasmic reticulum
ETC	electron transport chain
FABP	fatty acid binding protein
FACS	fluorescence activated cell sorting
FAD	flavin adenine dinucleotide
FAME	fatty acid methyl ester
FH	fumarate hydratase
G0S2	G0/G1 switch gene-2
GAPDH	glyceraldehyde-3-phosphate dehydrogenase
GLDH	glutamate dehydrogenase
GLS	glutaminase
GOT	glutamic-oxaloacetate transaminase
GPAT	glycerol-3-phosphate acyltransferase
GPI	glucose-6-phosphate isomerase
GTP	guanosine triphosphate
HDI	human developmental index
HDR	homology directed repair

HIF	hypoxia inducible factor
HILPDA	hypoxia inducible lipid droplet associated protein
HK	hexokinase
IC	immune cells
KO	knockout
KRAS	kirsten rat sarcoma
LASC	lung adenosquamous carcinoma
LCLC	large cell lung carcinoma
LD	lipid droplet
LDH	lactate dehydrogenase
LFQ	label-free quantitation
LLCC	lung large cell carcinoma
LOD	loss of attachment
LPL	lipoprotein lipase
LUAD	lung adenocarcinoma
LUSC	lung squamous cell carcinoma
lysoPA	lysophosphatidic acid
lysoPL	lysophospholipid
MEF	mouse embryonic fibroblast
MG	monoacylglycerol
MTBE	methyl-tert-butyl ether
MUFA	monounsaturated fatty acid
NAD(P)	nicotinamide adenine dinucleotide (phosphate)
NEM	N-ethylmaleimide
NET	neuroendocrine tumor
NSCLC	non-small cell lung cancer
NTA	normal tumor-adjacent
OE	overexpression
PA	phosphatidic acid
PAP	phosphatidate phosphatase
PASEF	parallel acquisition-serial fragmentation
PC*	pyruvate carboxylase (* Figure 4)
PC*	Phosphatidylcholine (* everywhere else)
PDC	pyruvate dehydrogenase compex
PDK	pyruvate dehydrogenase kinase
PE	Phosphatidylethanolamine
PFK	Phosphofructokinase
PFKFB	phosphofructokinase-2/fructose-2,6-bisphosphatase
PFKL	phosphofructokinase-liver type
PG	Phosphatidylglycerol
PGAM	phosphoglycerate mutase
PGE_2	prostaglandin E2
PGK	phosphoglycerate kinase
PHD	prolyl hydroxylase
PI	phosphatidylinositol
PK	pyruvate kinase

PKA	protein kinase A
PL	phospholipids
PNPLA	patatin-like phospholipase domain containing protein
PPP	pentose phosphate pathway
PS	phosphatidylserine
PUFA	polyunsaturated fatty acid
SCD	stearoyl-CoA desaturase
SCLC	small cell lung cancer
SDB-RPS	styrenedivinylbenzene-reversed phase sulfonate
SDH	succinate dehydrogenase
SDS	sodium dodecyl sulphate
sgRNA	short guide ribonucleic acid
SLC	solute carriers
SM	sphingomyelin
SPD	samples per day
TCA	tricarboxylic acid
TCEP	tris(2-carboxyetheyl) phosphine
TF	transcription factor
TFE	trifluoroethanol
TG	triacylglycerol
TKI	tyrosine kinase inhibitor
TME	tumor microenvironment
TPI	triosephosphateisomerase
WAT	white adipose tissue
WHO	World Health Organziation
α-KG	α-ketoglutarate

Zusammenfassung

Krebs gehört weltweit zu den häufigsten Todesursachen und ist zusammen mit Herz-Kreislauf-Erkrankungen für mehr als die Hälfte der weltweiten Todesfälle verantwortlich. Lungenkrebs ist eine der am häufigsten diagnostizierten Krebsarten und verursacht die meisten krebsbedingten Todesfälle. Eine wichtige therapeutische Strategie zur Krebsbekämpfung besteht darin, die Unterschiede im Stoffwechsel zwischen Tumor- und normalen Zellen gezielt zu nutzen. Krebszellen passen ihren Stoffwechsel an, um höheren bioenergetischen und biosynthetischen Anforderungen gerecht zu werden, was sich meist in unterschiedlich regulierten Stoffwechselwegen widerspiegelt. Bereits in der ersten Hälfte des 20. Jahrhunderts wurden höhere Glukoseaufnahme und Glykolyse Aktivität, sowie eine erhöhte Abhängigkeit von Glutamin als Krebseigenschaften beschrieben. Andere Änderungen im Stoffwechsel von Krebszellen wurden erst in den letzen Jahrzehnten entdeckt, wie beispielsweise eine erhöhte Aufnahme und Synthese von Fettsäuren im Lipidstoffwechsel. Die Rolle des Lipidabbaus ist in diesem Zusammenhang bisher jedoch weniger gut erforscht. Ziel dieser Arbeit ist es, Lipidspaltung im Lungenkrebs besser zu verstehen, indem Enzyme, die am Lipidabbau innerhalb der Zelle beteiligt sind, sowie deren Einfluss auf den Krebsstoffwechsel, untersucht werden.

Im ersten Teil dieser Arbeit untersuchten wir die Eigenschaften und das Proteom einer Lungenkrebszelllinie nach Verlust des Schlüssel-Enzyms (Adipose Triglyceride Lipase (ATGL)) des Abbaus von Triglyzeriden aus Lipidtröpfchen. Wir konnten erhöhte Zellvermehrung und eine Veränderung von Stoffwechselproteinen in Zellen beobachten, denen ATGL fehlt, wenn diese in *in-vivo*-ähnlichen Zellkulturmodellen kultiviert wurden. Eine erhöhte Glukoseaufnahme und Laktatausscheidung sowie ein höherer Gehalt an einfach ungesättigten Fettsäuren in Zellen ohne ATGL bestätigten diese Ergebnisse zusätzlich, was weiter auf einen glykolytischen Phänotyp, sowie auf Veränderungen im Lipidstoffwechsel hindeutet. Darüber hinaus untersuchten wir den Phänotyp und das Proteom weiterer Lungenkrebs-Zelllinien, die durch Ausschalten von ATGL oder einer anderen intrazellulären Lipase (Monoglycerid Lipase (MGL)) einen Lipidabbau-Mangel widerspiegelten. Der Verlust von ATGL in allen getesteten Zelllinien führte zu einer Anhäufung von Lipidtröpfchen, und der Mangel an Lipidabbau führte in einigen, aber nicht

in allen Zelllinien zu einer erhöhten Zellvermehrung in 2D- und 3D-Zellkultur Modellen, unabhängig davon, welche Lipase ausgeschaltet wird (ATGL oder MGL).

Im zweiten Teil dieser Arbeit untersuchten wir Lipidabbau in menschlichen Lungentumoren mit Hilfe mehrerer bioanalytischer Methoden. Wir beobachteten Veränderungen in der Genexpression einiger Lipasen und Lipase-Regulatoren. Darüber hinaus fanden wir eine Veränderung in der Abundanz und Verteilung von Lipiden - am auffälligsten war eine signifikante Anhäufung von Triglyceriden in Tumoren. Schließlich entdeckten wir auch, dass mehrere Lipasen in den Lungentumoren weniger häufig vorkamen und auch eine geringere Aktivität aufwiesen als im normalen Gewebe.

Zusammenfassend deuten unsere Daten auf eine deregulierte Lipidhydrolyse bei Lungenkrebs hin, und wir beobachten, dass der Verlust von Lipidhydrolasen zu metabolischen Veränderungen und einem stärker proliferativen Krebs-Phänotyp führen kann.

Abstract

Cancer is among the leading causes of death worldwide, and together with cardiovascular diseases, it accounts for more than half of the global fatalities. Lung cancer is one of the most often diagnosed types of cancer and accounts for the highest number of cancer-related deaths. An important anticancer therapeutic strategy is the targeting of metabolic differences between tumor and normal cells. Cancer cells generally adapt their metabolism to support increased bioenergetic and biosynthetic demands, which is reflected in differentially regulated metabolic pathways. Cancer phenotypes like increased glucose uptake, higher glycolytic flux, as well as increased glutamine dependence, were already documented in the early to mid-20th century. In previous decades, changes in lipid metabolism like fatty acid uptake and synthesis have been described as emerging cancer phenotypes. The role of lipid catabolism, however, is less well explored in this context. The aim of this thesis is to study lipid hydrolysis in lung cancer, through investigating enzymes involved in intracellular lipid catabolism, and their influence on cancer progression and metabolism.

In the first part of this thesis, we investigated the phenotype and proteome of a lung cancer cell line upon CRISPR-Cas9-mediated knockout of Adipose Triglyceride Lipase (ATGL), the rate-limiting enzyme of triglyceride catabolism from lipid droplets. We observed significantly increased proliferation and changes in metabolic proteins in cells lacking ATGL when grown in *in-vivo*-like cell culture models. Increased glucose uptake and lactate excretion, as well as higher levels of monounsaturated fatty acid species, in cells lacking ATGL corroborated the findings of the proteomics experiment that hint towards a more glycolytic phenotype and changes in lipid metabolism. Moreover, we investigated the phenotype and proteome of additional lung cancer cell lines that display lipolysis deficiency through knockout of ATGL or Monoglyceride Lipase (MGL), which is another enzyme involved in intracellular lipolysis. We found that the loss of ATGL caused lipid droplet accumulation in all tested cell lines, and in some but not all cell lines lipolysis deficiency caused significantly increased proliferation in 2D as well as 3D cell culture, independent of the lipase that is knocked out (ATGL or MGL).

In the second part of this thesis, we aspired to investigate lipid hydrolysis in human lung tumors by means of multiple bioanalytic methods. We observed changes in gene expression of some lipases or lipase co-regulators. Furthermore, we discovered changes in the abundance and pattern of lipids- most strikingly a significant accumulation of triglycerides in tumors. Finally, proteomics analysis also revealed changes in proteins involved in triglyceride catabolism, with several lipases being lower abundant, as well as lower in activity in the lung tumors.

Overall, our data point towards deregulated lipid hydrolysis in lung cancer, and we observe that loss of lipid hydrolases can result in metabolic changes and a concomitant more proliferative cancer phenotype.

1 General Introduction

1.1 Cancer

As reported by the International Agency for Research on Cancer (IARC) in the 2020 GLOBOCAN cancer statistics – backed up by the World Health Organization (WHO) mortality database – cancer has been responsible for almost 10 million fatalities worldwide in the year 2020 (10). This makes malignant neoplasms the most common cause of death worldwide after cardiovascular disease, which together account for more than half of all deaths worldwide[2]. With a rising world population and increasing life expectancy the global population is ageing (11), and along with it, the number of cancer-related deaths and incidences is rising (Figure 1). In 2020, there were approximately 19.3 million new cancer cases worldwide, and accordingly, the probability of developing cancer by the age of 75 is estimated to be at 20 % (10).

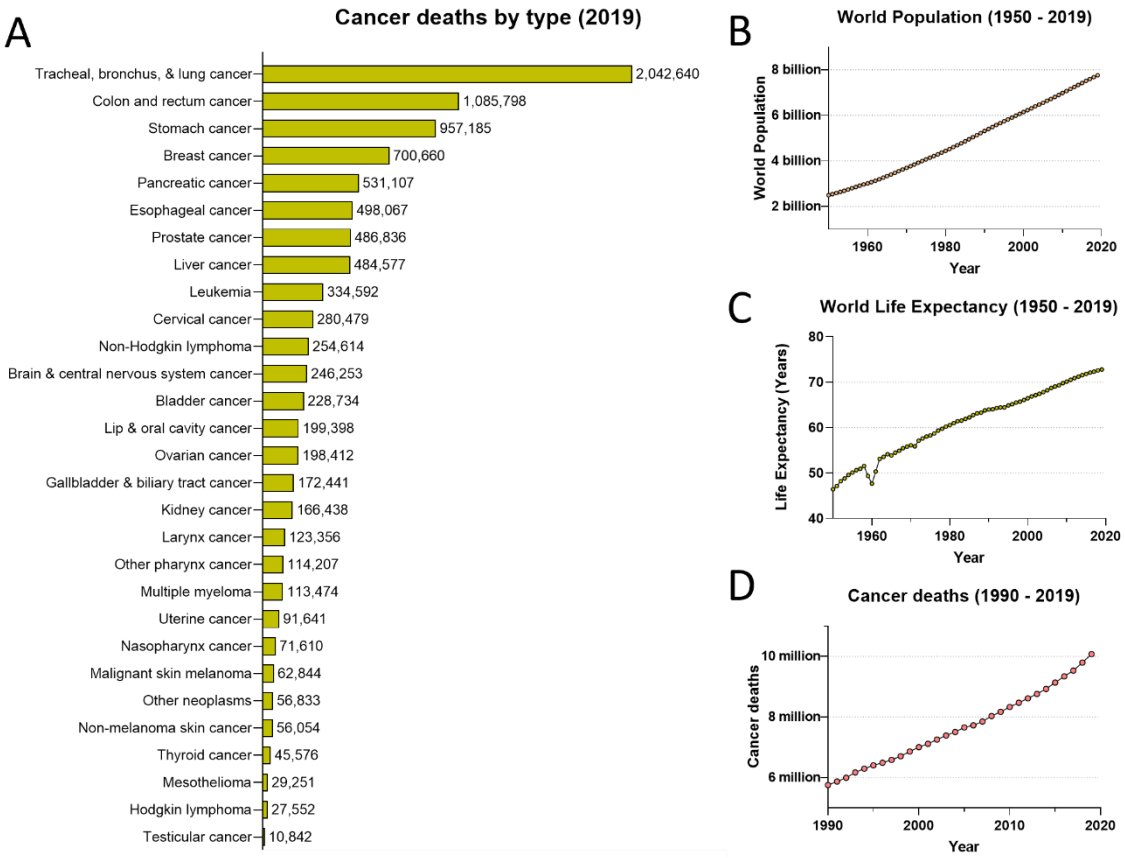

[2] https://ourworldindata.org/causes-of-death (accessed on: 11.10.2023)

Figure 1: world population, life expectancy, and cancer deaths over time and by type. A: lung cancer is the leading cause of cancer-related deaths in the world, data from 2019 (12); B: world population from 1950 to 2019 (11); C: world life expectancy from 1950 to 2019 (11); D: total number of cancer deaths over time from 1990 to 2019 (12). All charts were adapted from https://ourworldindata.org (accessed 11.10.2023) and are licensed under Creative Commons CC BY (free to use, share and adapt)

Cancer is a collection of diseases with a common characteristic: uncontrolled proliferation of abnormal cells. Cancer initiation and promotion (carcinogenesis) is a multi-stage process during which normal cells undergo transformation into tumor cells (13). This process is involving genetic factors as well as external factors, which can further be categorized into physical, chemical, and biological carcinogens[3]. The exposure to cancer-causing agents and thus cancer risk is dependent on environment and lifestyle. Some common risk factors due to lifestyle or environment include tobacco use, alcohol consumption, excess body weight, physical inactivity, air pollution, and infections (10). Overall, cancer risk increases significantly with age. This is due to the accumulation of the multitude of changes required for tumor initiation and a decline in cellular repair mechanisms (13).

The commonality of all cancers, uncontrolled proliferation, can occur in various types of cells and thus different tissues within the body, which gives rise to a plethora of different types of cancer. These different cancer types vary in their characteristics and response to treatment (14), and it is therefore indispensable to study the characteristics of each cancer in detail to eventually find more targeted therapy options.

Despite cancer being a diverse set of diseases with distinct characteristics, there are some common alterations in cell physiology – besides uncontrolled proliferation of abnormal cells – that occur in all or many of the different cancer types. These characteristics are commonly referred to as hallmarks of cancer, as they were defined and revisited by Hanahan and Weinberg (15, 16, 17).

[3] https://www.who.int/en/news-room/fact-sheets/detail/cancer (accessed on: 11.10.2023)

1.1.1 Lung Cancer

Among all types of cancer, lung cancer ranks as the second most frequently diagnosed cancer in both men and women. It stands out as the primary cause of cancer-related fatalities (10). In the US in data from 2023, lung cancer accounts for 12.2 % of all new cancer cases and more than 20 % of all cancer deaths, with a relative 5-year survival of 25.4 %[4]. An estimated 85 % of lung cancers are caused by tobacco smoke inhalation, whereby the lung cancer risk is determined by the duration and extent of tobacco use. Approximately 5 % of lung cancers are caused by occupational carcinogens, of which more than 90 % are caused by asbestos (18).

Histologically, lung cancers are divided into small cell lung carcinoma (SCLC) and non-small cell lung carcinoma (NSCLC) (Figure 2). SCLCs are usually neuroendocrine[5] carcinomas that are often centrally localized in the lung, and they comprise approximately 15 % of lung carcinoma cases. Due to a tumor doubling time of only 10-50 days, early diagnosis is rare and around 80 % of cases already show metastasis at diagnosis, which overall leads to a poor prognosis (18). NSCLCs account for 85 % of all lung cancers, and they are further divided into histological sub-subtypes. Squamous cell lung carcinomas (SCLC), predominantly located centrally, make up around 35 % of cases with a tumor doubling time of approximately 300 days. Lung adenocarcinomas (LUAD), constituting about 40 % of cases, often present in peripheral locations and have a faster tumor doubling time of 180 days. It's worth noting that adenocarcinomas are the most prevalent type of lung cancer among nonsmokers and are more frequently observed in women. Lung adenosquamous carcinomas (LASC), representing a mixed form of these two histological subtypes, are often observed. Large cell lung carcinoma (LCLC) constitutes about 10 % of lung cancers, with neuroendocrine carcinomas also found in the NSCLC category (18).

The most common sites of pulmonary metastases are lung, liver, brain, adrenal glands, and bone, and thyroid transcription factor 1 (TTF1) expression is usually used to differ between primary tumors (TTK1 positive) and pulmonary metastases (18). Mutation

[4] https://seer.cancer.gov/statfacts/html/lungb.html (29.10.2023) data from the US, representative for most high human developmental index (HDI) countries

[5] Neuroendocrine carcinomas, also called neuroendocrine tumors (NET) are tumors that can secrete hormones like adrenocorticotropic hormone (ACTH) or calcitonin (18)

analysis of the tumor cells is performed to offer targeted treatment, especially in later stage lung tumor with metastasis occurrence. Mutations of particular interest in lung cancer are genetic alterations in EGFR exon 18-21, ALK and ROS1 translocations, BRAF V600E mutations, NTRK fusions, RET translocations, HER2 gene amplifications/mutations, KRAS G12C mutations, and cMET alterations (18). According to the COSMIC Catalogue of Somatic Mutations in Cancer, the top three mutations in lung cancer are epidermal growth factor receptor (EGFR)[6] mutations, TP53[7] mutations, and KRAS[8] mutations (24).

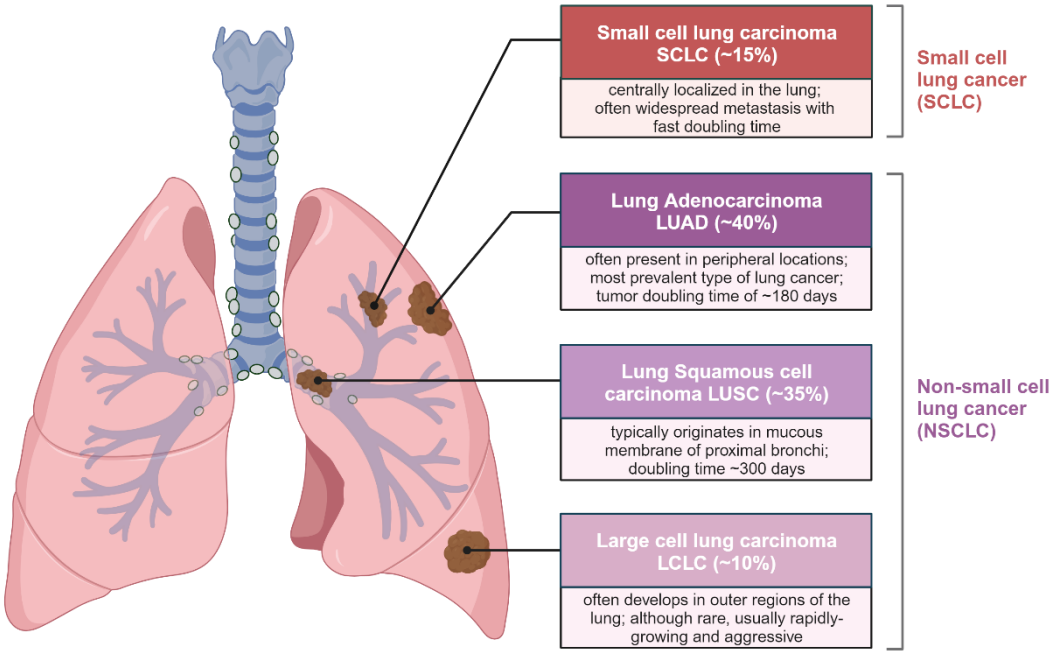

Figure 2: Histological Subtypes of Lung Cancer and their characteristics. (Created with BioRender.com)

[6] EGFR is a receptor tyrosine kinase involved in cell signaling and can be associated with the development and progression of certain cancers when mutated (19).

[7] p53 (gene name: *TP53*) is a tumor suppressor protein that regulates the cell cycle, promotes DNA repair, and initiates apoptosis in damaged or potentially cancerous cells. *TP53* loss or loss-of-function mutations are the most frequently occurring genetic alterations occurring in cancer (20)

[8] Kras, short for **K**irsten **ra**t **s**arcoma virus is part of the RAS/MAPK pathway and thereby plays a key role in cell signaling pathways involved in cell proliferation (21). It is a major proto-oncogene and one of the most often mutated genes in cancer. In lung adenocarcinoma, with 30 % mutation frequency, Kras is the most frequently mutated oncogene observed (22, 23).

1.1.2 Hallmarks of Cancer

The hallmarks of cancer are an attempt to simplify the extensive complexity of cancer phenotypes and genotypes into a set of shared molecular, biochemical and cellular traits, or: acquired capabilities (15). The original publication (2000) described six biological capabilities that are acquired by cells during carcinogenesis: (a) self-sufficiency in growth signaling; (b) insensitivity to growth suppressor signals; (c) resistance to apoptosis; (d) induction of angiogenesis; (e) activating tissue invasion and metastasis; (f) and limitless replicative potential (15). In their follow-up publication a decade later, they present two emerging hallmarks: (g) evasion of immune destruction, and (h) reprogramming of energy metabolism. Furthermore, they define (i) genome instability as an underlying quality of carcinogenesis, which generates the genetic diversity to accelerate the acquisition of many of the other hallmarks. Likewise, they describe (j) tumor-promoting inflammation as an underlying and enabling characteristic (16). These hallmarks are visualized in Figure 3.

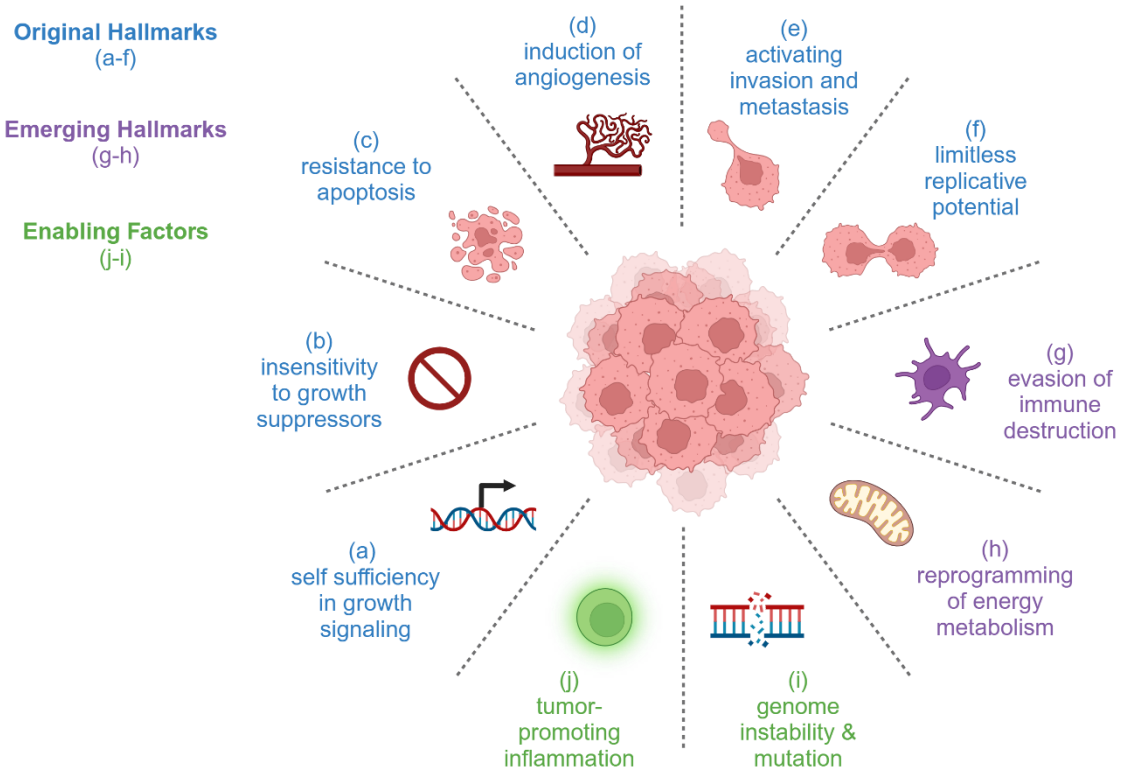

Figure 3: the Hallmarks of Cancer were first described by Hanahan and Weinberg in 2000 (15) and later revisited and expanded in 2011 (16). (a – f) Original Hallmarks; (g – h) Emerging Hallmarks; (j – i) enabling factors. (Created with BioRender.com)

These hallmarks are focused on normal cells undergoing transformation into cancer cells. Tumors, however, are not simply isolated masses of cancer cells but complex tissues involving various cell types. Several non-cancerous cells are part of the tumor-associated stroma, including cancer-associated fibroblasts (CAF), endothelial cells, pericytes, cancer stem cells (CSC), and inflammation and immune cells (16, 17). Stromal cells are not only bystanders of tumorigenesis but may play an active role and contribute to the development of key cancer traits. This more recent consideration emphasizes that understanding tumor biology requires considering the contributions of the tumor microenvironment (TME) in addition to the traits of cancer cells (16).

There are two central components in the intricate web of genetic factors that underlie uncontrolled cell proliferation in cancer: oncogenes and tumor suppressor genes (14). While oncogenes are genes with the potential to promote excessive proliferation of cells through dominant gain-of-function mutations, tumor suppressor genes are involved in regulation of cell cycle, DNA repair and apoptosis, and carcinogenesis often involves loss-of-function mutations of tumor suppressor genes (13). However, disrupted cell control mechanisms are not enough for indefinite cancer cell proliferation. In order to persist and sustain growth, cancer cells must adjust their metabolism to thrive in the TME, where nutrients and oxygen might become limiting (16).

1.1.2.1 Reprogramming energy metabolism

During proliferation cells must duplicate all macromolecules (amino acids, lipids, nucleotides) at each pass through the cell cycle, which necessitates the availability of sufficient nutrients, energy, and biosynthetic activity. Consequently, cancer cells, which are usually in a state of proliferation, have distinct metabolic needs compared to those of most well-differentiated normal cells (25). Through adjusting the flux through various metabolic pathways, cancer cells sustain challenges such as continuous anabolic growth and survival in nutrient-poor environments (26).

1.1.2.1.1 Changes in glucose metabolism: aerobic glycolysis and cataplerosis

In most cells and tissues, carbohydrate-derived glucose is the main source of energy (14). Cancer generally exhibits accelerated glucose metabolism, a feature so pronounced that it is even used in clinics for cancer staging, diagnosis, and treatment assessment, using ^{18}F-deoxyglucose (FDG) positron emission tomography (PET)[9] (27).

Changes in glucose metabolism were first reported in 1924 by Otto Warburg, who described that carcinoma cells display increased glucose consumption and lactic acid production, even in the presence of oxygen (28) – a phenomenon now commonly known as the "Warburg effect" or aerobic glycolysis. The preferential fermentation of glucose into lactate as compared to its full oxidation to carbon dioxide in mitochondria yields significantly fewer molecules of adenosine triphosphate (ATP) per molecule of glucose (14). Warburg initially proposed that this metabolic phenotype arises from damaged mitochondria and thus an impaired cellular respiration system (28), but later it was shown that cancer cells have functional mitochondria and retain their ability to carry out respiration (29). It is now widely accepted that – despite preferentially fermenting glucose to lactate – cancer cells rely on functional mitochondria, and part of the glucose-derived pyruvate is usually still metabolized through the tricarboxylic acid (TCA) cycle and oxidative phosphorylation.

The substantial reduction in ATP production efficiency through fermentation when compared to mitochondrial oxidative phosphorylation – ca. 18-fold less ATP is produced – is compensated by increased glucose uptake and metabolism (30, 31). The uptake of glucose into the cell is facilitated by solute carriers (SLC[10]), and many human cancers show upregulated expression of glucose transporters (GLUTs) (31). Especially GLUT1 and GLUT3 are facilitative glucose transporters associated with cancer. Several oncogenes are associated with upregulation of glucose uptake and glycolysis (32). For example, the expression of GLUT1 was shown to be upregulated upon mutation of the oncogene *Kras*

[9] FDG - ^{18}F-deoxyglucose - is the most widely used PET imaging radiotracer in the clinics. It is based on cancer cells taking up more glucose (and thus also FDG) than normal cells. After phosphorylation within the cell, FDG-6-phosphate cannot be further metabolized and accumulates, which is imaged by PET (27).

[10] Glucose is transported across the cell membrane by two distinct families of solute carriers: SGLTs (gene family name: *SLC5A*), which are secondary active Na^+/glucose co-transporters, and GLUTs (gene family name: *SLC2A*), which are facilitative glucose transporters. Amongst the facilitative glucose transporters, there are a total of 14 proteins (GLUT 1-14; *SLC5A1-SLC5A14*) (31).

(23, 33). On the contrary, the tumor suppressor p53 was found to inhibit *SLC2A1* and *SLC2A3* expression (34, 35), while a cancer-associated p53 mutation was found to promote GLUT1 translocation to the plasma membrane, thereby increasing glucose uptake and the Warburg effect (36). In lung adenocarcinoma (LUAD) cells, oncogenic epidermal growth factor receptor (EGFR) signaling, driven by gain-of-function mutations in EGFR, was linked to increased glucose uptake and glycolysis. EGFR tyrosine kinase inhibitors (TKI) were observed to reduce glucose consumption and lactate production, specifically targeting GLUT3 expression while leaving GLUT1 unaffected in drug-sensitive lung tumor cells (19).

After its uptake, glucose is metabolized within the cell. Glycolysis marks the first phase of glucose metabolism and consists of nine reactions. Among these reactions, two are energy-consuming phosphorylation reactions, catalyzed by two tightly regulated enzymes: hexokinase (HK) and phosphofructokinase (PFK). The third rate-limiting step in glycolysis is carried out by pyruvate kinase (PK), which also involves the transfer of a phosphate group. All three glycolysis-regulating enzymes have been found to play a role in cancer (37, 38).

HK is the first step of glycolysis and produces glucose-6-phosphate by phosphorylation of glucose. There are four HK isoforms in mammalian tissue: HK1-3 are known as hexokinases and have high affinity for glucose, while HK4, also termed glucokinase, has a lower affinity for glucose (39). In malignant tumors, HK2 is the predominantly overexpressed isoform and is strategically located on the outer mitochondrial membrane (40). This location grants HK2 preferential access to mitochondrial-generated ATP, while it also protects it from product inhibition by glucose-6-phosphate, which all together drives high rates of glycolysis and biosynthetic pathways and facilitates uncontrolled tumor proliferation (39, 40, 41).

The conversion of fructose-6-phosphate to fructose-1,6-bisphosphate by PFK exhibits a highly favorable thermodynamic profile, characterized by a substantial negative ΔG[11], and is therefore considered the most important rate-limiting step in glycolysis (38).

[11] The change in Gibbs free energy (ΔG) of a biochemical reaction summarizes the effects of changes in enthalpy and entropy. The ΔG is a measure of how energetically favorable a reaction is. A negative ΔG value for a reaction indicates a strong thermodynamic driving force for the reaction in a forward direction (14)

PFK is inhibited by high levels of ATP, but presence of the PFK-activating metabolite fructose-2,6-bisphosphate overrides this inhibition (42). The bifunctional enzymes phosphofructo-2-kinase and fructose-2,6-bisphosphatases (PFKFBs) are responsible for the synthesis as well as the degradation of fructose-2,6-bisphosphate (43). PFKFB3, which shows the highest 6-phosphofructo-2-kinase activity, was found to be upregulated in numerous human cancers, thereby increasing glycolytic flux through activation of PFK (44, 45).

The final step of glycolysis is catalyzed by PK, which transfers a phosphate group from phosphoenolpyruvate to adenosine diphosphate (ADP), thereby generating ATP and pyruvate (46). In humans, there are four distinct PK enzymes with unique distribution patterns: PKR is specific to red blood cells, PKL is predominantly present in the liver and kidney, PKM1 is expressed in mature somatic cells such as muscle and brain, and PKM2 is primarily found in fetal tissues and rapidly proliferating cells (37). Growing evidence indicates PKM2 to be the predominant isoform of PK in tumors (47). The enzymatic activity of PKM2 is modulated by a range of metabolic and signaling cues in cancer, and its regulation plays a crucial role in determining the fate of glucose-derived carbons, which either provide building blocks for biosynthesis or are metabolized for regeneration of energy (48). Increased PKM2 expression leads to suppression of PKM1, an enzyme that is constitutively active and throttles the production of carbon for anabolic reactions while promoting mitochondrial ATP generation. Favoring PKM2 expression therefore causes a bottleneck at the final stage of glycolysis, which ultimately leads to higher levels of glycolytic intermediates upstream that supporting biosynthetic pathways (30, 49).

Some glycolytic intermediates play an important role as precursors for biosynthesis pathways in cancer cells. Glucose-6-phosphate can enter the pentose phosphate pathway (PPP) and thereby contribute to nucleotide and NADPH synthesis (38). Besides its role in glycolysis, 3-phosphoglycerate is also a precursor for serine and glycine synthesis, which are shunted into the folate cycle to contribute to nucleotide and lipid synthesis (38, 50). Dihydroxyacetone phosphate can be converted to glycerol-3-phosphate, which is the starting point for glycerol phospholipid biosynthesis in the endoplasmic reticulum (ER) membrane (14).

The final product of glycolysis is pyruvate. More precisely, one molecule of glucose (6C) gives rise to two molecules of pyruvate (3C), two molecules of ATP and two molecules of NADH in the process of glycolysis (14). The fate of pyruvate is then determined by the activities of two enzymes: pyruvate dehydrogenase kinase (PDK) and lactate dehydrogenase (LDH). In normal differentiated cells under oxygen availability, pyruvate enters the TCA cycle through the pyruvate dehydrogenase complex (PDC) and is eventually oxidized to CO_2, resulting in nicotinamide dinucleotide (NADH) and flavin adenine dinucleotide ($FADH_2$) (14). In the electron transport chain (ETC), the reoxidation of the produced NADH (from glycolysis and in the TCA cycle) and $FADH_2$ requires O_2 as a final electron acceptor (38). In anaerobic conditions, this regeneration of NAD^+ through the electron transport chain does not work, but fermentation of pyruvate to lactate through LDH can regenerate NAD^+ (38). Several studies have shown that LDH – mostly LDH isoform A (LDHA) – exhibits elevated expression in cancer, and this heightened expression is linked to increased malignancy (51, 52, 53, 54). In addition to increase LDH activity, pyruvate entry into the TCA cycle is also downregulated through inhibition of pyruvate dehydrogenase (PDH). Regulation of PDH primarily occurs through phosphorylation and thus inhibition by PDK-1, which is frequently upregulated in cancer, thereby contributing to aerobic glycolysis (38, 55).

When pyruvate is not reduced to lactate, it can be decarboxylated and transferred onto a CoA molecule via the PDC, to produce an acetyl CoA molecule. In the TCA cycle, an acetyl unit (2C) from acetyl-Coenzyme A (acetyl-CoA) is combined with oxaloacetate (4C) to produce citrate (6C), which cycles through several reactions while producing CO_2, NADH, $FADH_2$, and GTP, and regenerating oxaloacetate in the end for reuse (14). It is noteworthy, that the two carbons exiting the TCA cycle as CO_2 are not the ones that are added from the acetyl unit and thus that are derived from glucose (38).

The TCA cycle and its intermediates play a crucial role in cancer cells by supplying precursors for biosynthesis pathways of important macromolecules: lipids, nucleotides, and amino acids. In cancer and proliferating cells, a significant part of the carbon entering the TCA cycle is shuttled into biosynthetic pathways (25, 30). This continuous loss of TCA cycle intermediate metabolites is also known as cataplerosis (56). One significant cataplerotic pathway in cancer cells is the biosynthesis of lipids from citrate (57). In cancer cells, most

of the carbon for fatty acid (FA) synthesis is derived from glucose (30, 57). The dependency of cancer on citrate for FA production is apparent from the dependency on the enzyme ATP citrate lyase (ACL), which is needed for the conversion of citrate to acetyl-CoA in the cytosol (57).

Oxaloacetate and α-ketoglutarate (α-KG) can provide building blocks for the biosynthesis of nonessential amino acids, like aspartate or glutamate, which are required for protein and nucleotide synthesis (25).

Some TCA cycle enzymes can act as tumor suppressor or oncogene and thereby promote malignancy. Succinate dehydrogenase (SDH) and fumarate hydratase (FH) catalyze the conversion of succinate to fumarate and fumarate to malate, respectively, and are mutated in some cancers (58). One of the most prominent mutations in a metabolic enzyme is a mutation in isocitrate dehydrogenase IDH1 in human brain cancer (58, 59). IDH1 and IDH2 usually catalyze the oxidative decarboxylation of isocitrate to α-KG under use of $NADP^+$ as a cofactor, in the cytosol or mitochondria, respectively. Upon mutation, these enzymes lose their ability to convert isocitrate to α-KG and instead produce the oncometabolite 2-hydroxyglutarate (2HG) from α-KG, which causes an increased rate of histone methylation through reducing α-KG-dependent dioxygenase activity (58, 59, 60).

Taken together, cancer cells significantly rewire their glucose metabolism to meet required bioenergetic and biosynthetic needs. Although energetically less favorable, most cancers – and for that matter also other highly proliferating cells – preferentially ferment pyruvate into lactate, while still performing oxidative phosphorylation at a lower rate. In recent years, it has been proposed that the reprogramming of energy metabolism to a more glycolytic phenotype supports the integration of nutrients into the essential building blocks required for biosynthetic pathways (30). An overview of changes in glucose metabolism in cancer cells is shown in Figure 4.

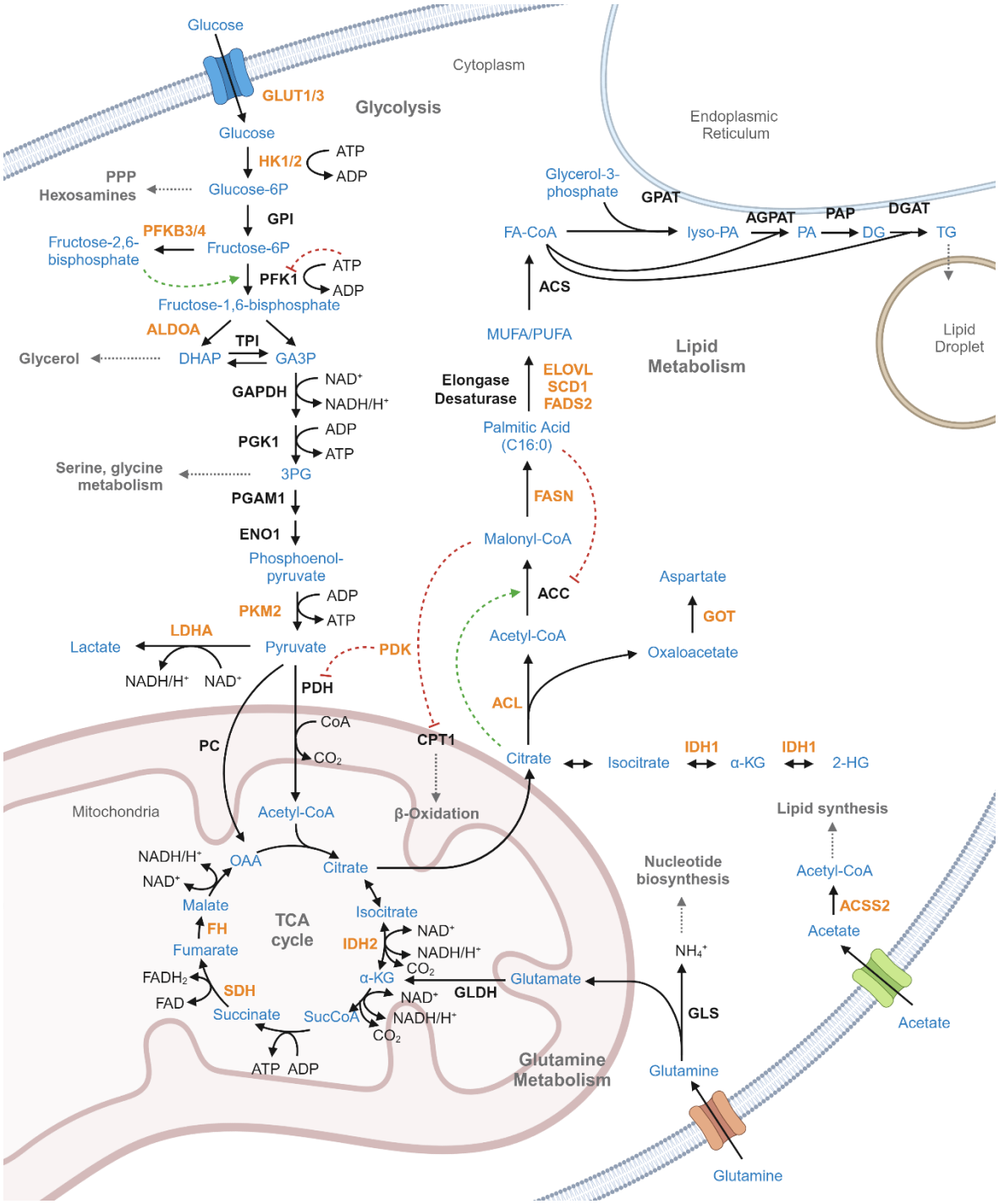

Figure 4: overview of changes in glucose metabolism (top left), glutamine metabolism (bottom) and lipid metabolism (top right) in cancer. Metabolites are blue, cofactors are black, enzymes are bold black or orange (if deregulated in cancer), inhibition or activation is visualized by red or green dashed arrows, respectively, and further pathways are shown in grey. Please refer to the text (and list of abbreviations) for a description of the depicted pathways. (Created with BioRender.com)

1.1.2.1.2 Anaplerosis: glutaminolysis and pyruvate carboxylation

As mentioned in the previous chapter, glycolytic as well as TCA cycle intermediates serve as important precursors for biosynthetic pathways to generate lipids, nucleotides, and amino acids (25, 30, 38, 50, 57). To support these biosynthetic reactions, while at the same time maintaining TCA cycle, it is necessary to replenish TCA cycle intermediates through anaplerotic pathways (56).

The two most important anaplerotic pathways in cancer cells are pyruvate carboxylation, which directly generates oxaloacetate from pyruvate in mitochondria (25), and glutaminolysis, the catabolism glutamine into α-KG (61). Glutamine, the most abundant amino acid in circulation, is one of the most important carbon sources for cells together with glucose, and likewise many cancers show increased uptake rates (25). After glutamine uptake, the enzyme glutaminase (GLS) catalyzes the conversion of glutamine into glutamate, which is further oxidized to α-KG by glutamate dehydrogenase (GLDH) under the formation of NADH or NADPH (37, 62). α-KG can then feed into the TCA cycle to replenish downstream TCA cycle intermediates like succinate, fumarate, and malate (63). Alternatively, IDH enzymes can convert α-KG into isocitrate by reductive carboxylation, and isomerization gives rise to citrate, which can support lipid biosynthesis through cytoplasmic ACL reaction (60).

While anaplerotic pathways such as glutaminolysis also occur in normal cells to support TCA cycle function (56, 64), the increased dependency on glutamine, which is referred to as glutamine addiction, is a characteristic primarily found in some cancers (37, 65). Increased glutamine uptake and glutaminolysis is supported by some oncogenic mutations like *Kras* or *Myc*[12], and reductive carboxylation is supported by hypoxic conditions and signaling (37, 60, 68, 69).

Glutamine is also an important nitrogen source for proliferating cells and contributes to the synthesis of purines and pyrimidines (70, 71). However, it was shown

[12] Myc is an oncogenic driver that acts as a universal enhancer of transcription by engaging with a multitude of factors and complexes that oversee nearly every cellular operation (66). Myc directly causes upregulation of enzymes involved in glutamine metabolism, like glutaminase, and thereby supports the glutamine anaplerosis pathway in Myc-driven cancer cells (67, 68)

that malignant cells with elevated rate of glutamine metabolism primarily use glutamine-derived carbons for regeneration of TCA cycle intermediates to support the use of TCA cycle intermediates derived from glucose for biosynthetic processes, rather than being dependent on glutamines nitrogen for nucleotide synthesis (72). Changes in glutamine metabolism in cancer cells are visualized in Figure 4.

1.1.2.1.3 Altered lipid metabolism: anabolic requirements and signaling

Fatty acids (FA) are particularly important for supporting cellular proliferation. They act as fundamental components for various cellular processes, such as building lipid membranes, storing and producing energy, and participating in cellular signaling (37). When needed, cells can acquire (exogenous) FAs through FA uptake or produce (endogenous) FAs through *de-novo* biosynthesis. Unlike most normal differentiated cells, cancer cells primarily generate endogenous FAs, and frequently show a shift towards FA synthesis (73, 74, 75).

De-novo fatty acid synthesis requires carbons derived from glucose or anaplerotic pathways (usually through glutamine) that are shunted into the cytosol in the form of citrate. As mentioned above, citrate in the cytosol can be converted into oxaloacetate and acetyl-CoA by ACL, and inhibition of ACL can curb cancer growth (57). Glucose and lipid metabolism are linked through this crucial reaction generating acetyl-Co A from glucose- or glutamine-derived citrate. Acetyl-CoA serves as the fundamental building block for the synthesis of fatty acids and isoprenoids, while it also has an important function in signaling due to its role in the acetylation of lysine (76). For FA biosynthesis, malonyl-CoA is produced from acetyl-CoA through acetyl-CoA carboxylase (ACC), which is the most tightly regulated enzyme in FA synthesis (75). While citrate and glutamate activate ACC allosterically, palmitoyl-CoA and other FA-CoAs as well as phosphorylation contribute to the inactivation of ACC. Malonyl-CoA, on the other hand, inhibits carnitine palmitoyltransferase 1 (CPT1), which is the rate-limiting enzyme of FA β-oxidation (75). Finally, one acetyl-CoA and seven malonyl-CoA are combined through a series of successive condensation reactions catalyzed by fatty acid synthase (FASN), resulting in the formation of the saturated 16-carbon fatty acid known as palmitate (C16:0) (77). Increased levels and activity of FASN has been documented in numerous types of cancer and correlates with poor prognosis (78, 79).

Following the formation of saturated fatty acids like palmitic acid (C16:0), elongases, desaturases, and acyl-CoA synthetase (ACS) assist in the modification and activation of FAs. Stearoyl-CoA desaturases (SCD) and fatty acid desaturases (FADS) generate monounsaturated and polyunsaturated fatty acids (MUFA and PUFA) that are elongated by fatty acid elongase (*ELOVL*) enzymes, and ACS transfers FAs onto CoA, resulting in formation of FA-CoAs, which are available for cellular use (75, 77). An appropriate ratio of saturated FAs (SFA) to unsaturated FAs (UFA) in cells is important, and it has been recognized that a high content of SFAs can induce cell death (80). Therefore, the expression and activity of desaturases like SCD1 is crucial, and upregulation has been observed in some cancers (75, 81).

Although FA synthesis is the primary route to increase the pool of FAs in cancer cells, the uptake of lipids and FAs though fatty acid binding proteins (FABP) and is an alternative way for cancer cells to obtain enough complex fatty acids. This is especially important under conditions of hypoxia or Ras-transformation when oxygen-dependent enzymes like SCD are inhibited and the conversion of SFA to UFA is low (82).

FAs that are taken up or synthesized can be used to build more complex lipids, which can be incorporated into biomembranes[13] or play a role as signaling lipids[14] (14, 83). Oleic acid (C18:1), which can be synthesized *de-novo*, can directly contribute to the synthesis of phosphatidic acid (PA) and TGs. Conversion of glycerol-3-phosphate and acyl-CoA by the ER-residing glycerol-3-phosphate acyltransferase 1 (GPAT) is the first committed step in TG synthesis via the glycerol phosphate pathway. The resulting lysophosphatidic acid (lysoPA) is further esterified with another acyl-CoA, yielding phosphatidic acid (PA), by acylglycerol-3-phosphate acyltransferase (AGPAT). Besides its structural and signaling functions, PA can act as a substrate for DG and thus TGs through acyl-CoA:diacylglycerol acyltransferase (DGAT) in the ER. It also plays a role in generating more complex glycerolipids like

[13] A large part of the lipids in biomembranes consists of four distinct phospholipids (PL): phosphatidylcholine (PC), phosphatidylethanolamine (PE), phosphatidylserine (PS) and sphingomyelin (SM). Other lipids, like phosphatidylinositol (PI), cholesterol, and glycolipids are also part of most biomembranes (14).

[14] Lipid signaling molecules, such as eicosanoids, phosphoinositides, sphingolipids (e.g., sphingosine-1-phosphate) FAs (e.g., arachidonic acid), lysophospholipids (e.g., lysophosphatidic acid) or platelet-activating factor or anandamide, play a role in regulating cellular functions like proliferation, apoptosis, metabolism, and motility (83).

phosphatidylinositols (PI), phosphatidylserines (PS), phosphatidylcholines (PC) and phosphatidylglycerols (PG) (77, 84).

Another fate of FAs is their degradation through FA β-oxidation. In this process, two carbon units (2C) are subsequently cleaved from a FA until acetyl-CoA remains. In each cycle, NADH and $FADH_2$ are produced and thereby contribute to ATP production in the electron transport chain (14). Oxidation of FAs provides twice as much ATP compared to carbohydrates, making it a more efficient energy production pathway, and lipids, usually in the form of triglycerides (TG), are the main storage nutrient in conditions of nutrient abundance (85). The rate-limiting enzyme of FA catabolism, CPT1, converts FAs into acyl carnitines for import into mitochondria, and its role in cancer is multifaceted (75). The three isoforms of CPT1 might play distinct roles in different types of cancer. Compared to CPT1B, which is primarily expressed in brown adipose tissue, muscle, and heart, CPT1A is ubiquitously expressed and overexpressed in some cancers, including leukemias, breast, and prostate cancer (86, 87, 88). CPT1C, on the other hand, is expressed primarily in neurons and is located to the ER. CPT1C has been found to support tumor survival in harsh conditions and is a prognostic factor in various human cancers. Due to its localization in the ER and inefficient activity, it has recently been proposed to play less of a role for the oxidation of FAs and might act as a nutrient sensor instead (89). At the same time, all isoforms of CPT1 are inhibited by malonyl-CoA, a metabolite of the FA biosynthesis pathway that is usually high in cancer (75). This proposes that cancers with high FA biosynthesis activity preferentially use FAs as building blocks, suggesting that ATP is limiting for proliferation and growth (85). Cancer cells with exceptionally high demand for ATP, on the other hand, might upregulate the FA β-oxidation pathway in conditions where FAs are not limiting. This is exemplified by cells that undergo loss of attachment (LOS) to the extracellular matrix (ECM), which show decreased glucose uptake and rely on ATP from other sources. These cells survive through upregulation of FA β-oxidation (85, 90).

Taken together, the upregulation of β-oxidation of FAs in cancer cells provides energy for sustained cancer cell growth and proliferation, while *de-novo* FA synthesis provides lipid building blocks supporting cell growth and proliferation. Which pathways are upregulated in cancer cells depends on the limiting factors for proliferation, which is

influenced by their surroundings, which governs the availability of nutrients and oxygen. Figure 4 depicts some of the changes in lipid metabolism that are frequently observed in cancer cells.

1.1.2.1.4 Hypoxia in the context of metabolic reprogramming

The rapid proliferation of cancer cells often depletes the available nutrients and oxygen from the surrounding normal vasculature, leading to a state of hypoxia within the tumor. Hypoxia, which is characterized by reduced oxygen levels, is regulated by hypoxia-inducible factors (HIF) and is associated with pathological conditions (67).

HIF-1 and HIF-2 are heterodimeric transcription factors (TF). They comprise an oxygen sensitive HIFα subunit, as well as a constitutively active HIFβ subunit. The protein level of HIFα is regulated through prolyl hydroxylases (PHD), which – under oxygen availability – hydroxylate HIFα and thereby mark it for degradation. In situations of reduced oxygen, PHDs become inactive, HIFα is stabilized, accumulates, and forms dimers with HIFβ (91). The HIF heterodimer can bind to hypoxia responsive elements (HRE) of target genes. HIFs therefore regulate the metabolic changes associated with hypoxia through mediation of gene expression of a plethora of metabolic genes (67).

Glucose metabolism is affected by hypoxia through HIF1 mediated gene regulation. HIF1 induces gene expression of glucose transporters (*GLUT1*, *GLUT3*) (31) and several glycolytic enzymes (*HK1/2*, 6-phosphofructokinase-liver type (*PFKL), PFKFB3*, aldolase (*ALDA)*, phosphoglycerate kinase (*PGK1)*, enolase (*ENO1), PKM*) (92, 93, 94). It also induces lactate metabolism through upregulation of *LDHA* (95) and *PDK1* (96). Hypoxia thereby stimulates mammalian cells to increase glucose consumption, glycolytic flux, and lactate production (93).

Cancer cells rely on the uptake or *de-novo* synthesis of lipids to support the required biomass production. In hypoxic conditions, the production of acetyl-CoA from glucose is reduced, which results in an increased reliance on reductive glutamine flux for lipogenic acetyl-CoA production (67). In addition to reductive glutamine flux, hypoxic cancer cells were shown to utilize acetate for acetyl-CoA production (97), which is further supported by

stimulated acetyl-CoA synthetase 2 (ACSS2) expression in hypoxic or lipid depleted conditions (98). Hypoxic cells also support sufficient lipid availability by scavenging unsaturated FAs from lysophospholipids (lysoPL) through FABP4. FABP4 is a target of HIF1, and facilitates extracellular scavenging of long-chain unsaturated lysoPLs like LPCs, LPEs, and LPGs (82). FABP3 and FABP7 were also shown to be induced by HIF1, and were crucial for lipid uptake supporting hypoxia-induced lipid droplet formation (99). Besides lipid uptake, *de-novo* synthesis of FAs was shown to be increased in hypoxia through HIF1 activation of protein kinase B (PKB) and subsequent induction of the sterol regulatory element binding protein (SREBP) 1, which induces *FASN* expression (100).

Taken together, hypoxia and HIFs shape cancer cell metabolism substantially, by regulating the expression of several genes involved in glucose and lipid metabolism (67).

1.2 Lipid Hydrolysis

Hydrolysis is the chemical process in which the presence of water leads to the breaking of a chemical bond. (101) Lipid hydrolysis is catalyzed by lipases, which are enzymes mainly belonging to the enzyme class EC 3.1.1 (carboxylic ester hydrolases) (102, 103, 104, 105). Within carboxylic ester hydrolases, lipases are distributed across several subclasses, including carboxylesterases, phospholipases A1/A2, lysoPLs, sterol esterases, acylglycerol lipases, and triacylglycerol lipases (105). Lipases generally catalyze the cleavage of carboxylesters into their respective fatty acid and alcohol component through a mechanism facilitated by a catalytic serine found within a Ser-His-Glu triad (106, 107). The reactions follow a four-step process: (i) nucleophilic attack of serine on the substrate, forming the first tetrahedral intermediate, (ii) the formation of an acyl-enzyme complex and the release of the alcohol product, (iii) nucleophilic attack by a water or alcohol molecule to create the second tetrahedral intermediate, and (iv) the release of the second product of the reaction (108). The hydrolysis of TGs is termed lipolysis (102). In this process, the ester bond between FAs and the glycerol backbone of TGs is cleaved, the FA is replaced by water, and thereby FAs and glycerol are released (103).

In humans, there are three distinct lipolytic processes, gastrointestinal lipolysis, vascular lipolysis, and intracellular lipolysis (104). While gastrointestinal and vascular lipolysis are important for breaking down dietary lipids or lipoproteins, respectively, intracellular lipolysis occurs in virtually all cells and tissues throughout the body and it involves the cleavage of TGs stored in lipid droplets (LD) (104). There are specific lipases involved in all three processes. The primary lipolytic enzymes found in the gastrointestinal tract comprise lingual lipase, gastric lipase, pancreatic lipase, as well as pancreatic lipase-related proteins 1, 2, and 3. Lipoproteins in the vasculature, on the other hand, are mainly degraded by hepatic TG lipase and lipoprotein lipase. Most extracellular lipases found in the digestive tract and the vascular system are members of the pancreatic lipase gene family and are secreted, while intracellular lipases are structurally unrelated and act inside the cell (102, 104).

1.2.1 Intracellular lipolysis

Intracellular lipolysis is divided into neutral and acid lipolysis, with reactions catalyzed at either neutral (pH 7) or acid (pH 4-5) pH (Figure 5) (102). In most cases, the resulting FAs are used internally for energy production or various biosynthetic pathways. However, white adipose tissue (WAT) stands as an exception by releasing FAs and glycerol to support non-adipose tissues during times of nutrient scarcity (103). Although most abundant in WAT, lipid droplets and intracellular lipolysis occurs in all types of tissues and cells (109).

Intracellular acid lipolysis is essentially the breakdown of cholesteryl esters (CEs), TGs, DGs, and retinyl esters that are taken up from autophagosomes or lipoproteins into the lysosome, and only one enzyme is responsible for the breakdown of all of these lipids at acidic pH in the lysosomes: lysosomal acid lipase (LAL, *LIPA*) (110). In neutral lipolysis, on the other hand, the breakdown of intracellular TGs alone is orchestrated by several lipolytic enzymes with distinct substrate profiles.

The first and rate-limiting step of neutral lipolysis is carried out by Adipose Triglyceride Lipase (ATLG, *PNPLA2*). ATGL was identified in 2004 and belongs to the family

of patatin-domain-containing proteins (PNPLA) (111, 112). The primary substrates are long-chain FA-containing TGs, which ATGL cleaves preferably at the *sn*-2 position and to some degree also at *sn*-1 position, resulting in *sn*-1,3- and *sn*-2,3- DGs, respectively (113, 114). *PNPLA2* is transcriptionally regulated through the peroxisomal proliferator activator receptor (PPAR) α and γ (115, 116) TFs, as well as through the TF FOXO1 (102, 117). However, the predominant mode of ATGL regulation is through interaction with co-regulators in a post-translational manner. LD-bound ATGL requires association with Comparative Gene Identification 58 (CGI-58, *ABHD5*), a strong activator of ATGL-dependent lipolysis (118). CGI-58 can also associate with other proteins, like the LD-associated perilipin-1 (*PLIN1*) or *PNPLA3*, causing lower lipolytic activity through decreased activation of ATGL (119, 120). In 2010, two proteins were identified as negative regulators of ATGL: hypoxia inducible protein 2 – also called hypoxia inducible lipid droplet associated protein (HILPDA, *HIG2*) – and the G0/G1 switch gene-2 (*G0S2*) (121, 122). In later studies, both inhibitory proteins of ATGL, G0S2 and HILPDA, were found to be regulated by PPARα (123, 124). HILPDA is also strongly regulated by hypoxia through hypoxia inducible factors (HIF) 1 and 2 (122).

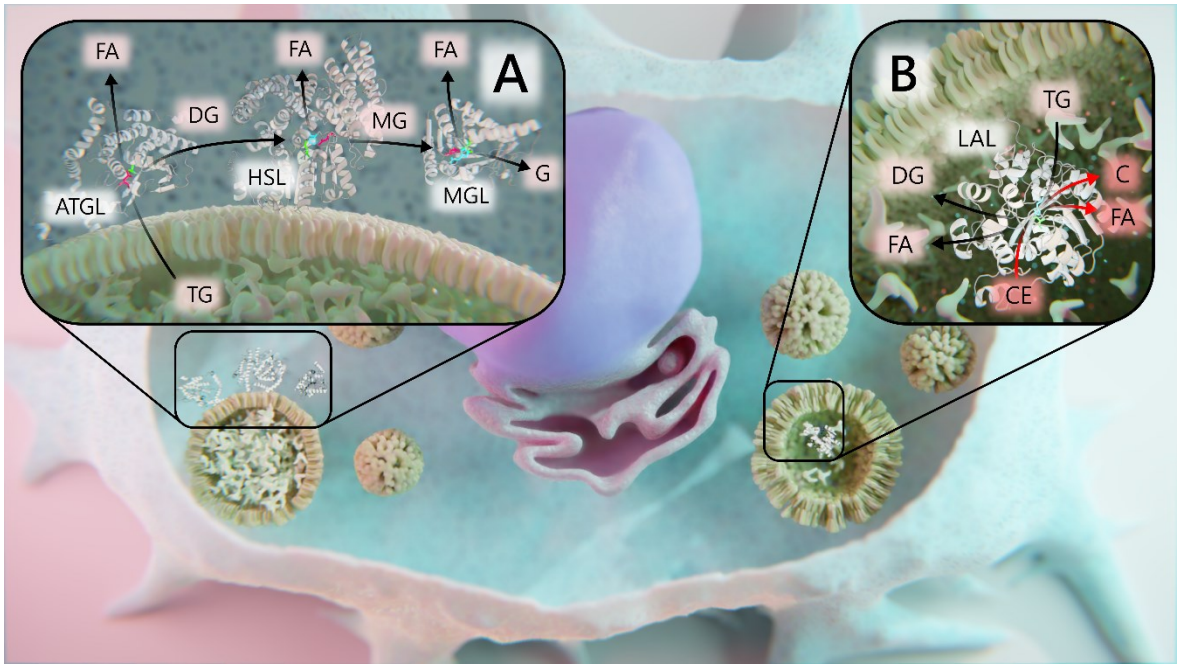

Figure 5: intracellular TG breakdown - lipolysis. A: neutral lipolysis happens at the lipid droplet at neutral pH through the enzymes ATGL, HSL, and MGL, releasing fatty acids (FA) and glycerol (G). B: acid lipolysis occurs in the lysosome and TG as well as CE hydrolysis is

catalyzed by LAL. Figure used from Honeder et al. 2023 (2) with permission from the publisher (CC BY 4.0 License)

The second step of neutral lipolysis is carried out by Hormone Sensitive Lipase (HSL), which was first described in 1964 (125). Before ATGL was discovered it was believed that HSL is the major intracellular neutral TG lipase, however, its TG hydrolysis activity is low compared to that of ATGL and loss of ATGL is sufficient to cause TG and LD accumulation (126). The preferred substrate of HSL is *sn*-1,3 DG, which is the main product of ATGL-mediated lipolysis (114). Although HSL is regulated by some TFs like the SREBP, the nuclear receptor family members LXR and RXR, or PPARα, it is primarily regulated at the post-translational level through phosphorylation (102, 116). The canonical way of lipolysis activation is through catecholamine binding to β-adrenergic G-protein-coupled receptors, which stimulates adenylate cyclase and leads to the synthesis of cyclic AMP (cAMP). cAMP, in turn, activates protein kinase A (PKA), which phosphorylates HSL and perilipin-1 at specific residues (127, 128). This phosphorylation causes HSL to move to lipid droplets (LD) and become enzymatically active, thus initiating the breakdown of stored lipids (127). In perilipin-1, PKA mediated phosphorylation causes its dissociation from CGI-58, which is then available to bind to and activate ATGL (129).

To complete intracellular neutral TG hydrolysis, the generated monoacylglycerols (MG) after the first two catalytic steps are degraded releasing the last FA and glycerol. Although several enzymes have been ascribed a MG hydrolysis activity, the main MG hydrolase in the canonical lipolysis pathway is Monoacylglycerol Lipase (MGL), which was described first in 1976 (130). MGL primarily cleaves FAs from both the *sn*-1 or *sn*-2 positions of MGs and is crucial for the inactivation of 2-arachidonoylglycerol (2AG), a potent endocannabinoid (131). MGL was shown to also have hydrolytic activity towards FA-ethyl ethers and prostaglandin-glycerol esters (132, 133). There are no MGL regulating posttranslational modifications or coregulators of MGL known, and the regulation of MGL happens at the transcriptional level primarily through PPARα, which also regulates the expression of *PNPLA2* and *LIPE* (gene for HSL) (102, 116). Another noteworthy MG hydrolase is α/β hydrolase containing-6 (ABHD6), a member of the α/β hydrolase

containing (ABHD) protein family. ABHD6 preferably cleaves FAs at *sn*-1 position but also shows hydrolase activity for lysoPL (102, 134).

1.2.2 Lipid Droplets

Lipid droplets (LD) are the storage site of the cell for excess lipids. These dynamic organelles are composed of a hydrophobic core – containing mainly triglycerides and cholesteryl esters (CE) – which is enveloped by a lipid monolayer consisting of phospholipids (135). Cells generate LDs through *de-novo* synthesis from the ER, where many enzymes of neutral lipid synthesis, such as acyl-CoA:cholesterol acyltransferase (ACTA) and DGAT, are located (136). TGs and CEs synthesized at the ER membrane first form an oil lens in the ER membrane. When a sufficient amount of TG has formed within the ER bilayer, the droplet buds into the cytosol, where it can further expand, and acquire LD associated proteins (137).

Two tissues associated with lipid storage are adipose tissue and the liver. Adipocytes and hepatocytes have increased capacity to store lipids and exhibit the highest levels of LDs. Nevertheless, LDs exist in virtually all cells, and their function within the cell goes far beyond fat storage (135). The scavenging of intracellular lipids and their subsequent storage in LDs is important for the protection of cells from lipotoxicity, which is caused by accumulated lipids such as FAs, glycerolipids or sterols (137). Furthermore, it is now recognized that LDs function as central hubs for various metabolic processes, and many proteins involved in LD metabolism are located on and around LDs (138). Proteins associated with LDs differ between different cell and tissue types. Among these LD-associated proteins in mammalian cells are Perilipins, which are important regulatory proteins, metabolic enzymes responsible for TG synthesis and degradation, as well as enzymes involved in phospholipid, retinol, and sterol ester metabolism (138). The major LD regulating proteins are Perilipins, which show distinct tissue distribution. Among the five perilipin proteins (PLIN1-5) in mammals, PLIN2 and PLIN3 are ubiquitously expressed, while PLIN1, PLIN4 and PLIN5 are expressed in a subset of tissues, with PLIN1 being specifically expressed in adipocytes (128).

In recent years, the accumulation of LDs in a variety of cancer cells has been reported (139). LD storage and degradation are closely linked to energy metabolism and cell signaling and LDs play a critical role in cancer cell proliferation, resistance to apoptosis, and aggressiveness (139). Increased uptake of FAs as well as *de-novo* lipid biosynthesis, a feature of many cancer cells, leads to increased lipid content. Increased LD level was observed in cancer cells that experience hypoxic conditions (140), and perilipin-2 was identified to correlate with high LD levels in hypoxic cancer cells (141). In another study, hypoxia-dependent increase in LD formation was associated primarily with increased FA uptake and concomitantly higher levels of FA binding proteins (FABP) 3 and 7 (FABP3 and FABP7), as well as perilipin-2 (99). Besides, it was found that LDs can play a protective role against lipotoxicity in cells by providing MUFAs like oleate from their TG stores, thereby helping to maintain an appropriate FA saturation level in the cell (142). TGs stored in LDs are also rich in PUFAs like arachidonic acid (AA), which is an important eicosanoid[15] precursor. In addition, some eicosanoid synthesis enzymes are found on LDs, which in turn makes LDs an important eicosanoid production site within the cell. Heightened levels of eicosanoids like prostaglandin[16] E2 (PGE_2) have been associated with tumors, and eicosanoids were found to promote tumor growth and invasion while suppressing anti-tumor immune response (139, 144, 145). Signaling-associated proteins like phosphatidyl inositol 3 kinase (PI3K), extracellular signaling regulated kinases (ERK1 and ERK2), p38, protein kinase C (PKC), and caveolin, have also been discovered on lipid droplets (LDs), suggesting that LDs might act as vital hubs for rapid proliferative signaling in the cytoplasm (146, 147, 148).

Elevated LD levels in cancer are often related to increased *de-novo* lipid synthesis and FA uptake. In contrast, the degradation of LD and the enzymes involved in it receive less attention but may play an important role in the context of some cancers.

[15] Eicosanoids are bioactive lipids that have been linked to a number of health problems, including inflammation and cancer. They include substances such as prostaglandins and leukotrienes (143).
[16] Prostaglandins are a group of biologically active lipids that are derived from arachidonic acid (AA), a poly-unsaturated 20-carbon FA, and modified through oxidation (144)

Chapter One: Lipid hydrolases and their influence on non-small cell lung cancer cell lines

2 Introduction to lipid hydrolases in the context of cancer cells

The first enzyme involved in the breakdown of TGs from LDs is ATGL, which is activated by CGI-58. Typically, loss-of-function mutations in *PNPLA2*, the gene encoding for ATGL, are associated with neutral lipid storage disease with myopathy (149), while CGI-58 deletion is associated with Chanarin-Dorfman syndrome, a version of neutral lipid storage disease which clinically also presents itself with ichtyosis[17] (150). Because ATGL knockout (KO) in mice causes severe heart dysfunction, which ultimately leads to premature mortality, ATGL rescue in the heart of whole-body ATGL-KO mice is required to study the systematic effect of ATGL-KO (151). Strikingly, under those conditions, mice spontaneously develop neoplasia in the lung, which can advance into lung adenocarcinoma (152). More recently, ATGL-mediated PPARα signaling has been found to play a crucial role in bronchiolar epithelial cells and ATGL loss is detrimental to lung regeneration (153). However, in several human cancers, including lung cancer, ATGL was found to be downregulated (152). In a study from our lab, ATGL-KO in a lung cancer cell line promoted a more aggressive cancer phenotype, as observed by increased migration and oncogenic signaling (154). The expression of ATGL was also found to inversely correlate with proliferation in mouse embryonic fibroblasts (MEF), which was attributed to reduced AMPK phosphorylation and apoptosis (155). Silencing of ATGL in a panel of cancer cell lines, on the other hand, did not corroborate these findings. However, it is worth noting that in this study, silencing of ATGL did not reduce TG hydrolysis activity in cancer cell lines, and that cancer cell proliferation was reduced by increasing ATGL-mediated TG hydrolysis (155).

Reduction of ATGL activity may also be a result of decreased CGI-58 availability, or inhibition of ATGL by G0S2 or HILPDA. Decreased CGI-58 availability may be the result of decreased expression of *ABHD5*, the gene encoding for CGI-58, or increased binding to perilipin proteins. *ABHD5* is frequently lost in human colorectal carcinomas, causing

[17] Ichtyosis is a rare skin disorder presenting with irregular epidermal maturation and skin barrier defects (150)

malignant transformation (156), and it was also reported that CGI-58-mediated increase in lipolysis causes decreased growth in prostate cancer (157). Several perilipins, particularly *PLIN2* and *PLIN3* in lung cancer, have been associated with cancer development and progression and contribute to LD accumulation in cancer (158, 159). *PLIN2* expression is stimulated by HIF1α and thus contributes to the increase of LDs under hypoxic conditions (99). In addition, the ATGL regulatory protein HILPDA is also induced by HIF1α and thereby promotes the inhibition of ATGL and intracellular lipolysis (160). The other ATGL inhibitory protein, G0S2, on the other hand, was found to diminish cancer growth through lowering ATGL activity in lung cancer cells (161). Most of the other studies, however, suggest an anti-neoplastic/tumor-suppressive effect of ATGL in cancer (162).

Contrarily, MGL was found elevated in aggressive human melanoma, ovarian as well as breast cancer cells, and it was proposed to promote oncogenic lipid signaling, that drives migration, invasion, survival, and tumor growth (163). However, MGL expression was found to be generally reduced in primary colon tumors compared to normal colon, and its overexpression (OE) resulted in reduced tumor cell line colony formation (164). The same study also showed that MGL was reduced in tumors of the breast and lung when compared to paired normal tissue. In a later study by the same group, MGL-deficient mice showed an increased occurrence of tumors in various organs, with lung neoplasia being the predominant abnormality. Furthermore, MGL-KO MEFs showed markedly higher cell proliferation when compared to wild-type MEFs (165).

The ambiguity about the impact of individual lipid hydrolases in cancer, which emerges from these studies, prompted us to ask the question about the role of lipid hydrolysis and lipolytic enzymes in the context of lung cancer in a broader sense.

Within the framework of this thesis, we aimed to build on previous work from our lab (154) through investigation of ATGL-KO cells in a more *in-vivo*-like (3D) cell culture system. Furthermore, we aimed to broaden our investigations of lipid hydrolases in the context of lung cancer by generating additional lipolysis-deficient cell lines through ATGL- or MGL-KO in NSCLC cell lines of different histological subtype and mutational status.

3 Material and Methods

Part of this section has been adapted or taken from Honeder *et al.*, MCP 2021.

3.1 Cell lines and cell culture conditions

The following cell lines were used in this thesis: A549 (#300114, CLS, Germany), A549, NCI-H1299, NCI-H358, and NCI-H441 (#CCL-185, #CRL-5803, #CRL-5807, #HTB-174, respectively, ATCC, USA). All cell lines were cultured at 37 °C and 5 % CO2 in Rosswell Park Memorial Institute-1640 (RPMI) medium with phenol-red and 2 g/L of glucose (RPMI-1640, #R0883, Merck) supplemented with 10 % Fetal Bovine Serum (FBS) and with 2 mM L-Glutamine (#25030081, Gibco), and 50 Units/ml Penicillin 50 µg/ml Streptomycin (1:100 from #15070063, Gibco). For cultivation in lipid-depleted medium, RPMI medium was supplemented with 10 % "lipid-stripped" FBS (166) but otherwise prepared as described above. All genetically modified cell lines that were generated for this thesis are summarized in Table 2.

3.2 CRISPR-Cas9 mediated gene KO generation

Genetic KO of *PNPLA2* (ATGL) in the A549 cell from CLS was achieved as reported in Honeder *et al.* (2021) (1). Briefly, an ATGL-directed or control plasmid from Santa Cruz Biotechnology (ATGL: #sc-401711, Control: #sc-418922) was used for Lipofectamine3000 (#L3000001, Thermo Fisher)-mediated transfection. The ATGL-directed plasmid was co-transfected with an RFP-containing homology-directed repair (HDR) plasmid (#sc-401711-HDR). The cells were subsequently single cell sorted by fluorescence activated cell sorting (FACS) according to high RFP intensity (ATGL-KO cell lines) or by serial dilution (control cell lines) to obtain single cell-derived clones. Because Santa Cruz Biotechnology plasmids are proprietary information, the vector details cannot be shown here. This prompted us to switch to a different method of generating genetic KOs by CRISPR-Cas9 in the panel of cell lines from ATCC for all further experiments.

Knockout of *PNPLA2* (ATGL) and *MGLL* (MGL) was achieved in the panel of NSCLC cell lines from ATCC (A549, H1299, H358, H441) through CRISPR-Cas9 methodology. Short

guide RNAs (sgRNAs) were designed using the CRISPick tool[18] by the Broad Institute. In brief, sgRNA oligos with a good CRISPick rank that are located on the same exon, approx. 50-150 base pairs apart, were chosen (Table 4) and used for cloning. The backbones for cloning were obtained from Addgene: pSpCas9(BB)-2A-GFP (#48138) (Figure 6A) and pU6-(BbsI)_CBh-Cas9-T2A-BFP (#64323) (Figure 6B), which express a fluorophore (GFP or BFP) for selection, and lentiGuide-Puro plasmid (#52963) (Figure 6C), which expresses puromycin N-acetyl-transferase gene for puromycin selection. All plasmid backbones (Figure 6A-C) also express a S. pyogenes sgRNA CRISPR customizable RNA element with a 5' and 3' BbsI restriction enzyme cut site for the introduction of the sgRNA. Two independent CRISPR-Cas9 approaches were used to generate ATGL- or MGL-KO cell lines.

In CRISPR-Cas9 approach 1, the deletion of ATGL or MGL in parental cell lines was attempted by transiently transfecting the target cell lines with plasmids containing genetic information for Cas9, a fluorophore (GFP (Figure 6A) or BFP (Figure 6B)) and sgRNAs targeting the gene of interest in the genome (Table 4). The plasmids were introduced using Lipofectamine™ 3000 Transfection Reagent (#L3000001, Thermo Fisher) according to the manufacturer's protocol. At first, the DNA amount for optimal transfection was determined for each target cell line (Table 3). 48 hours days after transfection, the cells were sorted for high BFP and GFP expression and collected as a polyclonal cell population.

For CRISPR-Cas9 approach 2, in a first step, target cell lines were infected with virus expressing the lentiCas9 blast plasmid (#52962, Addgene) (Figure 6D) - which contains genetic information for the S. pyogenes Cas9 as well as the Blasticidin S deaminase gene bsd, both under the EFS-NS promoter – for the generation of target cell lines that stably express Cas9. Cells were selected with 10 µg/ml blasticidin (#A1113903, Thermo Fisher) for a week or until all control cells (not infected with lentiCas9 blast) were dead, and subsequently kept at 5 µg/ml blasticidin. The Cas9 expressing parental cells were then subsequently infected with virus expressing the lentiGuide Puro plasmid containing the sgRNAs and selected with 2 µg/ml puromycin and 5 µg/ml blasticidin for 3 days or until all control cells were dead.

[18] https://portals.broadinstitute.org/gppx/crispick/public

The plasmid expressing virus was prepared by transfecting Lenti-X™ 293T cells using the TransIT-VirusGEN® Transfection Reagent (Mirus Bio, #) according to the user manual with following plasmids: pMDLg (Addgene, #12251), pMD2.g (Addgene, #12259), pRSV-REV (Addgene, #12259), and the respective target plasmid (e.g., lentiCas9 blast plasmid or lentiGuide Puro plasmid with sgRNA inserted).

All genetically manipulated cell lines generated were validated by western blot (ATGL and MGL) and in the case of ATGL-KO functionally validated by assessment of lipid droplets.

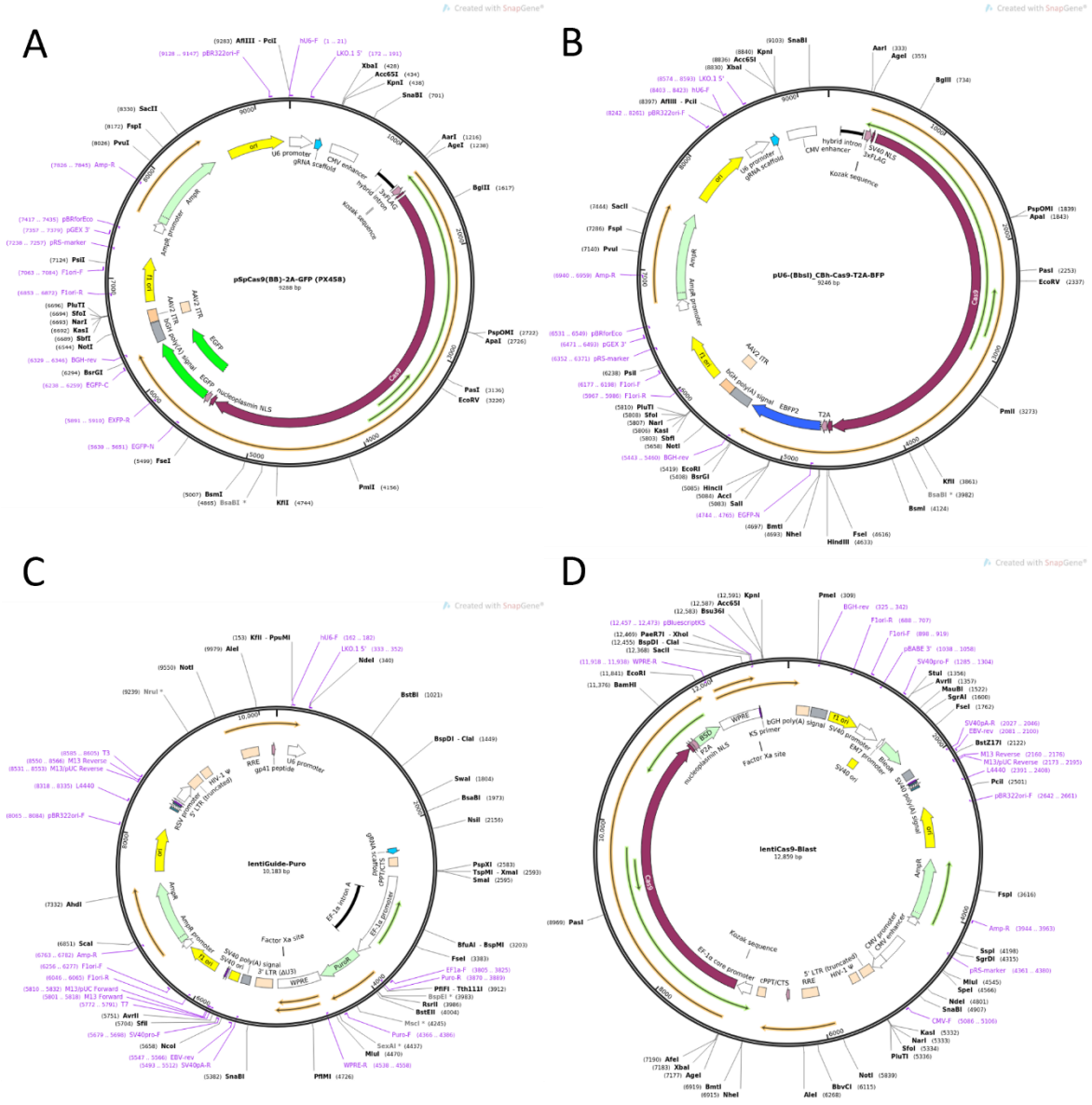

Figure 6: plasmids CRISPR-Cas9-mediated KO generation. A: plasmid pSpCas9(BB)-2A-GFP, containing Cas9 and GFP (#48138, Addgene); B: plasmid pU6-(BbsI)_CBh-Cas9-T2A-BFP,

containing Cas9 and BFP (#64323, Addgene); C: plasmid lentiGuide-Puro, containing puromycin N-acetyl-transferase (#52963, Addgene); D: plasmid lentiCas9 blast, containing Cas9 (#52962, Addgene)

3.3 Generation of cell spheroids- 3D cell culture

For the preparation of spheroids, cells were plated at 10,000 cells per well in 200 µl of medium into an Ultra-Low Attachment 96-well Plate (#7007, Corning). Spheroid formation was induced by centrifugation at 1,200 rpm for 20 minutes. The cells were kept in culture for a minimum of 10 days with medium exchange on days 4 and 8 (post plating).

For dissociation of spheroids to obtain a spheroid-derived cell suspension, 5 spheroids per cell line/condition were pooled and washed carefully with PBS. The spheroids were dissociated through incubation in Accutase cell detachment solution (#SCR005, Merck Millipore) at 37 °C for 10 minutes. Through careful pipetting, prior and post incubation, a spheroid-derived cell suspension was achieved.

3.4 qPCR

For qPCR experiments, RNA extraction was performed using TRIzol reagent (Invitrogen) according to manufacturer's protocol. Briefly, cells grown in 6-wells were harvested in 1 ml of TRIzol reagent (#15596026 , Thermo Fisher) at room temperature. Samples were incubated for 5 min prior addition of 200 µl chloroform. Samples were spun down at 12,000 x g at 4 °C for 15 min, and the upper aqueous phase was transferred into RNAse free Eppendorf tubes for RNA extraction. 500 µl isopropanol was added to the RNA fraction, and the tubes were thoroughly inverted and incubated for 10 minutes followed by centrifugation at 12,000 x g at 4 °C for 10 min. The RNA pellet was washed with ethanol, redissolved in 50 µl of RNase free water. The quality and concentration of RNA was assessed on a NanoDrop spectrophotometer.

RNA was reverse transcribed into cDNA with the QuantiTect Reverse Transcription kit (#205311, Qiagen) according to manufacturer's protocol. Briefly, samples corresponding to 1 µg RNA were incubated with gDNA wipeout buffer to get rid of any transferred genomic

DNA. A master mix containing reverse transcriptase, reverse transcriptase buffer (including nucleotides) as well as reverse transcription primer mix was added to the RNA samples and incubated for 15 min at 42 °C followed by incubation for 3 min at 95 °C and storage of cDNA at -20 °C.

For qPCR, cDNA samples were diluted 1:5 in RNase free water (= ca. 10 ng / µl) and RNA primer working solutions were prepared by diluting 100 µM primer stocks 1:10 to yield 10 µM of each primer e.g., 80 µl nuclease-free H_2O + 10 µl primer forward (100 µM) + 10 µl primer reverse (100 µM). Primer sequences for *PNPLA2* and two housekeeping genes (*ACTB*, *EEF1A1*) are shown in Table 1. A master mix was prepared with 5 µl Maxima SYBR Green/ROX qPCR Master Mix (2X) (#K0221, Thermo Fisher), 0.4 µl RNA working solution and 3.6 µl nuclease-free water per reaction. The primer-specific master mix was distributed (9 µl) into the wells of a hard shell 384-well plate (Bio-Rad), and subsequently, 1 µl of cDNA was added to the wells, the plate was sealed, briefly spun down and placed in a CFX384 real-time PCR detection system (BioRad).

For data analysis, delta Ct values (ΔCt) and fold change (= 2^ΔCt) were calculated by subtracting the mean Ct value of *PNPLA2* from the mean Ct value of the combined housekeeping genes (*ATCB* + *EEF1A1*). The fold change was then normalized to the mean of the control cell lines.

3.5 Western Blot

Cells from a 6-well (2D cell culture) or a minimum of 5 spheroids (3D cell culture) were harvested in 100 – 200 µl of 1x CST buffer (#9803, Cell Signaling Technology) or RIPA buffer (#BP-115, Boston BioProducts), each constituted with 1:100 Protease/Phosphatase Inhibitor (#78440, Thermo Fisher). Protein quantification was performed using Pierce™ BCA protein assay (#23225, Thermo Fisher) or Bradford protein assay (#5000006, Biorad). The separation of proteins was performed on precast NuPAGE 4-12 % Bis-Tris Midi Protein Gels or Bolt™ 4-12 % Bis-Tris Plus Gels (both Invitrogen™), followed by blotting of the proteins onto a 0.45 µm nitrocellulose membrane (Amersham). Blotting was performed through semidry method at 220 mA for 1-2 hours or in a wet chamber at 30 V for 16 hours. Unoccupied sites on the membrane were blocked by 5 % skim milk in Tris-buffered saline

containing 0.1 % Tween 20 (TBS-T). Following primary antibodies were used: ATGL (#2138S, Cell Signaling Technologies), MGL (#PA5-27915, Thermo Fisher), GLUT1 (#ab128033, Abcam), GLUT3 (#sc-74497, Santa Cruz Biotechnology), SCD1 (#2794, CST), FADS2 (#PA5-87765, Invitrogen), β-Actin (#A5441, Sigma Aldrich), Vinculin (#4650, Cell Signaling Technologies). Primary antibodies were diluted 1:1000 in 5 % BSA (ATGL, MGL, GLUT1, GLUT3) or 1:5000 in 5 % BSA (Actin, Vinculin). Incubation with primary antibody solutions was performed overnight at 4 °C on a shaker. Membranes were washed with TBS-T, followed by incubation for 1 hour at room temperature with diluted (1:5000) secondary antibody in TBS-T: anti-rabbit horseradish peroxidase (HRP)-linked antibody (Cell Signaling Technology). The bands were detected after ECL application (#32106, Thermo Fisher, or #1706061, Biorad) on a ChemiDoc System (BioRad) or an ImageQuant™ LAS4000 biomolecular imager (GE Healthcare) after application of Clarity Western ECL Substrate (#1705061, Biorad). Analysis of acquired images was performed by ImageLab (version 5.2) or FIJI (1.54d version, Java 1.8.0_345 version) (167).

3.6 Lipid droplet assessment

Lipid droplet assessment was performed through microscopy or flow cytometry.

For the microscopy method the cells were plated into glass-bottom cellview cell culture dishes (#627965, Greiner Bio One) and allowed to attach overnight (2D cell culture) or for 4 h (after spheroid dissociation). The cells were then carefully washed with phosphate buffered saline (PBS) and incubated with 2 µM BODIPY™ (#D3922, Invitrogen; 1000 x from a 2 mM stock in PBS) for 10 min at 37 °C. The cells were then washed carefully and fixed in 3.7 % formaldehyde solution for 10 min at 37 °C. The cells were then mounted in 25 µl Vectashield Antifade Mounting medium with DAPI (#H-1200-10, Vector Laboratories). Images of LDs were acquired on a Nikon A1+ confocal laser scanning microscope. Images were further analyzed with FIJI (167), and LD volume was quantified and normalized to cell count.

The flow cytometry method was adapted from Qiu and Simon (2017) (168). Briefly, cells were plated in a 6-well plate to reach 70-90 % confluency the next day. Cells were washed with PBS carefully and incubated with 2 µM BODIPY™ (#25892, Cayman Chemical

Company) in PBS for 15 min at 37 °C. Cells were then washed with PBS, trypsinized, quenched with medium and transferred into flow tubes through a 35 µm strainer cap to avoid cell clumps. Flow cytometry was performed on a FACS LSR II flow cytometer (BD Biosciences) equipped with a 488 laser and 530/30 filter to assess BODIPY™ intensity. The median of BODIPY™ positive cells was assessed with the BD FACSDiva software (version 8.0). To test the sensitivity of this method parental cell lines were incubated with 30 µM oleic acid-BSA conjugate (#O3008, Merck) or 5 µM DGAT1 inhibitor (PF-04620110, #16425 Cayman Chemical) and 5 µM DGAT2 inhibitor (PF-06424439, #17680 Cayman Chemical) for 24 hours, as a positive and negative control, respectively.

3.7 Cell proliferation/imaging

For the assessment of proliferation of cells in 2D cell culture, a microscopy method that tracks the confluency of cells in a plate, or cell counting was employed.

For the microscopy method, 80,000 cells were plated in duplicates into the wells of a 12-well plate (VWR). The cell confluency was observed at 7 positions in each well under a Zeiss Cell Observer microscope, and an image was taken hourly for up to 48 hours. The images were subjected to analysis by FIJI (167) running an in-house generated automated confluency analysis. The resulting growth curves (mean values of confluency over time) the slopes of the exponential growth phase were extrapolated and compared.

To determine proliferation rates (doublings/day) of cells (2D or 3D cell culture), cells were counted at timepoint 0 and at a later timepoint and doublings/day were calculated. For 2D cell culture, cells were plated at roughly 15,000 cells per well of a 12-well plate and allowed to attach overnight. Cell counts were determined by trypsinizing and quenching the cells to yield a total of 1 ml cell suspension at timepoint 0 and after 24-96 hours (depending on proliferation rate). For 3D cell culture spheroids were counted on days 0, 8, and 11 post plating. Spheroids were washed, suspended in 100 µl Trypsin, and after proper dissociation the suspension was quenched with 100 µl to yield 200 µl cell suspension total. Cell counts were subsequently performed using a Multisizer 3 Coulter Counter (Beckman Coulter) with diameter settings between 10 µm and 30 µm. Cell doubling/day was calculated with following formula:

$$doublings/day = \frac{\log\left(\frac{mean(cell\ count\ t=0)}{mean(cell\ count\ t=x)}\right)}{\frac{\log(0.5)}{time\ [days]}}$$

3.8 Spheroid Imaging

For the determination of spheroid size and circularity, spheroids were imaged in an Okolab stage top incubator with a Nikon TiE-2 microscope equipped with an Andor Zyla 4.2sCMOS camera. The wells containing the spheroids were scanned by an automated acquisition program that was established using the JOBS module of the imaging software NIS Elements (V5.20.01). For each well/spheroid, a brightfield z-stack (range 600 µm, 30 µm step size) was acquired at 100 x magnification. The NIS Elements General Analysis 3 tool was used to perform an automated analysis for size and shape (including Area and Perimeter estimation of the best focus plane). Using the Area and Perimeter values for each spheroid, the circularity of spheroids was calculated with the following formula:

$$\boldsymbol{Circularity = \frac{4 * \pi * Area}{Perimeter^2}}$$

The max. value for circularity is 1 for a perfect circle, and the value decreases as the values for the perimeter increase, meaning a less circular spheroid.

3.9 Spheroid Histology

For histological analysis, the harvested spheroids were fixed overnight in a solution of 4 % paraformaldehyde, followed by an ethanol series-mediated dehydration, and washing with toluene. The tissue was then embedded in paraffin and stored at 4 °C. The tissue blocks were cut into sections of 5 µm thickness with a semiautomated rotary microtome RM2245 (Leica Biosystems). For immunohistochemistry (IHC) staining, the deparaffinized and rehydrated sections were treated with antigen retrieval solution, followed by incubation Ki67-specific primary antibody (#GA62661-2, Dako Agilent) at a dilution of 1:50. HRP-mediated detection was carried out after incubation with an anti-mouse antibody and an HRP/3,3'-diaminobenzidine detection kit (Ultravision, Thermo Fisher). An Olympus BX53 with an Olympus cellSens Dimension 1.18 software (Olympus Corporation) was used to take pictures of the stained sections and for analysis.

3.10 Live and Dead Cell Estimation

The dissociated cells from spheroids (day 10) were incubated with 1:1000 SYTOX™ Red dead-cell stain (#S34859, Invitrogen) for 10 min at 37 °C. Subsequently, flow cytometry was performed on a cytoFLEX LX flow cytometer and single cell count as well as the percentage of dead cells was assessed with the CytExpert software (version 2.3.1.22).

3.11 Chorioallantoic Membrane Assay

For the chorioallantoic membrane assay (CAM) ex-ovo method (169), fertilized white Lohmann chicken eggs were incubated under standard conditions (37 °C and 60 % humidity). On day 3 of embryonic development, the eggshell was cracked, and the embryos were incubated in sterile dishes until day 9 of embryonic development, when A549 ATGL-KO and Control spheroids (day 10) were transferred onto the CAM. For each egg, there were three designated on-plant areas with each 5 spheroids of the same cell line (i.e., ATGL-KO clone 1). The cell lines were distributed randomly across the different on-plant areas and eggs to minimize potential egg-related bias. The chick embryos were further incubated for 5 days post spheroid transfer, after which the newly formed tumors were collected, washed and rapidly frozen. For proteomics analysis, two on-plants from each of the ATGL-KO cell lines (n = 3) or control cell lines (n = 3) were used.

3.12 Fatty Acid Methy Ester (FAME) Extraction and Measurement

Spheroids (n = 5) of each A549 (CLS) ATGL-KO or A549 (CLS) Control clonal cell line were pooled, dissociated in Accutase as described above, followed by addition of 100 µl H_2O, 300 µl methanol, and 1 ml methyl-tert-butyl ether (MTBE) containing 1 µg of C15:0 internal standard (methyl pentadecanoate) (Sigma Aldrich, #76560). After lipid extraction by 10 min sonication, followed by centrifugation at 2000 x g for 10 min to separate the phases, the organic phase was transferred to a new tube. After re-extraction of the aqueous phase (120 µl H_2O, 120 µl methanol, and 400 µl MTBE), the organic phases were combined and dried under a N_2 stream. Derivatization of the lipid extracts was achieved by hydrolysis and esterification of FAs in 200 µl sodium hydroxide (0.1 M) in methanol for 10 min at 80 °C and 5 min on ice. After addition of 200 µl boron trifluoride (#B1252, Sigma Aldrich) the fatty acid methyl ester (FAME) samples were further incubated for 10 min at 80 °C and 5 min on ice. The FAMEs were extracted into cyclohexane through

addition of 200 µl saturated NaCl and 400 µl cyclohexane and overhead rotation for 5 min. After phase separation through 2000 x g centrifugation for 5 min, the cyclohexane phase was transferred to a new tube and the samples were re-extracted with 200 µl cyclohexane. The cyclohexane phases were combined and dried under stream of N_2. The samples were dissolved in 200 µl dichloromethane (DCM). Before measurement, they were further diluted 1:5 in DCM and measured on a Scion 436-GC system (Bruker, Germany). The inlet temperature was set to 280 °C and 1 µl of sample was injected in a 1:20 split. The carrier gas (Helium) was set to a flowrate of 1 ml/min, and the oven temperature was ramped from 50 °C to 300 °C after 1 min with a rate of 20 °C/min and held at 300 °C until 30 min. The GC was coupled to an amaZon speed ETD ion trap mass spectrometer (Bruker, Germany), which was operated in positive ion mode and scanned in a mass range between 100 and 1000 m/z. Data analysis was performed with Lipid Data Analyzer (version 2.7.0). FAME species were normalized to the internal standard and protein content, and FA ratios or abundances were normalized to the control group.

3.13 Metabolic tracing: stable isotope labeling and extractions

For metabolic tracing experiments to trace the fate of glucose into downstream metabolites, RPMI without glucose (#R9011, USBiological Life Sciences) was prepared and reconstituted with [U-^{13}C] (= labeled) glucose (#CLM-1396, Cambridge Isotope Laboratories, Inc.) or [U-^{12}C] (= unlabeled) glucose, and with regular or delipidated FBS.

Cells were seeded at 50,000 cells per well in a 6-well plate and cultured overnight. Prior to the experiment, the cells were washed three times with PBS and then cultured in 4 ml media containing 11 mM glucose and the indicated treatment condition (i.e., tracing medium or non-tracing medium and lipids or non-lipid medium). At each timepoint (6 h, 24 h, 48 h, 72 h) cells in non-tracing medium were counted and cells in tracing medium were harvested. For harvest, cells were washed quickly in cold blood bank saline and lysed in 700 µl of lysis buffer. Lysis buffer consisted of Methanol (constituted with 25 mg/l butylated hydroxytoluene) with 0.88 % KCl in a ratio of 4:3 (MeOH/KCl). 1.5 µg/ml C17:1 fatty acid was added as internal standard for the extraction of polar fatty acids. Samples were scraped and transferred into glass vials containing 800 µl DCM, followed by 15 min vortex at 4 °C. After centrifugation at 3,500 x g for 10 min at room temperature, the lower, lipid-containing

DCM phase was transferred to a new glass vial and the upper, polar metabolite aqueous phase was transferred into an Eppendorf tube – both fractions were dried under stream of nitrogen.

3.13.1 FAME derivatization

For the derivatization of FAMEs, the lipid pellets were dissolved in 100 µl toluene. 200 µl of 2 % sulfuric acid in MeOH was added and incubated at 50 °C overnight. 500 µl of 5 % NaCl was added to the samples and extracted twice with 500 µl of hexane. The hexane phases were collected in glass MS vials and dried under nitrogen. The dried samples were dissolved in 50 µl of hexane and measured via GC-MS.

3.13.2 GC-MS metabolite measurement

For the measurement of fatty acid methyl ester (FAME) samples, a DB-FastFAME GC Column (30 m x 0.25 mm x 0.25 µm, Agilent J&W Scientific) was used in an Agilent 7890 GC coupled to an Agilent 5975C MS. 1 µl of sample was injected in splitless mode (timepoints 6 h, 24 h, 48 h) or 1:1 split mode (72 h) at a temperature of 270 °C. Separation was carried out using a temperature gradient starting at 100 °C for 5 min, increasing to 180 °C at 8 °C/min, followed by a ramp to 230 °C at 1 °C / min. For data analysis, the raw data were converted to *.mzML* files using MSConvert (ProteoWizard) (170). The data was then checked in the software El maven (171) corrected for naturally occurring isotopes using an R script based on IsoCorrectoR (172). Fractions of a metabolite (e.g., palmitate) refer to the fraction of this metabolite with different levels of incorporated ^{13}C-atoms from ^{13}C-labelled glucose and are thus intrinsically normalized to the total amount of that metabolite (all fractions always add up to 1). Peak areas (AUC), reflecting metabolite abundance, were first normalized to the C17:1 standard for each individual measurement and finally AUCs were normalized to the cell count. Metabolite pools (e.g., palmitate pool) were calculated by adding up the normalized (to internal standard and to cell count) AUCs of each fraction for each metabolite.

3.14 Glucose and lactate measurement in media

To assess lactate production, glucose consumption, and glutamine consumption bioluminescent assays (Lactate (#J5021), Glucose (#J6021), Glutamine/Glutamate (#J8021)

Glo™ Assay, Promega) were employed. The assays were conducted according to the manufacturer's instructions using a LumiStar luminometer (BMG Labtech). In brief, cells were plated in 96-well plates at 10,000 cells / 100 µl medium. At t = 0 as well as after 24, 48 and 72 hours (2D cell culture) or after 1, 7, 8, 9, 10 and 13 days in culture (3D cell culture), aliquots of medium were removed and stored at -20 °C until measurement. Glucose, lactate, and glutamine were measured in the media samples. External calibration curves allowed the calculation of metabolite concentrations.

In an additional experiment, glucose and lactate concentrations in media was measured using a YSI 2900 bioanalyzer. Cells were grown in 6-well plates in triplicates and medium was taken at t = 0 and after 24 h of exponential growth. Cells were counted at t = 0 and t = 24 h. Glucose consumption and lactate production was normalized to cell number.

3.15 Label-free quantitative proteomics

For proteomics experiments, cells, spheroids, or CAM-tumors are washed in PBS and lysed in proteomics lysis buffer, consisting of 10 mM tris(2-carboxyethyl) phosphine (TCEP), 40 mM chloroacetamide (CAA), 1 % sodium dodecyl sulphate (SDS) in 100 mM TrisHCl (pH = 8.5). After sonication with a sonication probe (amplitude = 70 %, 10 sec, or until cells/tissue was lysed), cell debris is removed by centrifugation (14,000 x g, 5 min, 4 °C). The samples are transferred into new Eppendorf tubes and heat-denatured (95 °C, 10 minutes). Protein estimation by Pierce™ BCA protein assay (#23225, Thermo Fisher) is performed and 50 – 100 µg of protein are precipitated by acetone precipitation at -20 °C overnight. After centrifugation at 14,000 x g, 10 min, 4 °C, the pellet is dissolved in 25 % trifluoroethanol (TFE) and brought to 10 % TFE with 100 mM ammonium bicarbonate. The spheroid and spheroid-derived CAM tumor samples were then digested through incubation with 1:100 MS Grade LysC endopeptidase (#9051, Thermo Fisher) for 2 hours followed by incubation with 1:100 MS Grade Trypsin protease (#90305, Thermo Fisher) at 37 °C. The samples were then desalted using self-packed 2-layer 200 µl styroldivinylbenzol – reversed phase sulfonate (SDB-RPS) Stage Tips (#2241, Empore SPE Disks, Sigma-Aldrich), prior to LC-MS/MS measurement. The NSCLC cell line samples were digested in 1:50 sequencing grade modified trypsin (#V5111, Promega) overnight at 37 °C, followed by loading 500 ng of

sample onto Evotips™ according to the Evosep One sample preparation workflow (173) prior to measurement by LC-MS/MS.

3.15.1 Spheroids

The desalted samples were diluted in 0.1 % formic acid, 5 % acetonitrile (ACN), and 1 µg of sample was injected for LC-MS/MS analysis. The samples were first concentrated on an enrichment column (C18, 5 µm, 100 Å, 20 × 0.1 mm, Thermo Fisher Scientific) for 6 min with a flow rate of 5 µl / min, followed by chromatographic separation on a C18 nanocolumn (Acclaim PepMap RSLC: 2 µm, 50 × 75 µm, Thermo Fisher Scientific) at 60 °C with a flow rate of 0.3 µl / min and the following gradient: 4 – 25 % B, 154 – 159 min: 25 – 95 % B, 159 – 169 min: 95 % B, 169.1 – 184 min: 4 % B (running buffer A: 0.1 % formic acid, 5 % ACN, running buffer B: 0.1 % formic acid in pure ACN). LC was coupled to a Bruker maxis Q-TOF mass spectrometer operated in positive ion mode and data dependent acquisition (DDA).

Data search was performed using MaxQuant (version 1.6.14.0) (174) with a SwissProt human FASTA file (downloaded April 2019) – including common proteomics contaminants[19] – as a database. Protein quantitation was based on label free quantitation (LFQ), with a minimum of two (unique and razor) peptides per protein as requirement for quantitation. Match between runs (MBR) was enabled in a 1 min retention time window and a 20 min alignment window. Data analysis was performed using Perseus (version 1.6.13.0) (175). LFQ values were log2 transformed and after removal of contaminants, the matrix was filtered to contain at least three valid values in at least one group. Missing values were imputed from normal distribution. Differentially expressed proteins were identified through unpaired student t tests with Benjamini-Hochberg FDR correction of 5 % to correct for multi-testing.

3.15.2 CAM tumors

The desalted spheroid-derived CAM tumor samples were diluted in 0.1 % formic acid, 5 % (ACN), and 1 µg sample was injected. Peptide separation was carried out on an Aurora Series UHPLC C18 column (250 mm × 75 µm, 1.6 µm, Ionopticks) with a flow rate of 0.25 µl / min and the following gradient: 0 – 18 min: 2 % B, 18 – 160 min: 2 – 25 % B, 160 –

[19] https://www.thegpm.org/crap/

167 min: 25 – 35 % B, 167 – 168 min: 35 – 95 % B, 168 – 178 min: 95 – 2 % B (running buffer A: 0.1 % formic acid, 5 % ACN, running buffer B: 0.1 % formic acid in pure ACN). Mass spectrometry was performed on Orbitrap Velos Pro (Thermo Fisher Scientific) operated in positive ion mode and DDA.

Data search and analysis was performed as described above for 3D spheroids, with some minor differences. Due to the cultivation method of the spheroids on the chicken embryo, the harvested tumors contained proteins from human and chicken. The data was therefore also searched against a TrEMBL chicken database (FASTA downloaded March 2019) with same search parameters, but only unique peptides were allowed for LFQ quantitation, and the list of proteins was finally reduced to contain only human proteins, and the LFQ of each individual protein was normalized on the sum of all human protein LFQs for each sample.

The MS proteomics data for ATGL-KO and Control 3D spheroids and spheroids grown on CAM have been deposited to the ProteomeXchange Consortium via the PRIDE (176) partner repository with the dataset identifier PXD021105.

3.15.3 NSCLC (Cas9) cell lines

A549, H1299, H358 and H441 (Cas9) control (NTC), ATGL-KO (ATGL) and MGL-KO (MGL) cells were grown as biological triplicates in 6-well plates. The samples prepared on the Evotips™ were measured on an Evosep One (173) with the Whisper 40 samples per day (SPD) method at a gradient flow of 100 nl / min over the course of 31 minutes. Evosep One was coupled to a timsTOF (Bruker, Germany) Pro-HT mass spectrometer operated in positive data independent acquisition (DIA) parallel accumulation-serial fragmentation (PASEF) mode with trapped ion mobility spectrometry (TIMS) enabled with a 100 ms cycle time (100 % duty cycle).

The protein search was carried out using Dia-NN (177) with the following settings: library-free search with library generation (FASTA provided: swiss prot human database downloaded July 2022); fixed modification: cysteine carbamidomethylation; variable modification: oxidation on methionine; peptide length range: 7 – 30; precursor charge range: 1 – 4; precursor m/z range: 30 – 1800; Fragment ion m/z range: 200 – 1800; 0.01

FDR filtering; protease: trypsin; max. missed cleavages: 2; match between run enabled. The data analysis was performed using the Perseus software (version 2.0.9.0) (175). Volcano plots were visualized with R (version 4.3.1) and LFQ intensity plots were visualized with Graphpad Prism (version 8.2.0).

The MS proteomics data for ATGL-KO, MGL-KO and Control (NTC) NSCLC cell line experiments have been deposited to the ProteomeXchange Consortium via the PRIDE (176) partner repository with the dataset identifier PXD046912.

Table 1: primer sequences for qPCR

gene	direction	sequence 5' - 3'
PNPLA2	forward	GAGATGTGCAAGCAGGGATAC
	reverse	CTGCGAGTAATCCTCCGCT
LIPE	forward	TCAGTGTCTAGGTCAGACTGG
	reverse	AGGCTTCTGTTGGGTATTGGA
MGLL	forward	TCGTCAGGGATGTGTTGCAG
	reverse	AGGCGAAATGAGTACCATGCC
HIG2	forward	AAGCATGTGTTGAACCTCTACC
	reverse	TGTGTTGGCTAGTTGGCTTCT
ABHD5	forward	CACATGGTGCCCTACGTCTAT
	reverse	ACAGGTCTGTTGGTGCAAAGA
ACTB	forward	CATGTACGTTGCTATCCAGGC
	reverse	CTCCTTAATGTCACGCACGAT
EEF1A1	forward	TGTCGTCATTGGACACGTAGA
	reverse	ACGCTCAGCTTTCAGTTTATCC

Table 2: list of generated cell lines

parental cell line	Lineage	Lineage Subtype	Mutations	code	Cas9 expression	comments
A549	Lung, primary	NSCLC, LUAD	KRAS (p.G12S), STK11 (p.Q37*), TP53 (WT), KEAP1 (p.G333C)	A549 Cas9 NTC	✓	ATGL, MGL expression confirmed
				A549 Cas9 ATGL-KO	✓	No ATGL expression: **KO confirmed**
				A549 Cas9 MGL-KO	✓	No MGL expression: **KO confirmed**
				A549 GFP/BFP NTC	x	ATGL, MGL expression confirmed
				A549 GFP/BFP ATGL-KO	x	ATGL expression: **no KO**
				A549 GFP/BFP MGL-KO	x	MGL expression: **no KO**
H1299	Lung, metastatic	NSCLC, LCLC	NRAS (Q61K), STK11 (WT), TP53 (WT), KEAP1 (WT)	H1299 Cas9 NTC	✓	ATGL, MGL expression confirmed
				H1299 Cas9 ATGL-KO	✓	No ATGL expression: **KO confirmed**
				H1299 Cas9 MGL-KO	✓	No MGL expression: **KO confirmed**
				H1299 GFP/BFP NTC	x	ATGL, MGL expression confirmed
				H1299 GFP/BFP ATGL-KO	x	ATGL expression: **no KO**
				H1299 GFP/BFP MGL-KO	x	MGL expression: **no KO**
H358	Lung, primary	NSCL, LUAD	KRAS (p.G12C), STK11 (WT), TP53 (WT), KEAP1 (WT)	H358 Cas9 NTC	✓	ATGL, MGL expression confirmed
				H358 Cas9 ATGL-KO	✓	No ATGL expression: **KO confirmed**
				H358 Cas9 MGL-KO	✓	No MGL expression: **KO confirmed**
H441	Lung, metastatic	NSCL, LUAD	KRAS (p.G12V), STK11 (WT), TP53 (p.R158L), KEAP1 (WT)	H441 Cas9 NTC	✓	ATGL, MGL expression confirmed
				H441 Cas9 ATGL-KO	✓	No ATGL expression: **KO confirmed**
				H441 Cas9 MGL-KO	✓	No MGL expression: **KO confirmed**

Table 3: DNA amount for optimal lipofectamine transfection (per well of a 12-well plate)

target cell line	A549	NCI-H1299	NCI-H358	NCI-H441
DNA amount (ng)	250	1000	750	1000

Table 4: sequences of sgRNAs for cloning into plasmid backbones

Species	Gene	Use	Primer Name	Sequence (5‘-3‘)	Backbone:	Enzyme	Plasmid
Hs	PNPLA2	sgRNA	KA672_HsPNPLA2_1_F	caccgCATTCTCGCCGTCTGACACG	pSpCas9(BB)-2A-GFP (PX458)	BbsI	pSH1: Cas9-GFP-KA672-3
Hs	PNPLA2	sgRNA	KA673_HsPNPLA2_1_R	aaacCGTGTCAGACGGCGAGAATGc		BbsI	
Hs	PNPLA2	sgRNA	KA674_HsPNPLA2_2_F	caccgGGCTGGTGCCAAGTTCATTG	pU6-(BbsI)_CBh-Cas9-T2A-BFP	BbsI	pSH2: Cas9-BFP-KA674-5
Hs	PNPLA2	sgRNA	KA675_HsPNPLA2_2_R	aaacCAATGAACTTGGCACCAGCCc		BbsI	
Hs	MGLL	sgRNA	KA676_HsMGLL_1_F	caccgCTGGTGTTCGCCCACGACCA	pSpCas9(BB)-2A-GFP (PX458)	BbsI	pSH3: Cas9-GFP-KA676-7
Hs	MGLL	sgRNA	KA677_HsMGLL_1_R	aaacTGGTCGTGGGCGAACACCAGc		BbsI	
Hs	MGLL	sgRNA	KA678_HsMGLL_2_F	caccgTCCGAGCCAGCTCTTCATAG	pU6-(BbsI)_CBh-Cas9-T2A-BFP	BbsI	pSH4: Cas9-GFP-KA678-9
Hs	MGLL	sgRNA	KA679_HsMGLL_2_R	aaacCTATGAAGAGCTGGCTCGGAc		BbsI	
Hs	PNPLA2	sgRNA	KA672_HsPNPLA2_1_F	caccgCATTCTCGCCGTCTGACACG	Lentiguide/puro	BbsI	pSH5: LGP-PNPLA2-1
Hs	PNPLA2	sgRNA	KA673_HsPNPLA2_1_R	aaacCGTGTCAGACGGCGAGAATGc		BbsI	
Hs	PNPLA2	sgRNA	KA674_HsPNPLA2_2_F	caccgGGCTGGTGCCAAGTTCATTG	Lentiguide/puro	BbsI	pSH6: LGP-PNPLA2-2
Hs	PNPLA2	sgRNA	KA675_HsPNPLA2_2_R	aaacCAATGAACTTGGCACCAGCCc		BbsI	
Hs	MGLL	sgRNA	KA676_HsMGLL_1_F	caccgCTGGTGTTCGCCCACGACCA	Lentiguide/puro	BbsI	pSH7: LGP-MGLL-1
Hs	MGLL	sgRNA	KA677_HsMGLL_1_R	aaacTGGTCGTGGGCGAACACCAGc		BbsI	
Hs	MGLL	sgRNA	KA678_HsMGLL_2_F	caccgTCCGAGCCAGCTCTTCATAG	Lentiguide/puro	BbsI	pSH8: LGP-MGLL-2
Hs	MGLL	sgRNA	KA679_HsMGLL_2_R	aaacCTATGAAGAGCTGGCTCGGAc		BbsI	

4 Results

A part of the results in this section has been published in Honeder *et al.* (1).

4.1 ATGL-KO in a human NSCLC cell line (A549) causes metabolic alterations and size discrepancy when grown as spheroids

Previous investigations by our group indicated that the loss of ATGL in A549 lung cancer cells grown in a monolayer results in a more aggressive cancer phenotype (154). However, cancer cells *in-vivo* do not grow as a monolayer and are usually part of more complex spatial structures. 3D cell culture can be employed as an alternative *in-vitro* model that mimics some physiological conditions, like hypoxia or nutrient gradients, found in solid tumors (178). Despite our previous findings, the question remained how ATGL loss affects cancer cells in a more *in-vivo*-like environment. To this end, we used the same genetically modified A549 clonal cell lines either expressing ATGL (Control) or not (ATGL-KO) (Figure 7) and grew them as multicellular tumor spheroids in ultra-low attachment plates.

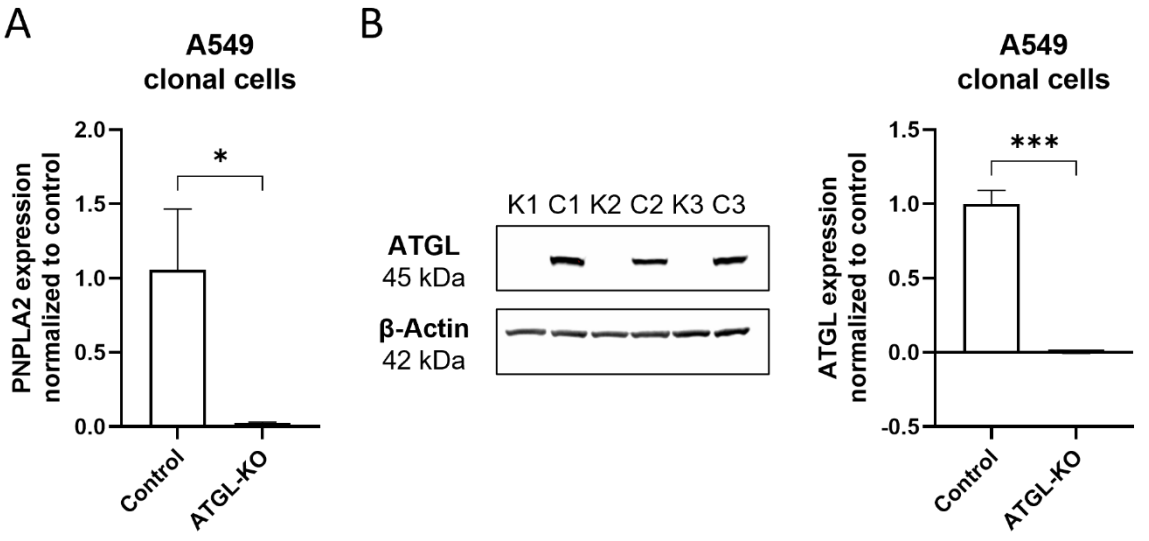

Figure 7: validation of ATGL loss in A549 ATGL-KO clonal cell lines. A: qPCR of *PNPLA2*, gene expression normalized to two housekeeping genes (*EEF1A1* and *ACTB*) and to controls (n = 3). B: Western Blot of ATGL, protein expression normalized to β-Actin expression and to controls (n = 3); K1-3: ATGL-KO clones; C1-3: Control clones. (* p-value < 0.05, ** p-value < 0.01, *** p-value < 0.001)

We monitored spheroid growth by capturing images of the cells over the period of 10 days, with representative spheroid images from day 10 depicted in Figure 8A. Strikingly, the spheroids lacking ATGL exhibited a significant increase in size compared to Control spheroids after 10 days of growth (Figure 8A and 8B).

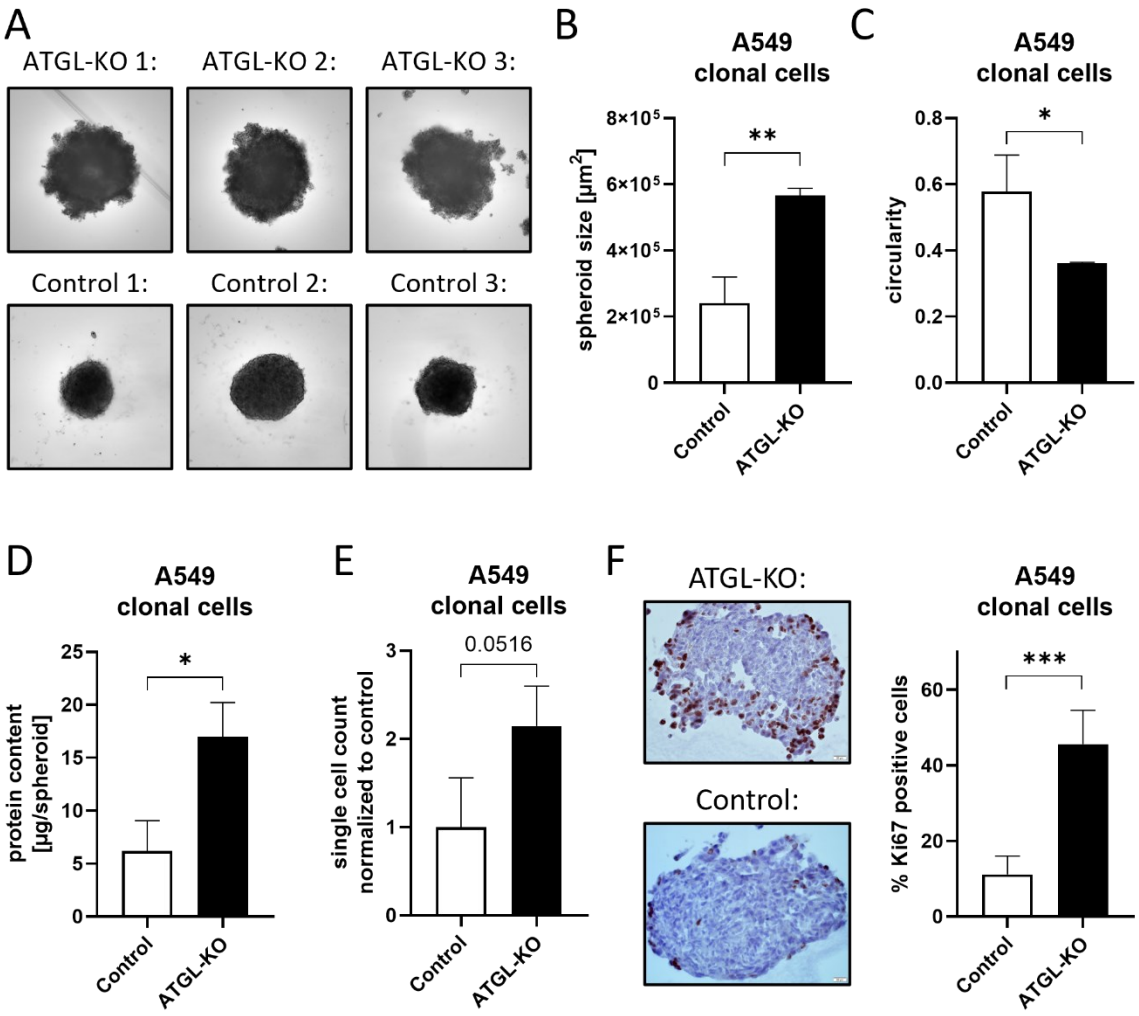

Figure 8: A549 ATGL-KO and Control show growth and morphology differences. A: representative images of ATGL-KO (upper panel) and Control (lower panel) spheroids after 10 days in culture; B: spheroid cross-sectional area quantitation, representing spheroid size; C: spheroid circularity; D: spheroid protein content; E: single cell count per spheroid normalized to control; F: Ki67 histology staining and quantitation of Ki67 positive cells. (n = 3 biological replicates and n = 4 spheroids per replicate; * p-value < 0.05, ** p-value < 0.01, *** p-value < 0.001) Figure adapted from Honeder *et al.* (1) with permission from the publisher (CC BY 4.0 License)

In addition to the size difference, the morphology of the ATGL-KO spheroids diverged from that of the Control spheroids. The former displayed less circular growth, while the latter displayed a smoother and more uniform surface, which is reflected in a lower circularity score in ATGL-KO spheroids (Figure 8C). To validate that ATGL-KO spheroids are not only larger in size but also contain more cells, the protein content within the spheroids was assessed and revealed a significantly greater protein content in the ATGL-KO spheroids (Figure 8D), which indicates an elevated cell count and, consequently, increased growth. This observation was further corroborated through single cell counts using flow cytometry (Figure 8E). Additionally, increased percentage of proliferation positive marker Ki67-positive cells were found in ATGL-KO spheroids compared to Control spheroids (Figure 8F). We further checked the viability of cells derived from ATGL-KO and Control spheroids and found that there was no difference in the percentage of dead cells due to very low numbers of dead cells overall (Figure 9).

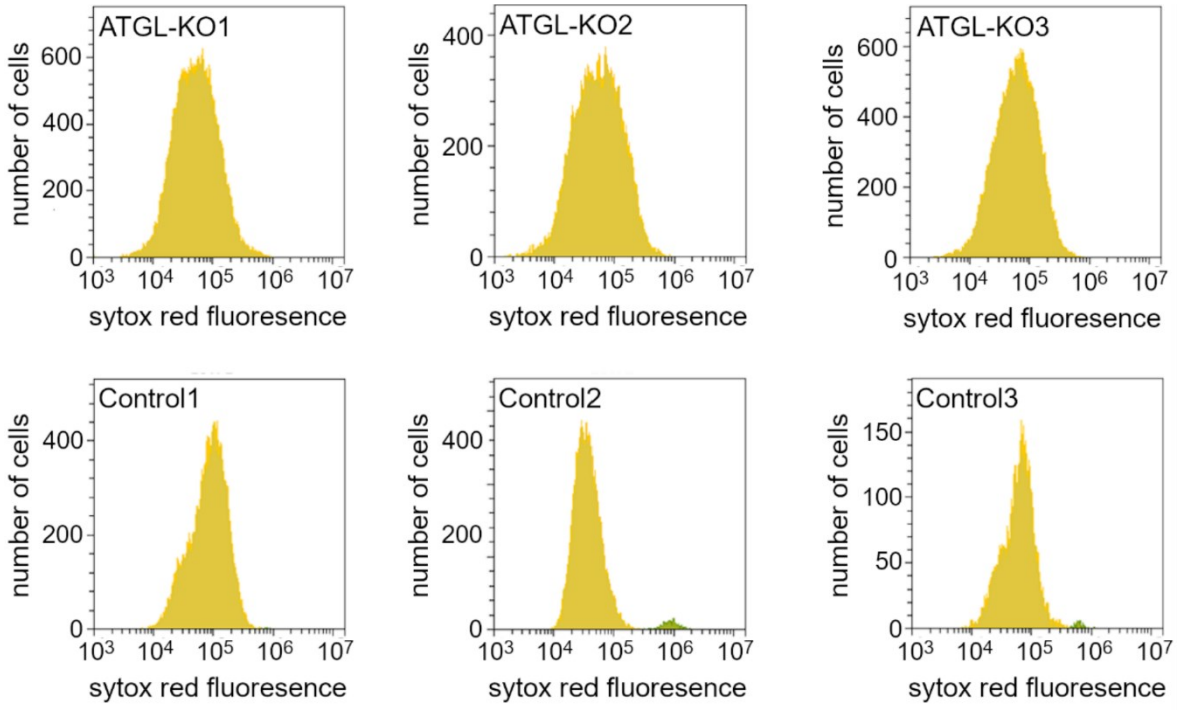

Figure 9: low number of dead cells in ATGL-KO and Control spheroids. SYTOX™ Red staining of cells derived from spheroids cultured for 10 days: no significant shift of the single cell population (yellow) towards higher Sytox Red fluorescence in any of the clonal cell lines; ATGL-KO as well as Control spheroids show a max. of 3.5 % dead cells in the single cell

population. Figure adapted from Honeder *et al.* (1) with permission from the publisher (CC BY 4.0 License)

In an effort to uncover potential proteomic alterations linked to the observed difference in spheroid growth, we performed an in-depth analysis of the proteome of ATGL-KO as well as Control A549 spheroids by LC-MS/MS-based label-free quantitative (LFQ) proteomics. This analysis revealed differences in the abundance of several proteins between the two groups (ATGL-KO and control) (Figure 10A).

Notably, some of the proteins upregulated in ATGL-KO compared to Control spheroids are representative of a glycolytic phenotype. The high-affinity glucose transporter GLUT1 (*SLC2A1*) was among the upregulated proteins. Both GLUT1 and GLUT3 are targeted by HIF-1 and their upregulation is associated with cancer (31). We also confirmed that both GLUT1 and GLUT3 expression was increased in ATGL-KO spheroids (Figures 10B and 10C). Furthermore, proteomics data suggest a glycolytic shift in ATGL-KO spheroids through increased abundance of the ADP-dependent Glucokinase (ADPGK), as well as PFKP, one of the key regulatory enzymes of glycolysis (37). Besides changes in glycolytic enzymes, we also observed some proteins that were upregulated in ATGL-KO spheroids that point towards increased cell division and DNA synthesis. These include proteins of the minichromosome maintenance protein complex (MCM3, MCM5) and thymidylate kinase (DTYMK), which play a role in DNA replication (179) and synthesis (180), respectively. The amino acid transporter LAT1 (*SLC7A5*), which facilitates the transport of large neutral amino acids like tyrosine, leucine, isoleucine, valine and phenylalanine (181), was also up in ATGL-KO spheroids. This might hint towards increased protein production in addition to increased division, and indeed we observed increased protein content (Figure 8D) in ATGL-KO spheroids as well as increased cell number (Figure 8E).

Furthermore, changes in lipid metabolism proteins were evident from the proteomics data. The alternative FA desaturase, fatty acid desaturase 2 (*FADS2*) was higher abundant in ATGL-KO spheroids. FADS2 plays a crucial role as a salvage pathway for FA desaturation, especially in the event of SCD1 inhibition, which is common in hypoxic conditions (182). Immunoblotting confirmed heightened levels of FADS2, while SCD1 levels were unchanged in ATGL-KO spheroids (Figure 10B and 10C). However, the activity of SCD1

might be different due to different extent of hypoxia. Another protein upregulated in ATGL-KO spheroids is Syntenin-1 (*SDCBP)* which is associated with cancer invasiveness and has been shown to enhance cancer migration (183). The morphological differences that were observed between ATGL-KO and Control spheroids (Figure 8A, 8B and 8C) might be due to increased migratory potential of ATGL-KO cells, which was previously published by our group (154).

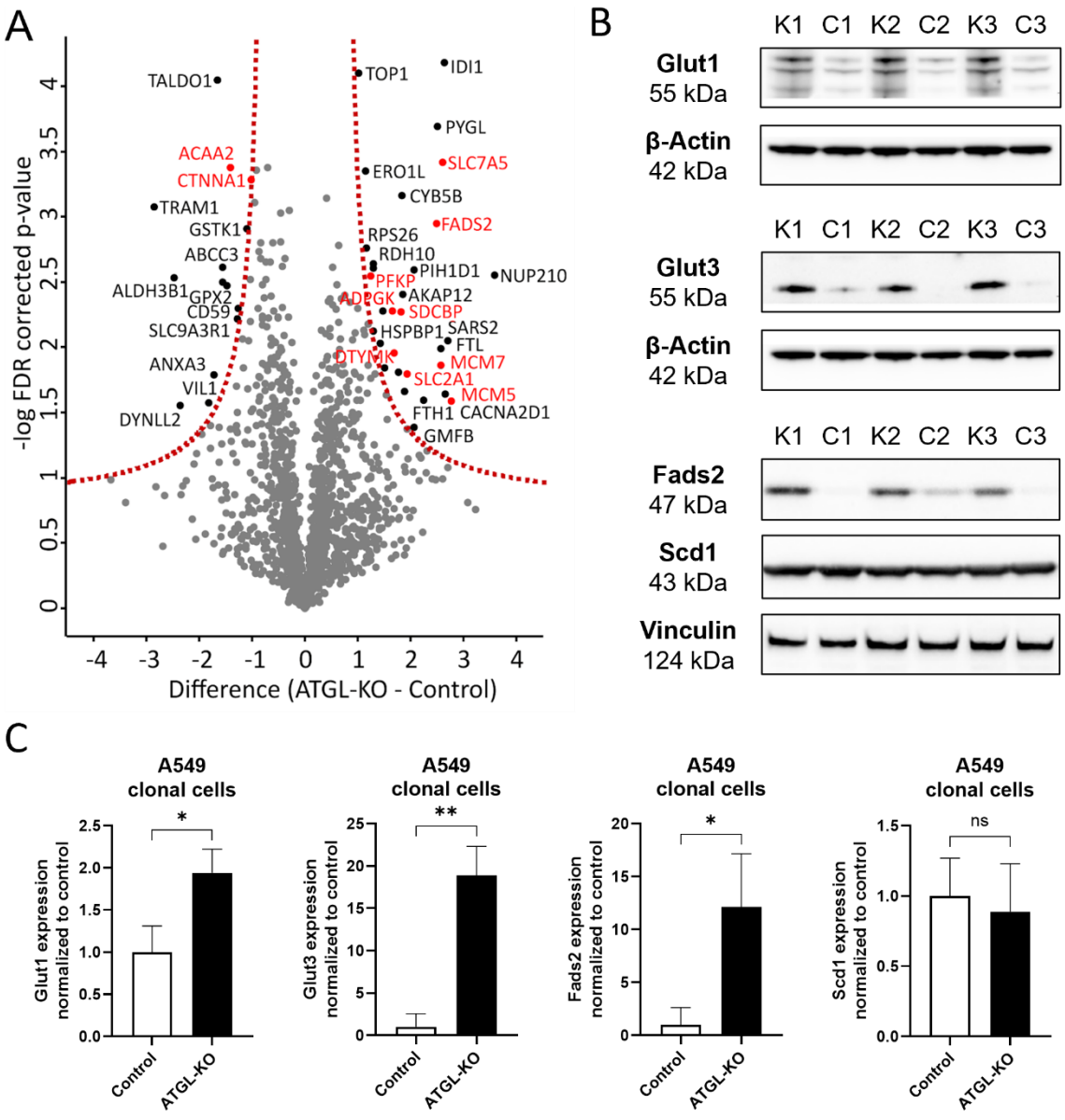

Figure 10: label-free quantitation (LFQ) proteomics of ATGL-KO and Control spheroids reveals changes in metabolism proteins. A: volcano plot of LFQ proteomics data from ATGL-KO and Control spheroids (FDR: 0.05 %, s0: 0.5, 250 randomizations), proteins marked in

red are discussed in more detail; B: Western Blot of Glut1, Glut3, Fads2 and Scd1; C: Protein expression normalized to β-Actin (Glut1/3) or Vinculin (Fads2, Scd1) expression and to controls (n = 3, * p-value < 0.05, ** p-value < 0.01, *** p-value < 0.001); figure adapted from Honeder *et al.* (1) with permission from the publisher (CC BY 4.0 License)

In the group of proteins that were lower in ATGL-KO spheroids, α-catenin (*CTNNA1*) was identified, which is a well-known tumor suppressor that is often downregulated in various human cancers (184). α-catenin plays a pivotal role within the E-cadherin-catenin complex, a critical component for cell-cell adhesion and tissue organization (184). The reduced presence of α-catenin in ATGL-KO spheroids could potentially contribute to the observed alterations in spheroid morphology, characterized by diminished circularity and a rougher, more irregular outer surface when compared to control spheroids (Figure 8A and 8C). Moreover, we identified 3-Ketoacyl-CoA Thiolase (*ACAA2*) to be lower in ATGL-KO spheroids. This enzyme is involved in mitochondrial beta-oxidation, an aerobic process responsible for generating energy from fatty acids (185). This finding suggests a preference for glycolytic energy production over fatty acid oxidative pathways in ATGL-KO spheroids.

4.2 Increased glucose uptake in ATGL-KO spheroids but not ATGL-KO cells in 2D cell culture

The proteomics data hinted at increased glucose uptake in ATGL-KO spheroids through increased levels of GLUT1 (Figure 10A). Because both GLUT1 and GLUT3 are HIF-1 targets and are often upregulated in cancers (31), we checked the expression of these glucose transporters by western blot and found that both GLUTs exhibited significantly higher levels in ATGL-KO compared to control cells (Figure 10B and 10C). We also examined GLUT1 and GLUT3 expression in ATGL-KO and Control cells grown in 2D culture and found that GLUT1 is unchanged while GLUT3 is higher in ATGL-KO cells (Figure 11D and 11E), albeit to a lesser extent than in 3D cell culture.

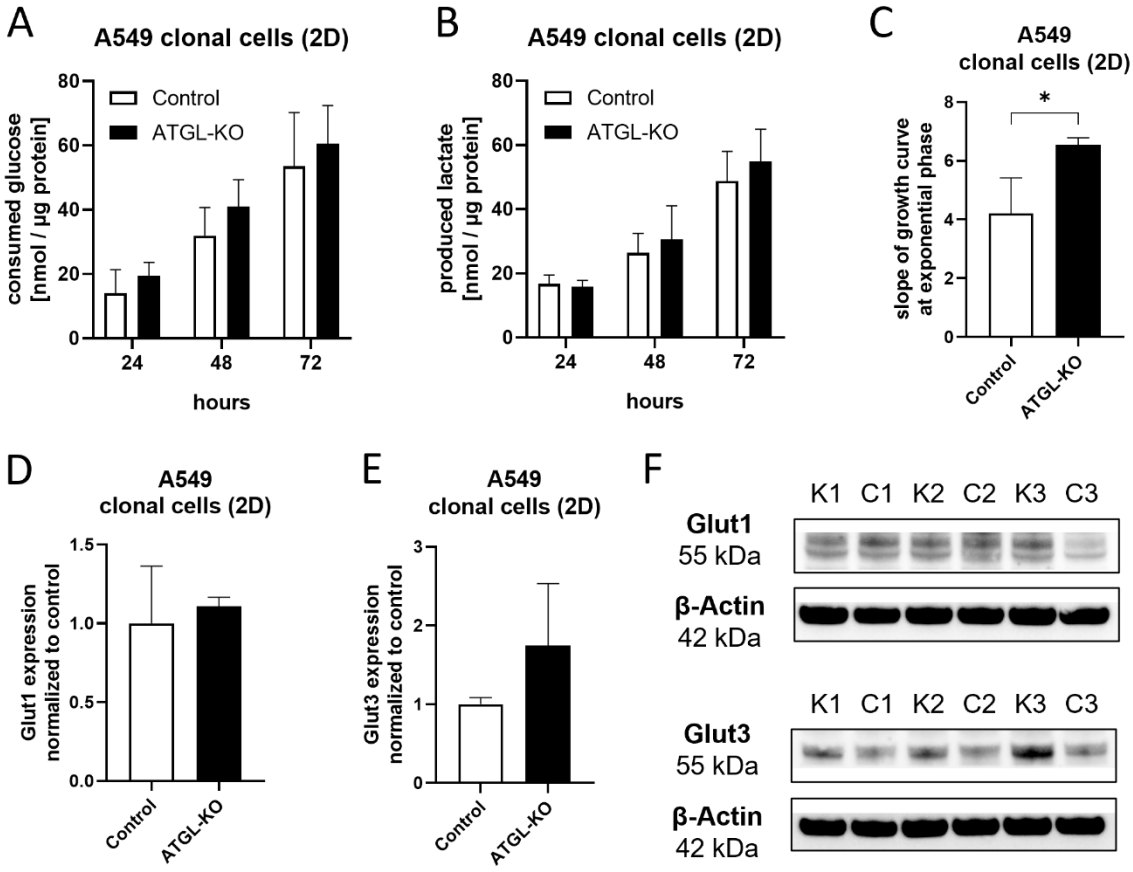

Figure 11: slightly increased proliferation but no change in nutrient consumption and production in A549 ATGL-KO and Control cells grown in monolayer culture. A: consumed glucose over the course of 72 hours in nmol per µg protein; B consumed lactate over the course of 72 hours in nmol per µg of protein; C: cell growth was estimated as a function of confluency over time and the slope of the linear growth rate (between t = 0 (24h after plating) and t = 30) is shown; D: Western Blot of Glut1 and Glut3; E: Protein (Glut1/3) expression normalized to β-Actin and to controls (n = 3, * p-value < 0.05, ** p-value < 0.01, *** p-value < 0.001); figure adapted from Honeder *et al.* (1) with permission from the publisher (CC BY 4.0 License)

To functionally validate the increased glucose uptake and a concomitant shift towards a more glycolytic phenotype, we performed in vitro assays measuring glucose consumption and lactate production in spheroid (3D) and 2D culture. As anticipated, ATGL-KO spheroids rapidly consumed glucose from the media and simultaneously produced higher amounts of lactate compared to control cells (Figure 12A and 12C). When normalized to protein content per spheroid, lactate production remained significantly higher in ATGL-

KO spheroids (Figure 12D), while normalized glucose consumption was not significantly different between ATGL-KO and Control spheroids (Figure 12B).

Spheroids usually feature a highly proliferative outer rim that causes rapid growth, while cells in the core show a quiescent or necrotic phenotype. We ruled out high numbers of necrotic cells in the core of the spheroids by dead-cell staining, which revealed very low numbers of dead cells in all tested spheroids (Figure 9). However, we observed that in ATGL-KO as well as Control spheroids the highly proliferative cells (Ki67 positive) were primarily found in the outer rim (Figure 8F). Therefore, despite increased expression of glucose transporters, the cells within the core of the spheroids might not be capable to take up more glucose owed to lack of vascularization. When we examined ATGL-KO and Control cells grown in 2D cell culture, despite increased proliferation (Figure 11C), the ATGL-KO cell lines showed only minor, non-significant, increase in glucose consumption and lactate production (Figure 11A and 11B), suggesting that the observed shift towards a more glycolytic phenotype is a distinctive characteristic of ATGL-KO spheroids.

Since glutamine is an essential nutrient for some cancers, and it makes up one of the major carbon sources for cells besides glucose (72), we assessed glutamine consumption in ATGL-KO and Control spheroids. While the total consumption of glutamine was higher for ATGL-KO spheroids, the overall consumption rate was not significantly different from that of the controls (Figure 12E). When normalized to protein content, glutamine uptake was significantly higher in Control cells compared to ATGL-KO cells (Figure 12F). These findings suggest that ATGL-KO cells primarily thrive on glucose, while the control cells are more dependent on glutamine.

Due to the observed changes in proteins involved in lipid metabolism (Figure 10A), and ATGL being the rate limiting enzyme for breakdown of TGs, we conducted LD and FA analysis to support the observed proteomic changes. Like previously observed in A549 ATGL-KO and Control cells grown in 2D (154), the LD volume was increased significantly in spheroid-derived ATGL-KO cells compared to spheroid-derived Control cells (Figure 11G). Furthermore, we detected an increased ratio of monounsaturated fatty acids (MUFA) to saturated fatty acids (SFA), as well as higher levels of C16:1 fatty acid (Figure 11H and 11I) in ATGL-KO spheroids. These findings are consistent with the increased abundance of

FADS2, which catalyzes the conversion of saturated fatty acids, particularly C16:0 FA, into the C16:1 FA sapienic acid (182).

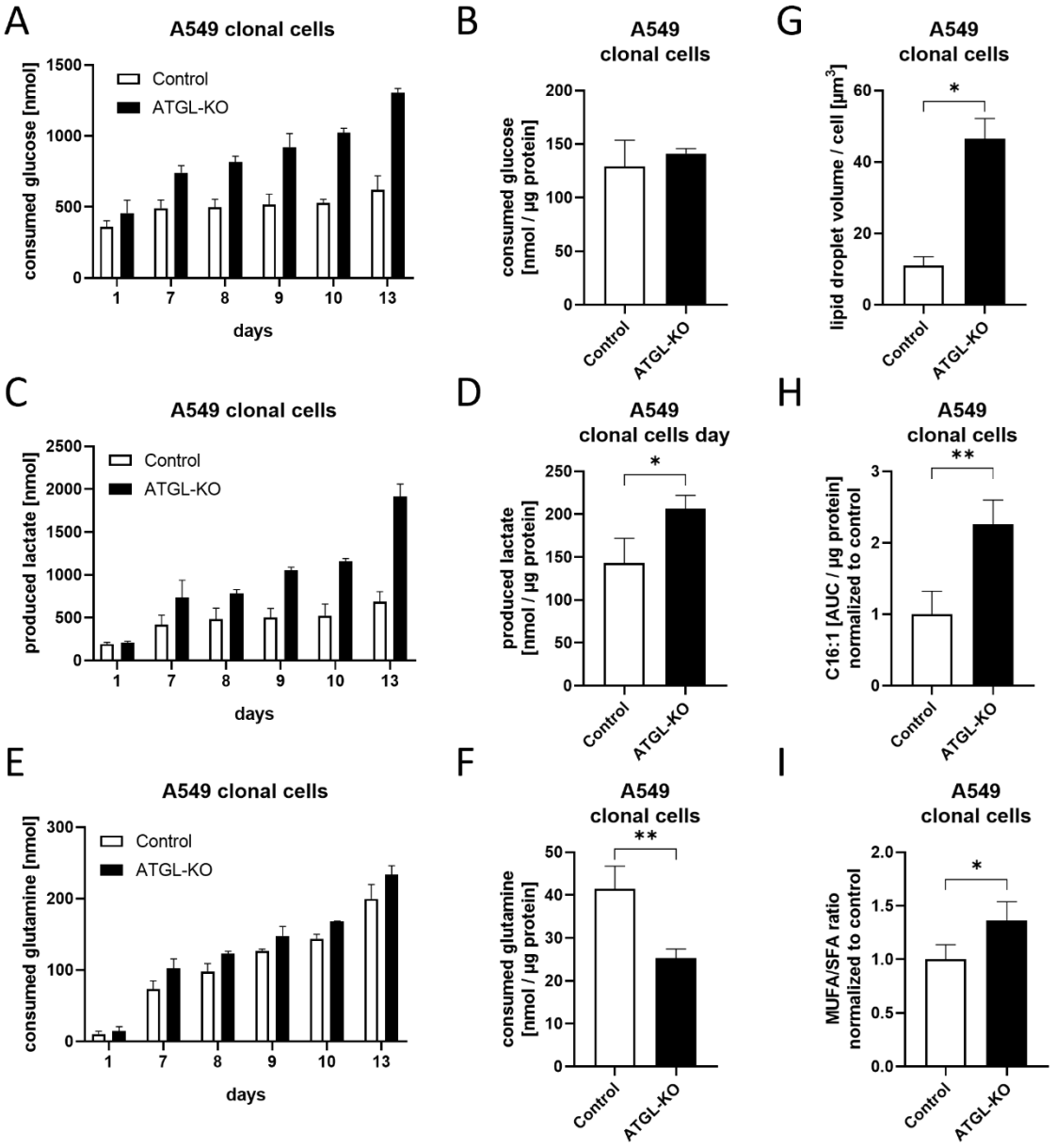

Figure 11: changes in metabolite uptake and production between ATGL-KO and Control spheroids. A: consumed glucose over 13 days in nmol per spheroid; B: consumed glucose on day 13 normalized to protein; C: produced lactate over 13 days in nmol per spheroid; D: produced lactate on day 13 normalized to protein; E: consumed glutamine over 13 days in nmol per spheroid; F: consumed glutamine on day 13 normalized to protein; G: lipid droplet volume of cells derived from spheroids; H: C16:1 concentration normalized to protein and

control; I: MUFA/SFA ratio normalized to control (n = 3, * p-value < 0.05, ** p-value < 0.01, *** p-value < 0.001). Figure adapted from Honeder *et al.* (1) with permission from the publisher (CC BY 4.0 License)

4.3 Increased Size and Proteome Changes between ATGL-KO and Control Spheroid-Derived Tumors Cultivated on Chorioallantoic Membranes

To create an even more physiologically relevant environment for the spheroids and mitigate potential limitations due to the absence of a tumor microenvironment, we conducted the chick chorioallantoic membrane (CAM) assay. The CAM assay is a well-established technique used in a wide range of cancer investigations, spanning from angiogenesis to invasion and metastasis (169). In this context, we cultivated spheroids from both ATGL-KO and Control A549 cells over a 10-day period. Subsequently, we transplanted these spheroids onto the CAM surface, allowing them to develop for an additional 5 days before harvesting. The tumors derived from these spheroids were subjected to LC-MS/MS proteomics analysis. Strikingly, ATGL-KO spheroid-derived tumors were significantly larger than Control spheroid-derived tumors (Figure 13B). The spheroid-derived tumors also showed substantial variations in their proteome, with ATGL-KO spheroid-derived tumors exhibiting a notably higher number of upregulated proteins in comparison to the Control group (Figure 13A). Upregulated proteins in ATGL-KO spheroid-derived tumors, displaying a fold change greater than two, were subjected to pathway analysis using the String functional protein database[20]. This analysis revealed upregulation of proteins involved in glucose metabolism, glycolysis, and protein translation in ATGL-KO spheroid-derived tumors (Figure 13C).

Several glycolytic proteins were found to be higher in ATGL-KO spheroid-derived tumors: *PFKP*, *ALDOA*, *PGK1*, *PGAM1*, *ENO1*, and *PKM*, suggesting overall higher glycolytic flux in those tumors. Additionally, tricarboxylic acid (TCA) cycle proteins like aconitate hydratase (*ACO2*), and isocitrate dehydrogenase 1 (*IDH1*), as well as ATP synthase subunit g (*ATP5L*), an enzyme involved in the electron transport chain were in the list of proteins

[20] https://www.string-db.org/

increased in ATGL-KO spheroid-derived tumors. These findings collectively suggest enhanced glucose metabolism.

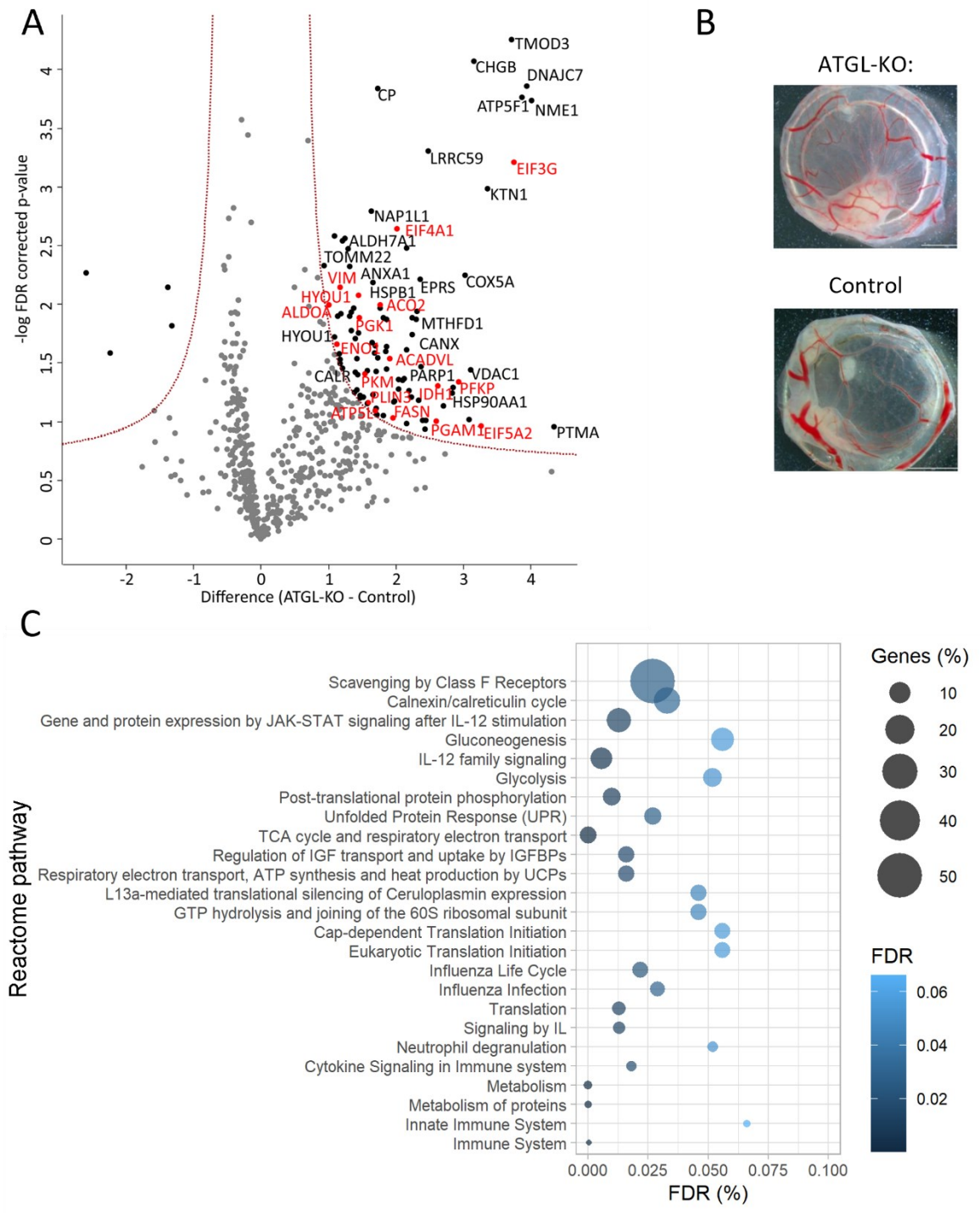

Figure 13: ATGL-KO spheroids grown on CAM form larger tumors and display changes in the proteome. A: volcano plot of LFQ proteomics data from ATGL-KO and Control spheroids (FDR: 0.05 %, s0: 0.5, 250 randomizations), proteins marked in red are discussed in more

detail; B: representative image of tumors derived from ATGL-KO (upper panel) or Control (lower panel) spheroids on CAM; B: Highly enriched Reactome pathways in ATGL-KO spheroids grown on CAM (proteins upregulated at least 2-fold were included in the analysis, top 25 most enriched pathways are shown). Figure adapted from Honeder *et al.* (1) with permission from the publisher (CC BY 4.0 License)

Furthermore, numerous proteins associated with lipid metabolism exhibited higher abundance in ATGL-KO spheroids. These include fatty acid synthase (*FASN*), very-long-chain specific acyl-CoA dehydrogenase (*ACADVL*), and Perilipin-3 (*PLIN3*). Proteins linked to protein synthesis were also elevated: eukaryotic translation initiation factor 3 subunit G, (*EIF3G*), 5A-2 (*EIF5A2*), and 4A-1 (*EIF4A1*). These protein changes collectively indicate an increased production of biomass and heightened *de-novo* fatty acid synthesis, further supporting the presence of a more aggressive cancer phenotype.

4.4 Deletion of ATGL or MGL in a panel of NSCLC causes changes in proliferation

Given the striking phenotypic changes in A549 lung cancer cells upon ATGL-KO, we intended to generate additional lipolysis-deficient cell lines to delineate whether this is indeed a result of aberrant lipolysis in lung cancer. To this end, we employed new CRISPR-Cas9 methods, which are more thoroughly explained in the material and methods, without relying on proprietary plasmids with unknown sequence. To achieve lipolysis-deficiency, we aimed to manipulate one of two enzymes involved in neutral lipolysis: adipose triglyceride lipase (ATGL) or monoglyceride lipase (MGL). The parental cell lines were selected based on their histological subtype and genetic background and include the following: A549, NCI-H1299, NCI-H358, and NCI-H441. The characteristics of the parental cell lines and the generated KOs are summarized in Table 2. Two CRISPR-Cas9 approaches were used. Approach 1, in which sgRNA and fluorophore-containing plasmids were introduced transiently into the target cells by lipofectamine, followed by selection of double positive cells (high GFP and BFP signal) through flow cytometry, caused little or no reduction of

expression of the targets (ATGL, MGL) in the polyclonal population (here termed GFP/BFP cell lines) of both tested cell lines, A549 (Figure 14A, 14G) and H1299 (Figure 14B, 14H).

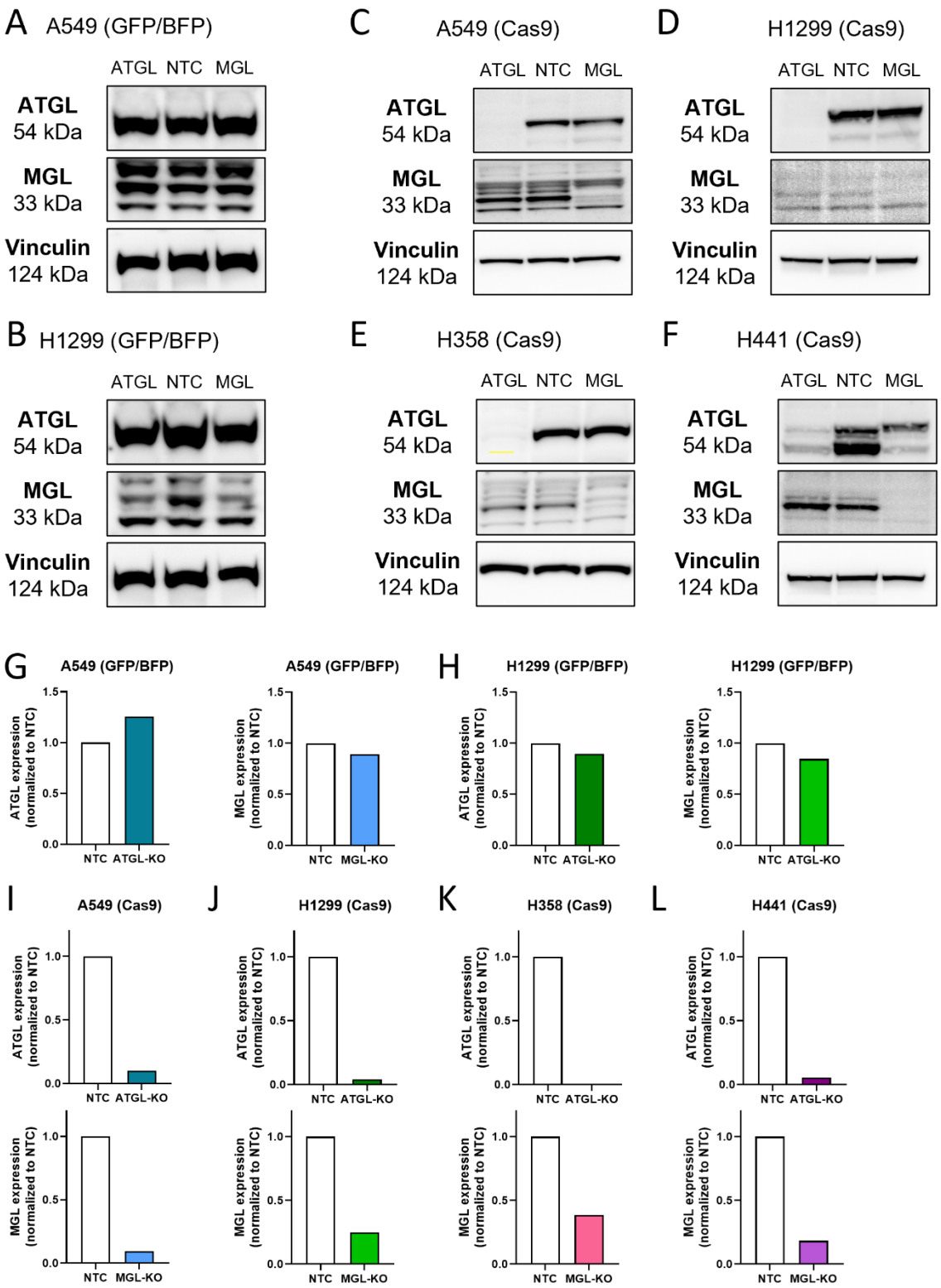

Figure 14: validation of lipase KO in A549, H1299, H358 and H441 polyclonal cell lines. A-F: Western Blots of ATGL and MGL and G-L: quantified protein expression of ATGL and MGL normalized to Vinculin and to NTC in (A/G) A549 (GFP/BFP) polyclonal cells; (B/H): H1299 (GFP/BFP) polyclonal cells; (C/I) A549 (Cas9) polyclonal cells; (D/J) H1299 (Cas9) polyclonal cells; (E/K) H358 (Cas9) polyclonal cells; (F/L) H441 (Cas9) polyclonal cells

In approach 2, Cas9 was first stably introduced into the parental cell lines, followed by introduction of sgRNAs targeting ATGL or MGL. The resulting polyclonal populations were subjected to KO validation by western blot. In all four tested cell lines, ATGL expression was abolished in ATGL-KO and MGL was abolished in MGL-KO polyclonal cell lines (Figure 14 C-F and 14I-L). The cell lines generated with this, second, CRISPR-Cas9 approach (here termed Cas9 polyclonal cell lines) were used for further experiments.

Deletion of ATGL, the main enzyme degrading triglycerides intracellularly, is expected to cause significant accumulation of LDs. Therefore, we next sought to determine whether ATGL deletion indeed renders the cell lines lipolysis-deficient and causes accumulation of LDs. LD staining and analysis using flow cytometry was therefore employed to functionally validate ATGL-KO in the cell lines. We first tested the ability of LD depletion and induction in the parental cell lines by this method. Parental cell lines were either treated with 5 µM DGAT1 inhibitor and 5 µM DGAT2 inhibitor for 24 hours (DGATi), or with 30 µM oleic acid-BSA conjugate (Oleic Acid), to prevent LD formation or induce accumulation of LDs, respectively. As a control, cells were treated with vehicle (DMSO). After 24 hours, the LDs were quantified by flow cytometry by their bodipy intensity. The different cell lines showed different basal lipid droplet levels, and treatment with oleic acid was able to induce LD accumulation in all parental cell lines, indicating that none of the cell lines had already reached its maximum capacity to store LDs at basal conditions (Figure 15A). Inhibition of LD formation by DGAT inhibitors, on the other handy, was able to reduce LD signal in all the cell lines, with exception of A549 cells, in which the DGAT inhibition caused very little reduction in median bodipy intensity. In Figures 15B-E, the median bodipy intensity and thus LD content in control (NTC) and ATGL deficient (ATGL) Cas9 expressing polyclonal cell lines is represented. In all four tested cell lines, the deletion of ATGL resulted in increased bodipy signal. These findings further corroborate a successful ATGL deletion

and deficiency in breaking down intracellular lipid droplets. The biggest LD accumulation upon ATGL-KO was observed in H441 cells (64 %, Fig. 15E), followed by A549 (40 % increase, Fig. 15B) and H1299 (28 %, Fig. 54C), while there was only a small increase in H358 cells (8 %, Fig. 15D).

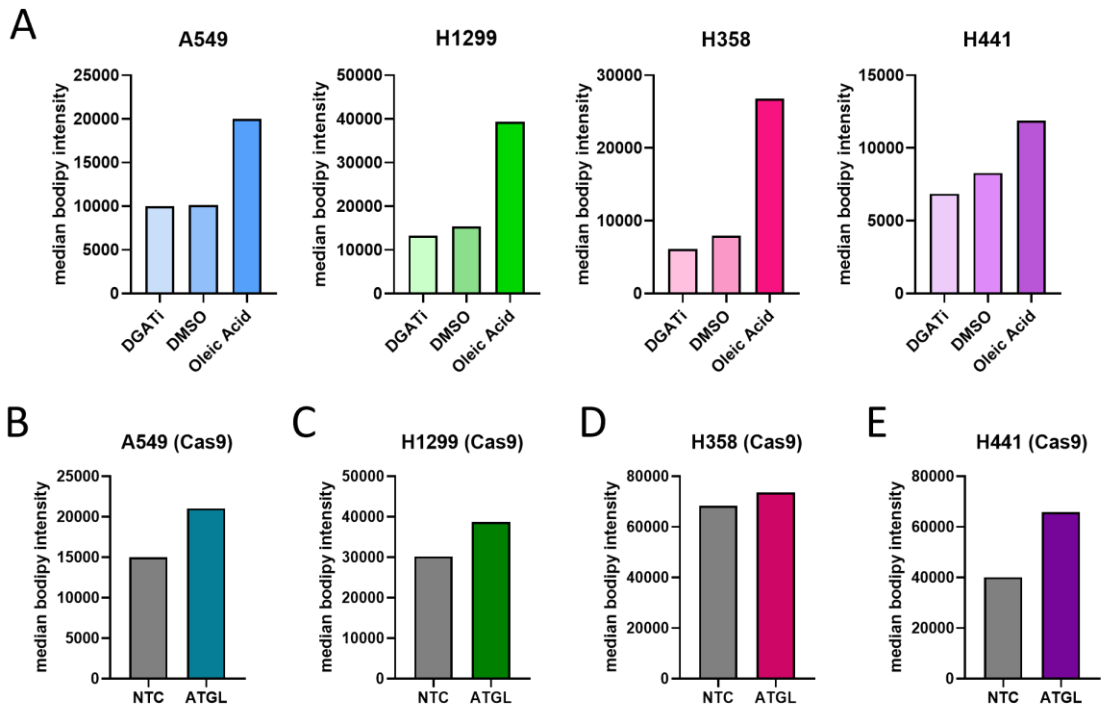

Figure 15: ATGL-KO in Cas9 expressing polyclonal NSCLC cell lines causes increase in lipid droplets. A: parental cell lines treated with 5 µM DGAT1 inhibitor (PF-04620110) and 5 µM DGAT2 inhibitor (PF-06424439) to reduce lipid droplets or with 30 µM oleic acid-BSA conjugate to induce lipid droplets or DMSO as control; B-E: Cas9 expressing controls (NTC) and ATGL-KO (ATGL) polyclonal cell lines. LD quantity assessed through staining with bodipy and measurement of the mean fluorescence intensity of cells by flow cytometry

Since we previously observed proliferation increase in A549 cells upon deletion of ATGL, the proliferation of control (NTC) and KO cell lines was assessed. Polyclonal A549 (Cas9) ATGL-KO cells showed a substantial increase in proliferation compared to control (NTC) cells, in 2D cell culture (Figure 16A). Strikingly, the knockout of MGL in the same cell line (A549 Cas9) increased proliferation to a similar extent than ATGL-KO compared to Controls (Figure 16A). A similar phenotype was observed in a second cell line: H1299, where substantial increase in proliferation was observed upon ATGL-KO as well as MGL-KO (Figure

16B). H358 cells, on the other hand, proved to display a different phenotype upon lipolysis deficiency. Compared to Control (NTC) cells, both ATGL-KO and MGL-KO had lower number of doublings/day (Figure 16C), albeit this difference was not as pronounced as the increased proliferation in A549 and H1299 cells (Figures 16A and 16B). In the generally more slowly proliferating H441 cells, the deletion of ATGL but not MGL increased proliferation slightly, but not significantly (Figure 16D).

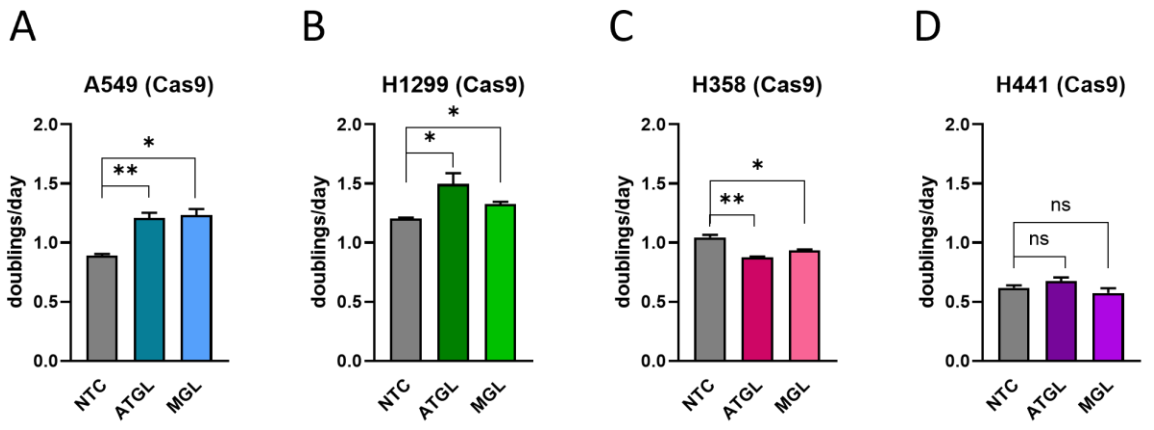

Figure 16: lipolysis-deficient cell lines display different proliferation rates compared to Control cells. A-D: cell doublings/day of control (NTC), ATGL-KO (ATGL) and MGL-KO (MGL) Cas9 expressing polyclonal cell lines grown in 2D: A: A549 (Cas9); B: H1299 (Cas9); C: H358 (Cas9); D: H441 (Cas9) (n = 3, * p-value < 0.05, ** p-value < 0.01, *** p-value < 0.001)

Amongst the NSCLC cell line panel, A549 and H1299 cells were the cell lines that displayed higher proliferation rates overall compared to the other two cell lines, H358 and H441. Therefore, the generation of ATGL-KO and MGL-KO was attempted and achieved first in A549 and H1299 background. For these two cell lines, we also tested the growth behavior in 3D cell culture. All cell lines generated in A549 (Cas9) and H1299 (Cas9) background formed spheroids well in Ultralow-Attachment plates without any supporting matrix. Representative images of spheroids after 11 days in culture are shown in Figure 17A (A549) and 17D (H1299). Interestingly, we did not observe the striking morphological difference that was previously observed in the A549 ATGL-KO clonal cell lines. However, ATGL-KO in both Cas9-expressing polyclonal cell lines (A549 and H1299) showed increased proliferation rates compared to Controls (Figure 17B and 17E). In A549, proliferation was even higher upon MGL-KO (Figure 17B), while MGL-KO in H1299 cells showed less pronounced

proliferation increase (Figure 17E). Overall, the cell lines follow the trend that was observed in the previously generated and thoroughly tested A549 ATGL-KO clonal cell lines.

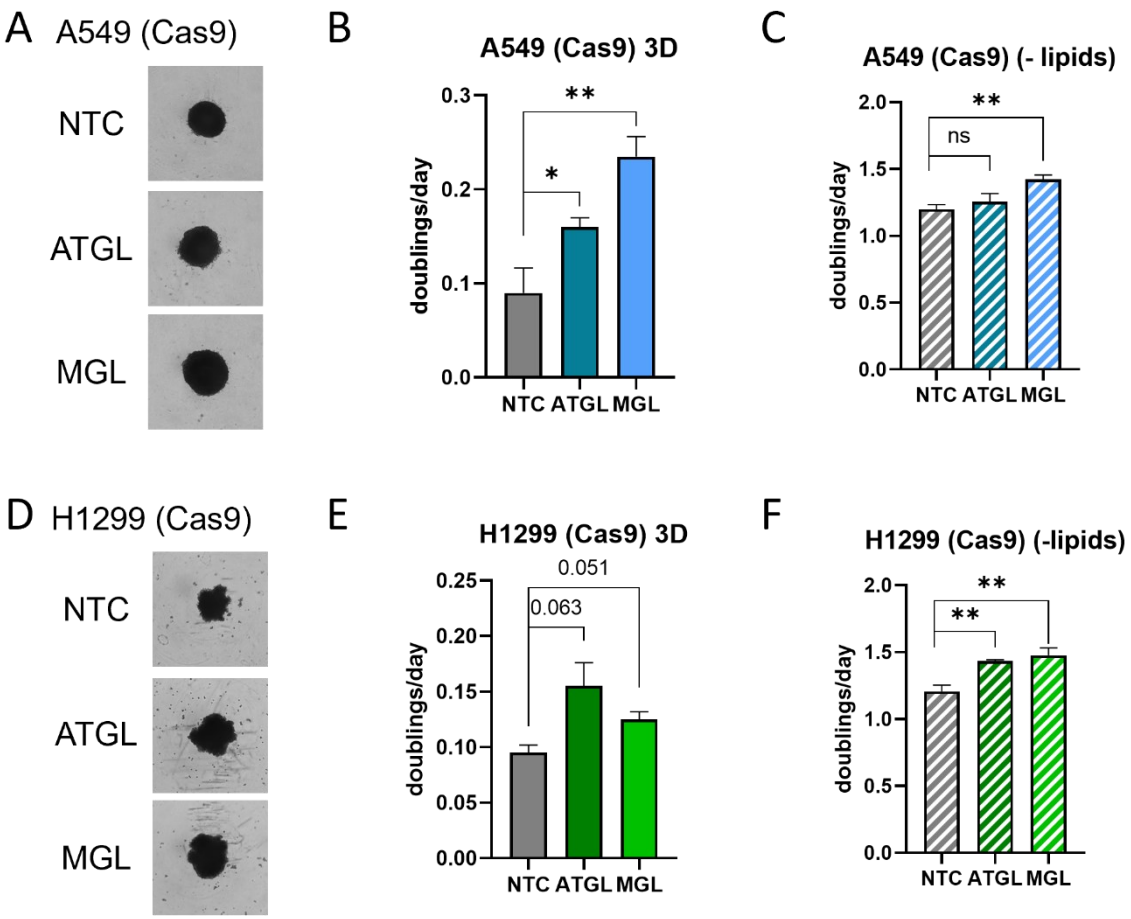

Figure 17: lipolysis-deficient cell lines with growth advantage in 2D cell culture also show increased proliferation in 3D cell culture and in lipid-depleted medium. A549 (Cas9) (upper panel) and H1299 (Cas9) (lower panel) Control (NTC), ATGL-KO (ATGL), and MGL-KO (MGL) polyclonal cell lines were grown as spheroids for 11 days. A and D: representative spheroid images after 11 days in culture; B and E: doublings/day calculated from cell counts over a period of 11 days; C and F: doublings/day of ATGL-KO (ATGL), MGL-KO (MGL) and Control (NTC) cell lines grown in regular or lipid-depleted (- lipids) medium (n = 3). (* p-value < 0.05, ** p-value < 0.01, *** p-value < 0.001)

With the deletion of ATGL or MGL, the mobilization of FAs from TG stores within the cells is disturbed. We hypothesize that cells are more dependent on *de-novo* FA synthesis or on supply of exogenous fatty acids under these circumstances. Thus, we aimed to test

the effect of growing A549 (Cas9) and H1299 (Cas9) polyclonal cell lines in medium stripped of lipids, i.e., lipid-depleted medium (- lipids). In H1299 (Cas9) cell lines, ATGL-KO or MGL-KO did not appear to result in increased dependency on exogenous fatty acids, and proliferation rates were still higher than that of Control cells (Figure 17F); and this was also observed in A549 (Cas9) MGL-KO cells (Figure 17C). In A549 (Cas9) ATGL-KO cells, the increase in proliferation that was observed in regular medium (Figure 16A) was lower in lipid-depleted conditions (Figure 17C). Nevertheless, we observed that all the cell lines tested grew well in lipid-depleted conditions overall without severe proliferation deficiency (Figure 17C and 17F). We hypothesize that upon ATGL or MGL deletion, the cells grown in lipid depleted medium rely on and switch to *de-novo* fatty acid synthesis to a higher extent than Control cells, which also possess the ability to mobilize FAs from TG stores. To test this hypothesis, we performed metabolic tracing of A549 (Cas9) polyclonal cell lines with ATGL-KO or MGL-KO or Controls (NTC) to assess the rate of fatty acid synthesis from glucose.

4.5 Metabolic tracing of uniformly ^{13}C-glucose into fatty acids reveals increased fatty acid synthesis in lipolysis-deficient cell lines

To test our hypothesis, that cells with ATGL deletion or MGL deletion that are grown in lipid depleted medium are more dependent on *de-novo* fatty acid synthesis, we performed a metabolic tracing experiment. In this experiment, the cells were grown for 72 hours in medium containing lipids (+ lipids) or not (- lipids), and uniformly labelled ^{13}C-glucose was used as the sole glucose source. After 72 hours, the cells were counted, and fatty acid methyl ester (FAME) extraction was performed. The first fatty acid generated by *de-novo* fatty acid synthesis is the saturated fatty acid palmitate (C16:0) (77). We here show palmitate labelling as a representation of *de-novo* synthesized fatty acids in general (Figure 18), however, the labelling of other fatty acids can be found in the Appendix (Figures 29-34 for myristate, palmitoleate, stearate, oleate, arachidate and arachidonate, respectively). Figure 18 shows fraction distributions of labelled palmitate, including unlabelled palmitate of cells grown in lipid-containing (Figure 18A) or lipid-depleted (Figure 18C) medium. Fractions of palmitate are denoted as m+n, where n is the number of carbon atoms derived

from labelled glucose. Fractions with increasing number of labels thus have been generated through *de-novo* fatty acid synthesis with glucose as the carbon source.

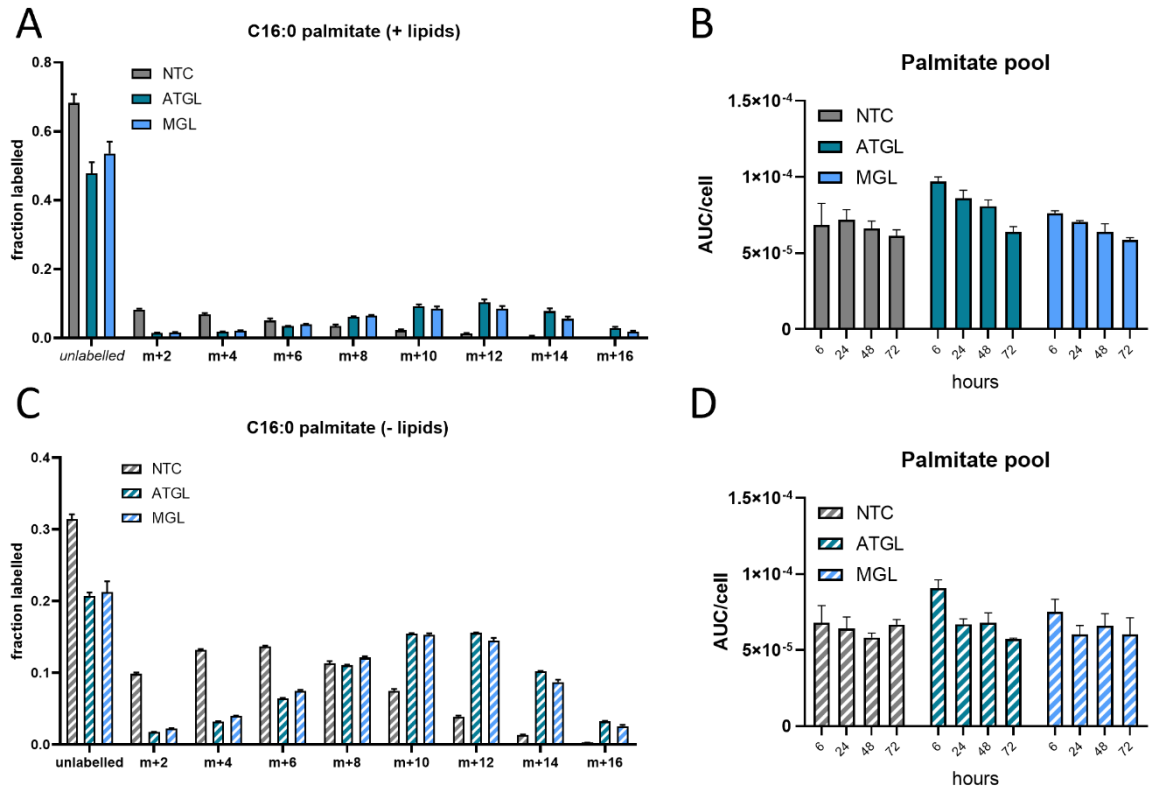

Figure 18: metabolic tracing data of uniformly ^{13}C-labelled glucose into palmitate in A549 (Cas9) cell lines. A: distribution of fractions of palmitate with increasing amount of ^{13}C-label, cells grown in regular (lipid-containing) medium; B: palmitate pool at t = 6 h, 24 h, 48 h or 72 h of cells grown in regular (lipid-containing) medium; C: distribution of fractions of palmitate with increasing amount of ^{13}C-label, cells grown in lipid-depleted medium; D: palmitate pool at t = 6 h, 24 h, 48 h or 72 h of cells grown in lipid-depleted medium. Fractions (A, C) are shown as unlabelled or m+n, where n corresponds to the number of ^{13}C labels derived from glucose that were incorporated; Cells were cultured in respective media for 72 hours, and metabolite levels were normalized to cell counts as well as an internal standard. Metabolite pools (B, D) were determined by combining the peak areas (AUC) of each fraction of palmitate normalized to internal standard and cell counts.

The fraction of unlabeled palmitate was generally higher in cells grown in regular (+ lipid) medium (Figure 18A) compared to cells grown in lipid-deficient (- lipid) medium

(Figure 18C). Correspondingly, the overall sum of fractions of palmitate that was derived to some degree from *de-novo* fatty acid synthesis was higher in all cell lines grown in lipid-depleted media, which corroborates our hypothesis that cells grown in lipid depleted media rely on *de-novo* fatty acid synthesis to a larger degree. More importantly, when looking at the fractional distribution of palmitate it becomes apparent that in both cell lines with lipase deletion (ATGL, MGL) compared to control (NTC) the fraction distribution is shifted to the right, meaning a larger fraction of palmitate that contains carbons derived from glucose (Figure 18A and 18C). This concomitantly shows that a larger fraction of FAs is derived from *de-novo* fatty acid synthesis. This shift of fractional distribution in lipolysis-deficient cells is observed in cells grown in lipid containing (Figure 18A) as well as in lipid-deficient medium (Figure 18C), however, the overall fraction of palmitate derived from glucose is larger in cells grown in lipid deficient medium. It is important to note, that the overall pool of palmitate in cells grown in lipid containing (Figure 18B) or in lipid-depleted medium (Figure 18D) decreases over time from the first harvest at 6h to the last harvest at 72h. However, across the different genotypes (control (NTC), ATGL-KO (ATGL), MGL-KO (MGL)) the levels are comparable at 72h, the timepoint for which the fraction labels are shown. Overall, these findings suggest that, irrespective of the presence of exogenous lipids, A549 cells with deletion of an intracellular lipase (ATGL or MGL) generate more of their fatty acids from *de-novo* synthesis compared to Control cells.

4.6 Measurement of glucose and lactate levels in media

Since the tracing data suggests that more FAs are generated from glucose upon lipolysis deficiency, we were wondering about the overall glucose consumption and lactate production of these cells. We therefore performed glucose/lactate measurements in A549 and H358 (Cas9) cell lines (Figure 19). Surprisingly, A549 Control cells consumed more glucose per cell over time compared to ATGL-KO and MGL-KO cells (Figure 19A). However, the overall lactate production over time per cell was higher in the lipase KO cell lines (Figure 19B), and thus the overall ratio of lactate/glucose, representing the conversion of glucose to lactate was higher in the ATGL-KO or MGL-KO cell lines (Figure 19C). In H358 (Cas9) cell lines, where ATGL-KO and MGL-KO do not cause a similar phenotypic (proliferative)

difference, the glucose uptake (Figure 19D), lactate excretion (Figure 19E) and lactate/glucose ratio (Figure 19F) was relatively similar between any of the three genotypes. This might indicate that a proliferation advantage upon lipolysis deficiency might be dependent on concomitant changes in glucose to lactate conversion.

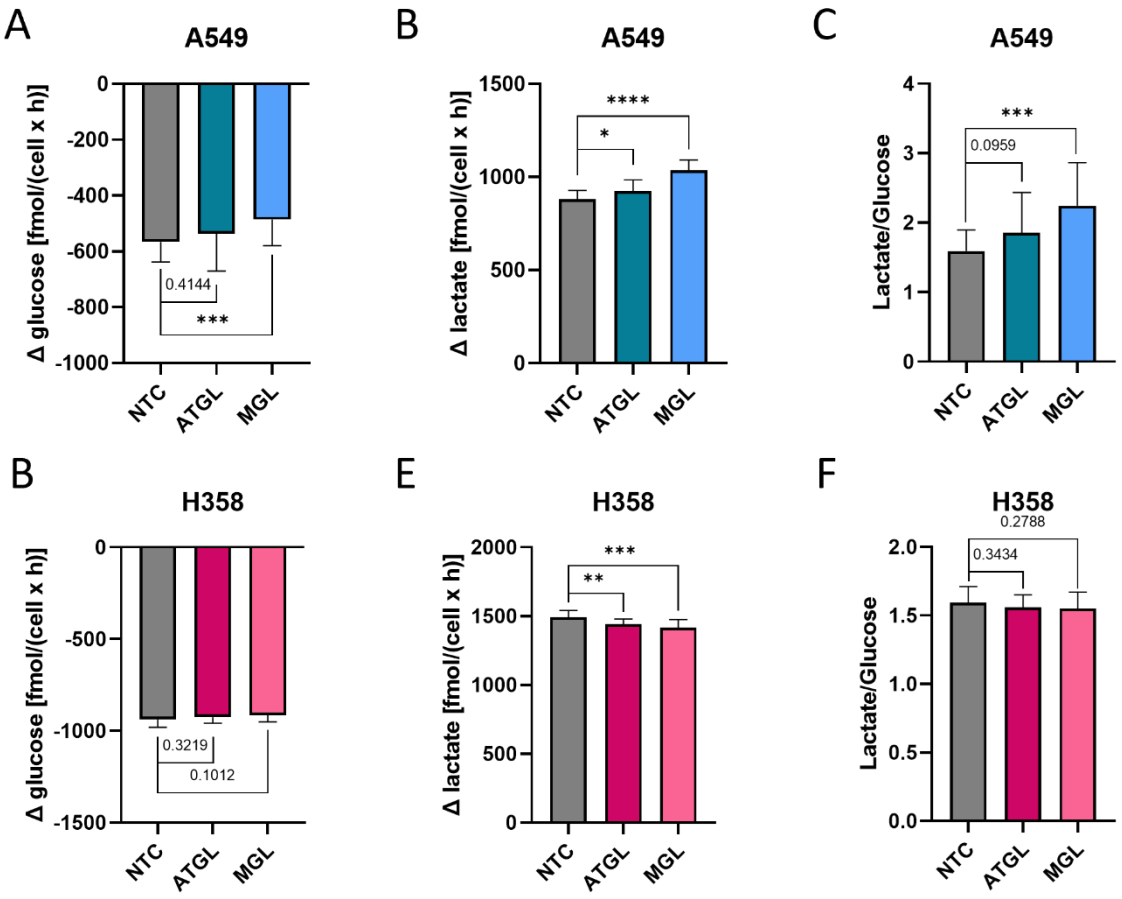

Figure 19: glucose and lactate measurement in media. A/D: change in glucose concentration in the medium of cells grown for 24 hours, normalized to cell count and time (in hours) [fmol/(cell x hour)] in A549 (A) or H358 (D) (Cas9) cell lines; B/E: change in lactate concentration in the medium of cells grown for 24 hours, normalized to cell count and time (in hours) [fmol/(cell x hour)] in A549 (B) or H358 (E) (Cas9) cell lines; C/F: Ratio between the formed lactate and the consumed glucose (arbitrary unit) in A549 (C) or H358 (F) (Cas9) cell lines. (n = 3 technical replicates, n = 3 biological replicates, * $p < 0.05$, ** $p < 0.01$, *** $p < 0.001$)

4.7 Label free quantitative proteomics of NSCLC lipolysis-deficient cell lines

As part of our goal to fully profile the generated panel of cell lines, we performed untargeted label-free quantitative proteomics by LC-MS/MS. Despite several significantly changed proteins (volcano plots and histograms are found in the Appendix, Figure 36-39), there were no signs that hinted towards a change in metabolism. The proteomics data were consistent with our western blot data, and confirmed ATGL loss in ATGL-KO cell lines, with LFQ intensities significantly lower (H441 (Cas9) cells) or not detected in ATGL-KO cell lines (Figure 20A). Furthermore, MGL was generally lower or missing in MGL-KO cell lines, with exception of H358 (Cas9) MGL-KO, where it was detected (Figure 20B). It hast to be noted that MGL could not be detected in H1299 control cells, and the signal from western blot in H1299 cells was low too (Figure 14D). However, MGL might be below the limit of detection in H1299 cells.

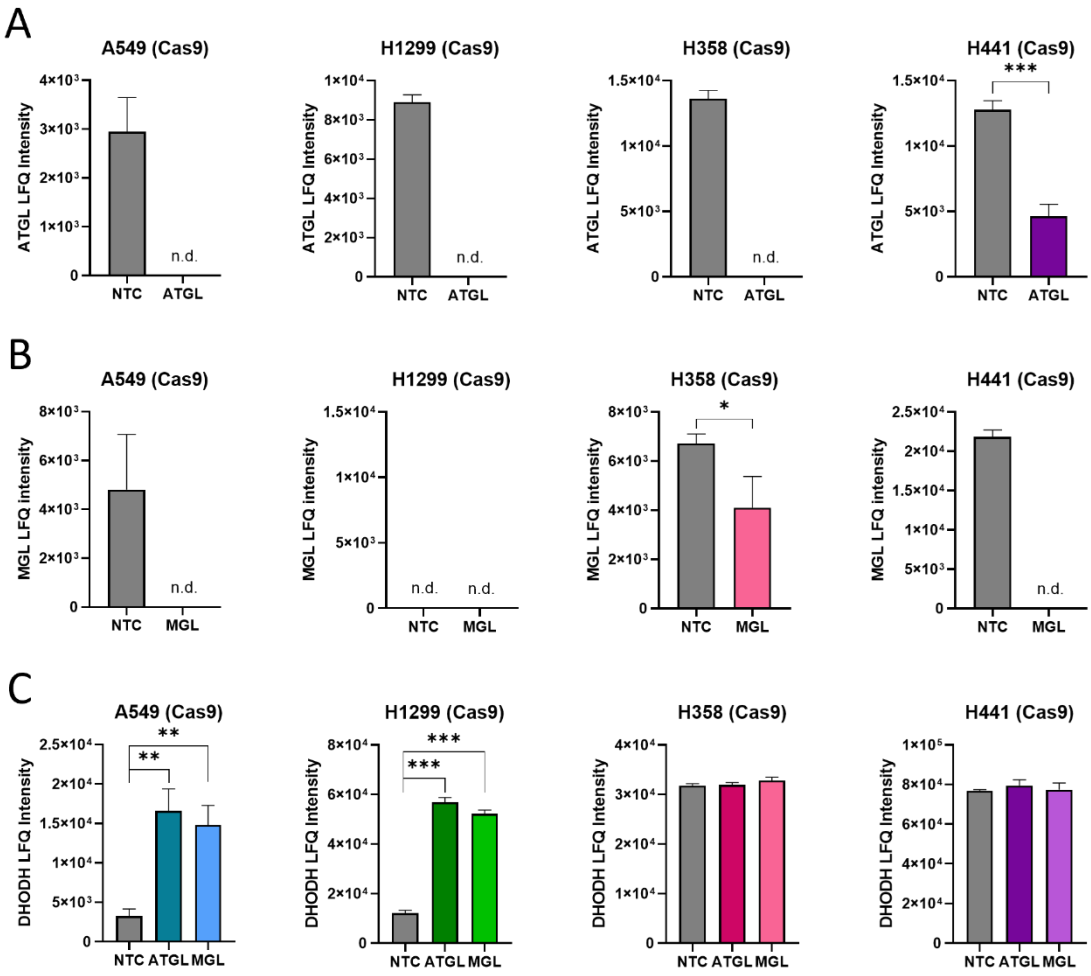

Figure 20: selected protein quantitations from proteomics data of ATGL-KO (ATGL), MGL-KO (MGL) and Control (NTC) NSCLC (Cas9) cell lines. A: abundance (LFQ intensity) of ATGL in control (NTC) and ATGL-KO (ATGL) (Cas9) cell lines B: abundance (LFQ intensity) of MGL in control and MGL-KO (MGL) (Cas9) cell lines; abundance (LFQ intensity) of DHODH in control, ATGL-KO (ATGL), and MGL-KO (MGL) cell lines (n.d. = not detected n = 3, * $p < 0.05$, ** $p < 0.01$, *** $p < 0.001$)

Overall, the proteomics data show that there are more changes observed in the A549 and H1299 cell lines when lipases are knocked out, while relatively little changes were observed in H358 and H441, which is also reflected in the smaller (or lack of) differences in proliferation. One striking observation is that in both A549 and H1299 cell lines, irrespective of the type of lipase that is knocked out, the dihydroorotate dehydrogenase DHODH abundance was elevated (Figure 20C). This observation was not made in the other two cell lines, which did not show the strong increase in proliferation upon ATGL or MGL-KO. DHODH is involved in the synthesis of pyrimidines and has recently been found to support cancer proliferation through ferroptosis defense (186). The potential association of DHDOH with the observed increase in proliferation upon ATGL or MGL knockout can be explored in future experiments using DHODH inhibitors (brequinar or leflunomide).

5 Discussion

It is well-established that cancer cells undergo significant metabolic alterations to sustain their proliferation and cancer characteristics (38). Beyond widely recognized changes in glucose metabolism, changes in FA and lipid metabolism have gained interest more recently (75, 80, 82, 99, 139, 142, 182). FAs are not only essential in proliferating cells for their function as building blocks for biomembranes, but they also play a role in lipid signaling (75, 104). Although the role of lipid droplets in cancer has emerged as a novel hallmark in some cancers (139, 187), the specific role of lipolysis in cancer-associated metabolic changes, particularly regarding the enzymes involved in neutral lipolysis and their coregulators, has remained inconclusive (152, 154, 155, 157, 161, 163, 165, 188). Despite prior evidence of ATGL-KO driving cancer aggressiveness from a study in our lab (154), this study was constrained by relying solely on standard *in-vitro* cell culture models, which do not authentically replicate *in-vivo* conditions.

In this thesis, the impact of ATGL loss on lung cancer cells was reevaluated, and particular attention was paid to the use of alternative cell culture models that simulate conditions closer to solid tumors: 3D spheroid cell culture and CAM assay (169, 178). The comparative analysis of growth of A549 ATGL-KO cells and their controls highlighted a more significant distinction in 3D spheroids and their derived tumors (CAM assay) compared to the 2D monolayer setup (Figure 8 and Figure 11). Notably, we observed a marked shift towards a glycolytic, pro-Warburg phenotype in these 3D conditions (Figure 10 and Figure 13). Unlike the uniform exposure to nutrients and oxygen in monolayer growth, the 3D setup created gradients of oxygen and nutrients, which mimics conditions of *in-vivo* solid tumor formation. Under these conditions, ATGL-KO appeared to play a pivotal role in metabolic adaptation, upregulating glycolytic enzymes and FA metabolism-related proteins (Figure 10 and Figure 13).

Proteomic analysis revealed increased abundance of glycolytic pathway enzymes and glucose uptake proteins, as well as an alternative fatty acid desaturase, in the 3D cell culture model lacking ATGL (Figure 10). In the same cells grown as tumors on the CAM model, even more glycolytic enzymes were upregulated, together with increased levels of fatty acid synthase (Figure 13). Additionally, enzymes associated with the TCA cycle were

found to be upregulated, challenging the belief that mitochondrial pathways are dysfunctional in cancer.

One of the key divergences in the different cell culture models (2D compared to 3D or CAM) is the varied availability of oxygen and nutrients. Both spheroids and tumors grown on CAM assay, which most closely mimics *in-vivo* conditions, revealed traits mimicking solid tumors. Most notably hypoxic core formation was indicated by up regulation of several hypoxia-related proteins. ATGL-KO spheroid-derived tumors showed increased abundance of hypoxia upregulated protein 1 (HYOU1), a protein associated with tumor prognosis (189). Hypoxia triggers metabolic shifts in cancer regulated by HIF transcription factors (93). HIF-induced changes, such as enhanced GLUTs and glycolytic enzymes, were observed in the at least partially hypoxic cell models (3D, CAM) but not in the 2D culture of ATGL-KO cells. These changes also extended to lipid metabolism through FASN upregulation (increased *de-novo* FA synthesis) and PPARγ signaling activation (increased FA uptake) (100). FASN was notably heightened in both ATGL-KO spheroids and derived tumors, correlating with increased de novo FA synthesis. The absence of ATGL further led to lipid droplet accumulation, associated with both cancer and hypoxia, potentially mitigating reactive oxygen species stress (99). Another protein, Perilipin-3, was found to be upregulated in ATGL-KO spheroid-derived tumors, stabilizing lipid droplets, crucial in high LD accumulation (128). Hypoxia also impacts FA metabolism independently of HIFs; we identified an upregulation of an alternative fatty acid desaturase, FADS2, providing an alternative pathway for MUFA synthesis when the primary desaturase SCD1 is inhibited (182).

Despite expanding on our previous findings by employing more advanced 3D cell culturing techniques, these findings are limited because data was derived from only one cell line (A549 (CLS) ATGL-KO and Control clonal cell lines). To rule out the possibility that the observed changes are only specific to this one cell line and not to lung cancer in general, we turned to additional lung cancer cell lines. Through the generation of lipolysis-deficiency by ATGL- or MGL-KO in additional cell lines we aimed to expand the research question on how lipid hydrolases impact lung cancer cell lines.

The previously observed increase in proliferation of lipolysis-deficient (ATGL-KO) A549 cell lines (1, 154) was reproduced in A549 ATGL-KO cells generated by a new CRISPR-

Cas9 technique (Figure 16). Strikingly, a similar phenotype was also observed upon deletion of MGL (Figure 16). These observations highlight the importance of both ATGL- and MGL-mediated lipolysis in regulating the behavior of A549 lung cancer cells. Furthermore, we demonstrate that the deletion of ATGL as well as MGL caused increased proliferation in another lung cancer cell line, H1299 (Figure 16). However, the loss of ATGL or MGL in two other lung cancer cell lines either caused the opposite effect on proliferation (H358 cells) or caused minor or no increase in proliferation (H441 cells). Interestingly, H358 cells also showed the least lipid droplet accumulation upon ATGL-KO (Figure 15). This discrepancy might indicate a complex relationship between lipid metabolism and cell proliferation that warrants further exploration. Additional experiments focusing on the metabolic differences between H358 and the other cell lines will help shed light onto the reason of these phenotypic differences.

The knockouts of ATGL and MGL were validated through immunoblotting and functional assays like LD assessment (Figure 14 and Figure 15). All ATGL-KO cell lines caused increased lipid droplet content compared to Controls (Figure 15), supporting efficient ATGL-KO in these cell lines. ATGL and MGL protein expression was also assessed by quantitative proteomics (Figure 20). Both the western blot as well as the proteomics data revealed residual MGL expression in H358 MGL-KO cells, and proteomics data revealed residual ATGL expression in H441 ATGL-KO cells (Figure 14 and Figure 20). Furthermore, proteomics was unable to detect MGL in H1299 Control cells, however, this might be due to expression below the limit of detection. Data from the depmap portal (https://depmap.org/portal/interactive/ accessed on 10.11.2023) corroborated the presence of MGL expression in H1299, albeit at a lower level compared to the other examined cell lines.

The proteomics analysis of the generated cell lines exposed some significantly different proteins between Control and ATGL- or MGL-KO cell lines in all cell lines (Figure 36 and 38). Even though no discernible changes were noted in glucose metabolism, which was observed in ATGL-KO 3D spheroid and ATGL-KO spheroid-derived CAM tumors, an interesting observation emerged: the enzyme DHODH, related to pyrimidine synthesis, showed increased activity following the knockout of ATGL or MGL. This effect was consistent

in both cell lines, A549 and H1299, where the absence of the lipase notably enhanced proliferation, but not in the other two cell lines (H358, H441) (Figure 20C). DHODH is coupled to the respiratory chain and has been found to support cancer proliferation (186, 190). The increased proliferation in A549 and H1299 cells upon lipase knockout might be dependent on increased DHODH activity, and this avenue can be further investigated through experiments involving DHODH manipulation or inhibitors (e.g., brequinar or leflunomide).

Metabolic tracing using stable-isotope labeled U-^{13}C-glucose provided valuable insights into how lipolysis deficiency (through ATGL- or MGL-KO) influences the metabolism of the generated cell lines. The data revealed an increase in *de-novo* fatty acid synthesis in A549 cells lacking ATGL or MGL, two enzymes important in intracellular lipolysis (Figure 18). This finding suggests a compensatory mechanism in these cells to maintain fatty acid availability for various cellular processes. Expanding the scope of our tracing experiments to include other tracers like U-^{13}C-glutamine and exploring additional pathways, such as glutamine's role in pyrimidine production, using suitable methods to measure labeled pyrimidines, will further illuminate the metabolic needs of cells deficient in lipolysis. Extending these experiments to the other cell lines will provide a comprehensive understanding of these dependencies.

The A549 lipolysis-deficient cell lines further showed increased production of lactate and subsequently increased ratios of lactate/glucose when compared to Control cells (Figure 19). This phenotype was not observed in H358 cells, in which knockout of ATGL or MGL caused decrease in proliferation (Figure 16). The preferential generation of lactate from glucose instead of fueling into TCA cycle can help cells regenerate NAD^+, which can be limiting to support oxidation reactions in proliferating cells (191). Furthermore, lipid metabolism influences cellular redox state through fatty acid synthesis (consumption of NADPH) or oxidation (production of NADPH). Therefore, studying the $NAD(P)^+$/NAD(P)H ratios in lipolysis deficient cell lines might provide further understanding on how lipid hydrolases or their loss contribute to different cancer phenotypes.

In conclusion, the results of this study support the crucial role of intracellular lipid catabolism enzymes, particularly ATGL and MGL, in lung cancer progression and

metabolism. Deletion of ATGL or MGL was associated with increased proliferation in some cell lines (A549, H1299), while metabolic alterations indicated a compensatory shift in glucose and fatty acid metabolism. As shown in our published study on the influence of ATGL-KO in 3D spheroids and CAM tumor models (1), the use of adequate cell culture model systems that better reflect *in-vivo* conditions can have significant impact on the observed phenotype, given that numerous phenotypic insights observed in 3D and CAM models were distinct from those observed in 2D culture experiments. Therefore, further exploration of all of the lipolysis-deficient cell lines in more *in-vivo* like cell culture models are justified.

Chapter Two: Altered lipid hydrolysis in tumors of non-small cell lung cancer patients

6 Introduction to activity-based proteomic profiling for the evaluation of relative lipase activities in lung tumors

Metabolic alterations in tumors are pivotal for their proliferation and survival (25). While some pathways – and enzymes therein – of glucose, glutamine, and lipid metabolism have been extensively linked to cancer, the exploration of lipid hydrolases in the cancer context remains relatively understudied (32, 71, 75). Although some studies have focused on specific lipid hydrolases in the context of cancer, these have predominantly been conducted in cancer cell line models, posing challenges for translation into *in-vivo* situations where the tumor microenvironment and other factors contribute to cancer progression (16). Approaches such as 3D cell culture or CAM models offer more *in-vivo*-like conditions but have limitations and do not fully recapitulate real *in-vivo* scenarios (169, 178). Another avenue involves using model organisms, with mouse models being popular, yet discrepancies between mice and humans complicate the translation of findings.

For some study questions, direct sampling and analysis of patient tissues provide valuable insights, especially in descriptive studies aimed at finding deregulated pathways. Large-scale cancer patient studies analyzing the genome and transcriptome gained a lot of insight, although gene expression does not always align with protein expression levels due to post-transcriptional and post-translational modifications (192). Recent advancements in technology and data analysis facilitate large-scale patient sample studies beyond transcriptomics and have reached the proteomics field (193, 194), offering additional insights.

The role of lipid mobilization from intracellular stores in lung cancer cells remains inconclusive. Despite studies on intracellular lipid hydrolysis cascade enzymes in (lung) cancer cell models and animals, findings are conflicting (152, 154, 161, 163, 164, 165, 188). Given the nature of lipolytic enzymes, which are often regulated at the post-translational level through phosphorylation or coregulators (109, 118, 124), their enzymatic activity

might not be portrayed by gene expression and/or protein expression, which makes studying them challenging.

Hypothesizing that lipid hydrolysis is deregulated in lung tumors, we aimed to investigate lipid hydrolysis in a broader sense in tissues derived from tumors as well as normal tumor-adjacent tissue of lung cancer patients. To investigate lipid hydrolysis, we did not only check gene expression levels of lipolytic enzymes and their coregulators, but more importantly employed LC-MS/MS-based lipidomics and proteomics analyses. Due to the challenges in studying lipases, we turned towards activity-based proteomic profiling (ABPP), which is a special proteomics technique that enables the identification of relative enzyme activities across multiple samples. This method is enabled by using a serine hydrolase-directed probe that covalently binds to serine hydrolases, including lipases, and it provides an additional layer of evidence to gene expression and proteomics analyses.

7 Material and Methods

7.1 Patient tissue

Lung tissue was excised during surgery of non-small cell lung cancer patients and sent immediately to the Institute of Pathology at Medical university of Graz for investigation of the tissue. Small pieces (ca. 1 x 1 mm) of tissue (tumor and normal tumor-adjacent (NTA)) were cut and collected in Eppendorf tubes containing 1 ml PBS (control) or 30 µM activity-based probe (ABP) (Hexyl 4-nitrophenyl (3-azidopropyl)phosphonate)) (Figure 21A) in PBS for activity-based proteomic profiling. Additional pieces of tissue (2 each ca. 4 x 4 mm) were collected for subsequent RNA/protein extraction, proteomics sample preparation as well as lipidomics sample preparation. Samples were briefly rinsed with PBS and then flash frozen and and stored in liquid Nitrogen.

7.2 RNA extraction and qPCR

RNA extraction was performed using TRIzol reagent (Invitrogen) according to manufacturer's protocol. Briefly, samples (n = 25 patients, paired tumor and NTA) were transferred on liquid nitrogen and tissue was weighed and immediately transferred into 1 ml of TRIzol reagent (#15596026, Thermo Fisher) at room temperature. Samples were homogenized using a rotor stator homogenizer (Miccra, Germany), briefly incubated (5 min) and 200 µl chloroform was added followed by incubation for 3 min. After centrifugation at 12,000 x g at 4 °C for 15 min, the upper aqueous phase was transferred into RNAse free Eppendorf tubes for RNA extraction. The lower chloroform phase and interphase were kept for subsequent protein extraction. To the RNA fraction, 500 µl isopropanol was added, the tube was thoroughly inverted and incubated for 10 minutes followed by centrifugation at 12,000 x g at 4 °C for 10 min. The RNA pellet was washed once with ethanol, dried and redissolved in 50 µl of RNase free water. The quality and concentration of RNA was assessed on a NanoDrop spectrophotometer.

RNA was reverse transcribed into cDNA with the QuantiTect Reverse Transcription kit (#205311, Qiagen) according to manufacturer's protocol. Briefly, samples corresponding to 1 µg RNA were incubated with gDNA wipeout buffer to get rid of any transferred genomic DNA. A master mix containing reverse transcriptase, reverse transcriptase buffer (including

nucleotides) as well as reverse transcription primer mix was added to the RNA samples and incubated for 15 min at 42 °C followed by incubation for 3 min at 95 °C and storage of cDNA at -20 °C.

For qPCR, cDNA samples were diluted 1:5 in RNase free water (= ca. 10 ng / µl) and RNA primer working solutions were prepared by diluting 100 µM primer stocks 1:10 to yield 10 µM of each primer e.g., 80 µl nuclease-free H_2O + 10 µl primer forward (100 µM) + 10 µl primer reverse (100 µM). Genes of lipolysis enzymes as well as their regulators were tested (*PNPLA2*, *LIPE*, *MGLL, HIG2; ABHD5*) as well as two control genes (*ACTB*, *EEF1A1*) for normalization. Primer sequences are listed in Table 1. A master mix was prepared with 5 µl Maxima SYBR Green/ROX qPCR Master Mix (2X) (#K0221, Thermo Fisher), 0.4 µl RNA working solution and 3.6 µl nuclease-free water per reaction. The primer-specific master mix was distributed (9 µl) into the wells of a hard shell 384-well plate (Bio-Rad), and subsequently, 1 µl of cDNA was added to the wells, the plate was sealed, briefly spun down and placed in a CFX384 real-time PCR detection system (BioRad).

For data analysis, mean Ct values of sample and for each gene were calculated, and the delta Ct value was calculated by subtracting the mean Ct value of the gene of interest from the mean Ct value of both control genes combined. The fold change was then calculated accordingly (= 2^ΔCt).

7.3 Lipidomics sample preparation and LC-MS measurement

For lipidomics sample preparation, a piece of tissue was cut (ca. 1.5 x 1.5 mm) from each tissue sample (n = 25 patients, paired tumor and NTA) and transferred into a BeadBug prefilled tube (#Z763829, Sigma Aldrich) filled with 500 µl chloroform and 250 µl methanol. The tissue was homogenized in a MagNA Lyser (Roche) twice for 25 sec at 6,500 rpm and placed immediately back on ice. 600 µl of the suspension was transferred into a n MS glass vial (Bruckner) and 10 µl of EquiSPLASH™ LIPIDOMIX® Quantitative Mass Spec Internal Standard (#330731, Avanti) was added and incubated for 1 hour on ice. The samples were thoroughly vortexed and 150 µl water added, vortexed again and centrifuged for 15 min with 7,197 x g at 4 °C. The lower chloroform phase was transferred into a new MS vial and extraction was repeated. The chloroform phases were combined and evaporated in 50 µl

steps in MS vial glass inserts with a Heto Vacuum Centrifuge. The residual methanol/water phase was used for protein quantification using a Pierce™ BCA protein assay (#23225, Thermo Fisher) for normalization. The dry lipids were resuspended in 30 µl of a 90:5:5 isopropanol:chloroform:methanol (vol:vol:vol) mixture and were kept at -80 °C until measurement.

The lipids were separated by HPLC (Dionex Ultimate 3000, Thermo Fisher Scientific) equipped with a Waters BEH column (C8, 1.7 µm, 100 x 1 mm) at 50 °C and at a flow rate of 150 µl / min with following gradient: 50 – 100 % B 0 – 42 min; 100 % B 42 – 50 min; 50 % B 50 – 57 min; solvent A: H_2O with 10 mM ammonium formate and 0.1 % formic acid and solvent B: a 5:2 mix (vol:vol) of ACN/isopropanol with 10 mM ammonium formate and 0.1 % formic acid. HPLC was coupled to an Orbitrap Velos Pro (Thermo Fisher Scientific) operated in positive mode and CID of the top 10 most abundant ions. Data analysis was performed using the Lipid Data Analyser (LDA) software (version 2.7.0) (195). The results were normalized to internal standards and total ion chromatogram (TIC).

7.4 Proteomics sample preparation and LC-MS measurement

From each tissue sample (n = 25 patients, paired tumor and NTA) a piece was cut (ca. 1.5 x 1.5 mm) and transferred into an Eppendorf tube with 200 µl lysis buffer (= 10 mM TCEP, 40 mM CAA, 1 % SDS, 100 mM TrisHCl (pH = 8.5)). The samples were homogenized using a rotor stator homogenizer (Miccra, Germany) and the tissue and cell debris was removed by centrifugation (14,000 x g, 5 min, 4 °C). The samples were heated to 95 °C for 10 minutes and protein estimation was performed using the Pierce™ BCA protein assay (#23225, Thermo Fisher). 100 µg were used for acetone precipitation and the obtained protein pellet after centrifugation at 14,000 x g for 10 min at 4 °C was dissolved in 50 µl of 25 % TFE and brief sonication using a sonication probe. The samples were brought to 10 % TFE by addition of 100 mM ammonium bicarbonate and digested with 1 µg sequencing grade modified trypsin (#V5111, Promega) at 37 °C overnight. The samples were further desalted on self-packed 2-layer 200 µl styrenedivinylbenzene-reversed phase sulfonate (SDB-RPS) Stage Tips (#2241, Empore SPE Disks, Sigma-Aldrich), dried in a vacuum concentrator centrifuge, and redissolved in 2 % ACN, 1 % formic acid. Peptides were separated by nano-HPLC coupled to a timsTOF (Bruker, Germany) mass spectrometer in

positive mode in DIA mode. Data analysis was carried out using Dia-NN (177) and Perseus (version 1.6.12.0) (175). The proteomic data were further subjected to pathway analysis using the String functional protein database (version 11.5).

The shotgun DIA proteomics data of tumors and normal tumor-adjacent tissue have been deposited to the ProteomeXchange Consortium via the PRIDE (176) partner repository with the dataset identifier PXD046998.

7.5 Activity-based proteomic profiling (ABPP) sample preparation and LC-MS measurement

Samples (n = 12 patients, paired tumor and NTA, control & ABP) were thawed and sonicated thoroughly using a sonication probe while kept on ice. After removing tissue and cell debris by centrifugation at 7,000 x g for 10 min at 4 °C, the protein content was quantified using a Pierce™ BCA protein assay (#23225, Thermo Fisher), and 100 µg were used for acetone precipitation. Protein pellets were obtained by centrifugation at 18,000 x g for 10 min at 4 °C and were resolubilized in 10 mM TCEP, 1 % SDS in TrisHCl (pH = 8.5), followed by incubation at 95 °C for 10 min. Samples were brought to 30 mM N-ethylmaleimide (NEM) and incubated at 37 °C for 30 min.

Excess of DBCO-TEV-Biotin strain promoted click linker (Figure 21B) was added and incubated on a shaker at 37 °C and 500 rpm overnight, which allowed for click reaction. Samples were diluted 1:10 to reduce SDS concentration and excess of linker, TCEP and NEM was removed by 3 kDa cut-off centrifugal filters (#UFC5003BK, Amicon, Millipore). The retentate was washed twice with 8 M urea in 100 mM TrisHCl (pH = 8.5) and once with 2 M urea in 100 mM TrisHCl (pH = 8.5) followed by enrichment on streptavidin-agarose resin (Thermo Scientific) in spin columns (#69705, Thermo Scientific) on an overhead rotor for 4 hours. After washing of beads with 2 M urea in 100 mM TrisHCl (pH = 8.5), proteins on the beads were digested by 1:100 sequencing grade modified trypsin (#V5111, Promega), overnight. The digests were collected into Eppendorf tubes by centrifugation at 500 x g for 5 min and brought to 1 % trifluoroacetic acid (TFA). The samples were desalted on self-packed 2-layer 200 µl SDB-RPS Stage Tips (#2241, Empore SPE Disks, Sigma-Aldrich). The samples were loaded onto the stage tips and passed through the SDB-RPS material through

centrifugation at 1,500 x g for 10 minutes followed by a wash with 0.2 % TFA and elution into glass inserts with 5 % NH_4OH, 80 % ACN. Samples were dried in a vacuum concentrator centrifuge and redissolved in 2 % ACN, 1 % FA. Peptides were separated by nano-HPLC coupled to a timsTOF (Bruker, Germany) mass spectrometer in positive mode in DDA mode. Data analysis was carried out using MaxQuant (version 1.6.17.0) (174) and Perseus (version 1.6.12.0) (175). A schematic representation of the workflow is shown in Figure 21C.

The ABPP proteomics data of tumors and normal tumor-adjacent tissue have been deposited to the ProteomeXchange Consortium via the PRIDE (176) partner repository with the dataset identifier PXD046934.

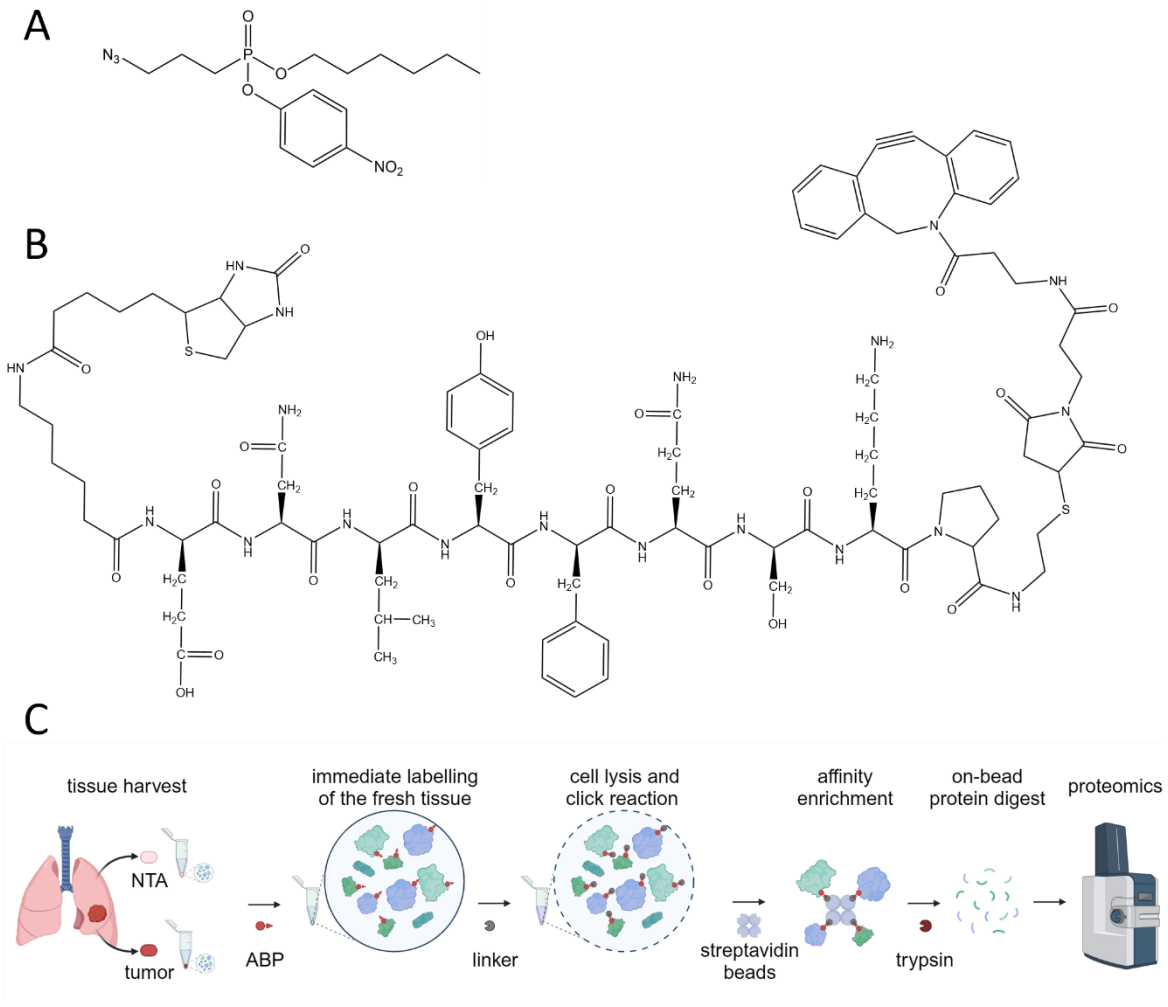

Figure 21: activity-based proteomic profiling workflow. A: Activity-based probe (ABP): Hexyl 4-nitrophenyl (3-azidopropyl)phosphonate); B: Linker: DBCO-TEV-Biotin strain promoted click linker; C: ABPP workflow schematic overview (Created with BioRender.com)

8 Results

Tissue from tumors as well as Normal Tumor-Adjacent (NTA) regions of 25 non-small cell lung cancer patients that underwent surgical removal of the tumors were collected in collaboration with the Institute of Pathology at the Medical University of Graz. From 25 patients, 64 % were male, and the rest (36 %) were female. The tumors were histologically analyzed and categorized by their subtype: 48 % of tumors were lung adenocarcinomas, 32 % were lung squamous cell carcinomas, 8 % were adenosquamous carcinomas, and 4 % were large cell lung carcinoma. Tumors of two patients could not be assigned a histological subtype due to few or no tumor cells after medication. These data were excluded from analyses. The patient data (sex, histological subtype, analyses) is summarized in Table 5.

Table 5: patient data

Patient #	Sex	Histological subtype	Analysis Info
1	male	LUSC	no ABPP
2	female	LASC	no ABPP
3	female	LUAD	no ABPP
4	male	LASC	all analyses
5	male	LUSC	all analyses
6	female	-	excluded
7	male	LUAD	no ABPP
8	male	LUSC	all analyses
9	male	LUAD	no ABPP
10	male	LUAD	no ABPP
11	male	-	excluded
12	female	LUAD	all analyses
14	female	LUAD	no ABPP
13	female	LUAD	no ABPP
15	male	LUSC	all analyses
16	male	LUAD	all analyses
17	male	LUSC	all analyses
18	female	LUAD	all analyses
19	female	LUAD	all analyses
20	male	LUSC	no ABPP
21	male	LUAD	no ABPP
22	male	LUAD	all analyses
23	female	LUSC	no ABPP
24	male	LCLC	all analyses
25	male	LUSC	no ABPP

The collected samples were analyzed by means of several bioanalytical methods to investigate if lipid hydrolysis is deregulated in lung cancer *in-vivo* setting in humans. To this end, we first employed qPCR to analyze the gene expression of lipolytic enzymes and their coregulators. To better characterize the differences between tumors and adjacent tissue we also employed multiple "omics" techniques. These include activity-based proteomic profiling, label-free quantitative proteomics, as well as lipidomics, all through LC-MS/MS. A graphical representation of the used techniques is depicted in Figure 22.

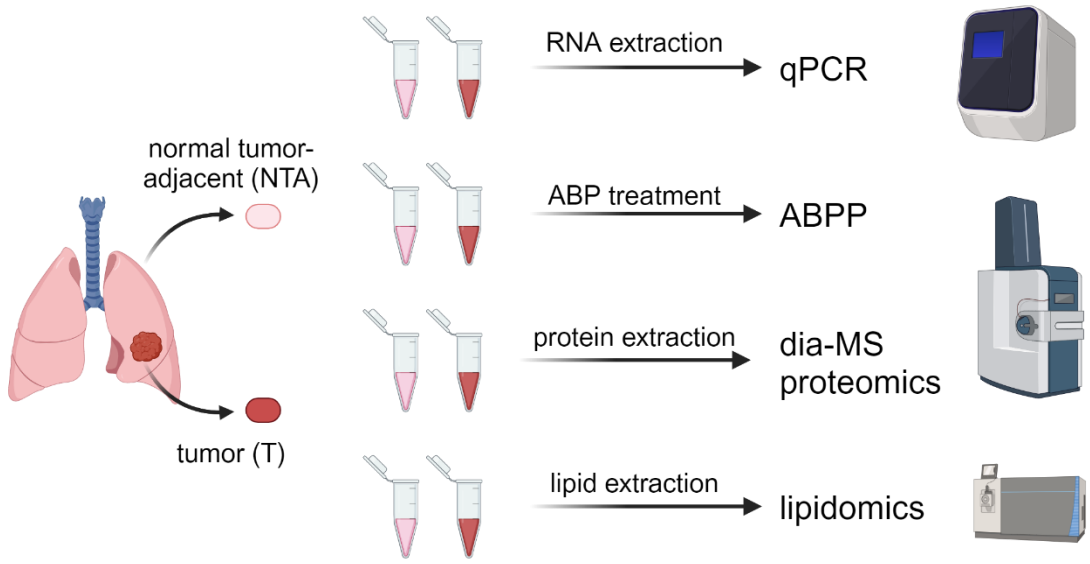

Figure 22: graphical representation of the study design (Created with BioRender.com)

8.1 Gene expression analysis hints towards deregulated neutral lipolysis in NSCLC

Lipid hydrolysis from intracellular lipid stores (lipid droplets) is catalyzed by three main lipid hydrolases: ATGL (*PNPLA2*), HSL (*LIPE*) and MGL (*MGLL*), each responsible for one step of the degradation of triglycerides. To study if lipid hydrolysis is deregulated in lung cancer, we investigated the gene expression of those enzymes in tumors (T) and adjacent (NTA) tissue from lung cancer patients by qPCR. While the gene expression of *PNPLA2* and *LIPE* are not significantly changed (Figure 23A and 23B), those enzymes are also more regulated at the post-translational level. HSL is strongly regulated through phosphorylation

(102, 116). ATGL, on the other hand, is mainly regulated through association with inhibitory or activating proteins like HILPDA or CGI-58 (118, 122).

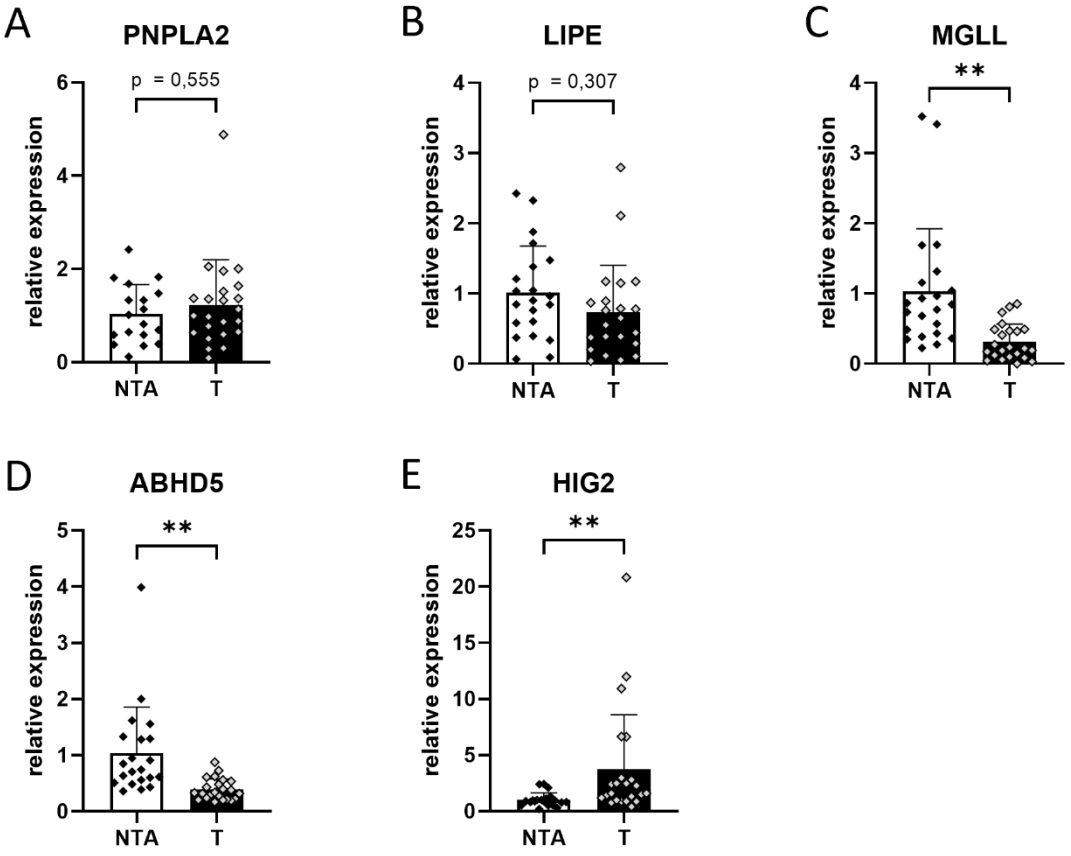

Figure 23: gene expression analysis of paired tumor and normal tumor-adjacent (NTA) tissue from NSCLC patients. A: expression of *PNPLA2* (ATGL); B: expression of *LIPE* (HSL); C: expression of *MGLL* (MGL); D: expression of *ABHD5* (CGI-58, activator of ATGL); E: expression of *HIG2* (HILPDA, inhibitor of ATGL). gene expression normalized to two housekeeping genes (*EEF1A1* and *ACTB*) and to NTA (n = 23 biological replicates, * $p < 0.05$, ** $p < 0.01$, *** $p < 0.001$)

Accordingly, we also checked the gene expression of the two major interactors of ATGL: HILPDA (*HIG2*) and CGI-58 (*ABHD5*). Remarkably, there were significant gene expression differences in both genes when tumors were compared to adjacent tissue. *ABHD5* expression is significantly lower, while *HIG2* expression is higher in the tumors (Figure 23D and 23E). These findings overall point towards lower activity of ATGL in lung tumors, either through inactivation by HILPDA or lack of activation through CGI-58.

Monoglyceride lipase has no known coregulators and is regulated at the transcriptional level by transcription factors like PPARα (102, 116). Strikingly, we find that the gene encoding for monoglyceride lipase (*MGLL*) is significantly lower in tumors of NSCLC patients compared to adjacent tissue (Figure 23C). Taken together, these data provide evidence that lipid hydrolysis enzymes are deregulated in lung tumors either at transcriptional level or through other regulatory mechanisms.

8.2 Changes in the lipidome of Tumors compared to Normal Tumor-Adjacent Tissue

Although gene expression analysis can provide important hints towards pathways that might be deregulated, additional analyses can shed light onto what is happening at a functional level. We hypothesize that if lipid hydrolysis is indeed aberrant in lung tumors, the tumors will display a changed lipidome. To this end, we employed untargeted lipidomics analysis to investigate changes in lipids between the tumors and NTA tissues.

The abundance of individual lipid species, reflected by the area under the curve (AUC) as analyzed by LDA software (195), was normalized to an internal standard (different for each lipid class), and finally to the total ion chromatogram (TIC) of the lipidomics run of a sample, which reflects the injected sample amount. The sum of all lipid species within a lipid class was calculated to check for changes in whole lipid classes between tumors and NTA tissue. The results are shown in Figure 24A.

While diglycerides (DG) were lower in lung tumors, triglycerides (TG) and monoglycerides (MG) were higher, albeit TGs did not pass significance threshold. These observations may also imply decreased TG and MG hydrolysis in tumors, which was indicated by the gene expression data. When looking at sphingolipids, sphingomyelins appeared to be lower (n.s.) in tumors, while ceramides were significantly higher, which could point towards increased activity of sphingomyelinases, a process that is usually associated with apoptosis (196, 197). Within the phospholipid (PL) classes, phosphatidylglycerols (PG) were overall lower in tumors, while phosphatidyl serine (PS), phosphatidylcholine (PC) and phosphatidylethanolamine (PE) appeared to be higher in

tumors (PS, PC: n.s., PE: $p < 0.05$). Lysophosphatidylcholines (lysoPC) appeared to be unchanged overall, while lysophosphatidylethanolamines (lysoPE) were lower in tumors (Figure 24A).

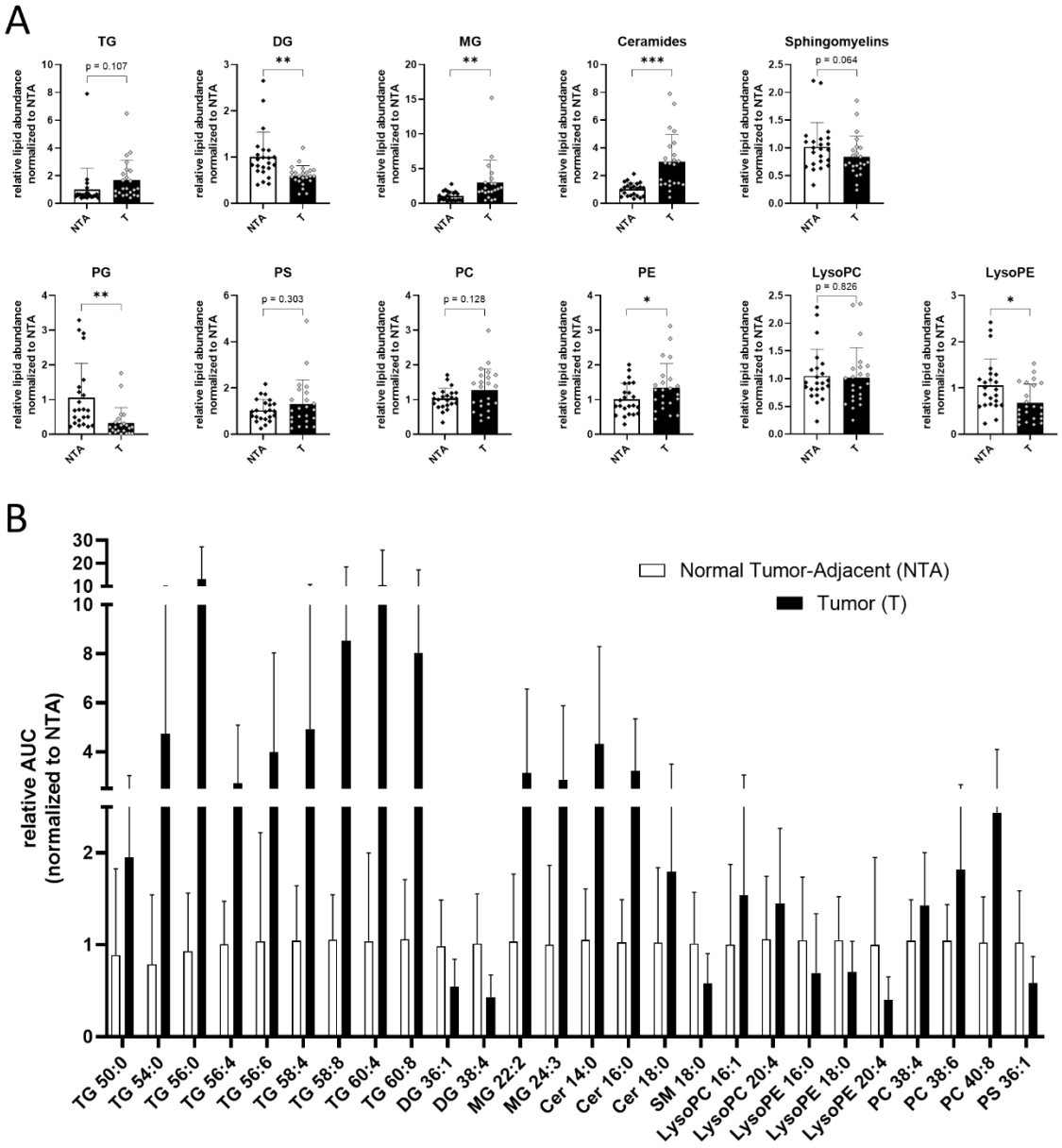

Figure 24: changes in the abundance of lipid classes and individual lipid species in NSCLC Tumors (T) compared to Normal Tumor-Adjacent (NTA) tissue. A: abundance of whole lipid classes (sum of all individual species) normalized to internal standard (IS), total ion chromatogram (TIC) and NTA (paired t-tests, * $p < 0.05$, ** $p < 0.01$, *** $p < 0.001$); B:

selected individual lipid species that passed multi-testing corrected statistical testing and are significantly different between the two groups (threshold was set to 5 % and multiple t-test correction was performed by a two-stage linear step-up procedure of Benjamini, Krieger and Yekutieli, where each row was analyzed individually, without assuming a consistent SD). (n = 23 biological replicates)

We then looked at individual lipid species and found several species that are significantly changed in the lung tumors. Figure 24B displays selected lipid species that passed a significance threshold after multi-testing correction. Concomitant with lower overall DG abundance and higher overall MG abundance in tumors, some individual DG species were found to be lower and some individual MG species were higher in tumors. A similar trend was observed for Cer species (higher) and SM species (lower) in tumors. Although lysoPCs were not changed overall, two lysoPC species (lysoPC 16:1 and lysoPC 20:4) were significantly higher in the lung tumors. These lipid species have been found to play a role in release of inflammatory cytokines (198). LysoPEs, on the other hand, are significantly lower in the tumors, as suggested by the overall lower lysoPE level. Although both PS and PC were not significantly changed overall, several individual PCs were higher in the lung tumors, while PS 36:1 was significantly lower. The most striking differences, however, were observed in the triglyceride lipid class. Although the overall lipid class appeared to be increased in the tumors (Figure 24A), albeit it did not pass significance threshold, many of the individual TG species were significantly elevated in lung tumors (Figure 24B). Notably, not all TG species were significantly higher in the tumors (Figure 15A). However, when looking across different TG species, it became apparent that especially longer chained TGs were significantly elevated in tumors. This can be seen at individual TG species level (Figure 25A) and when TGs of equal chain length are combined (Figure 25B).

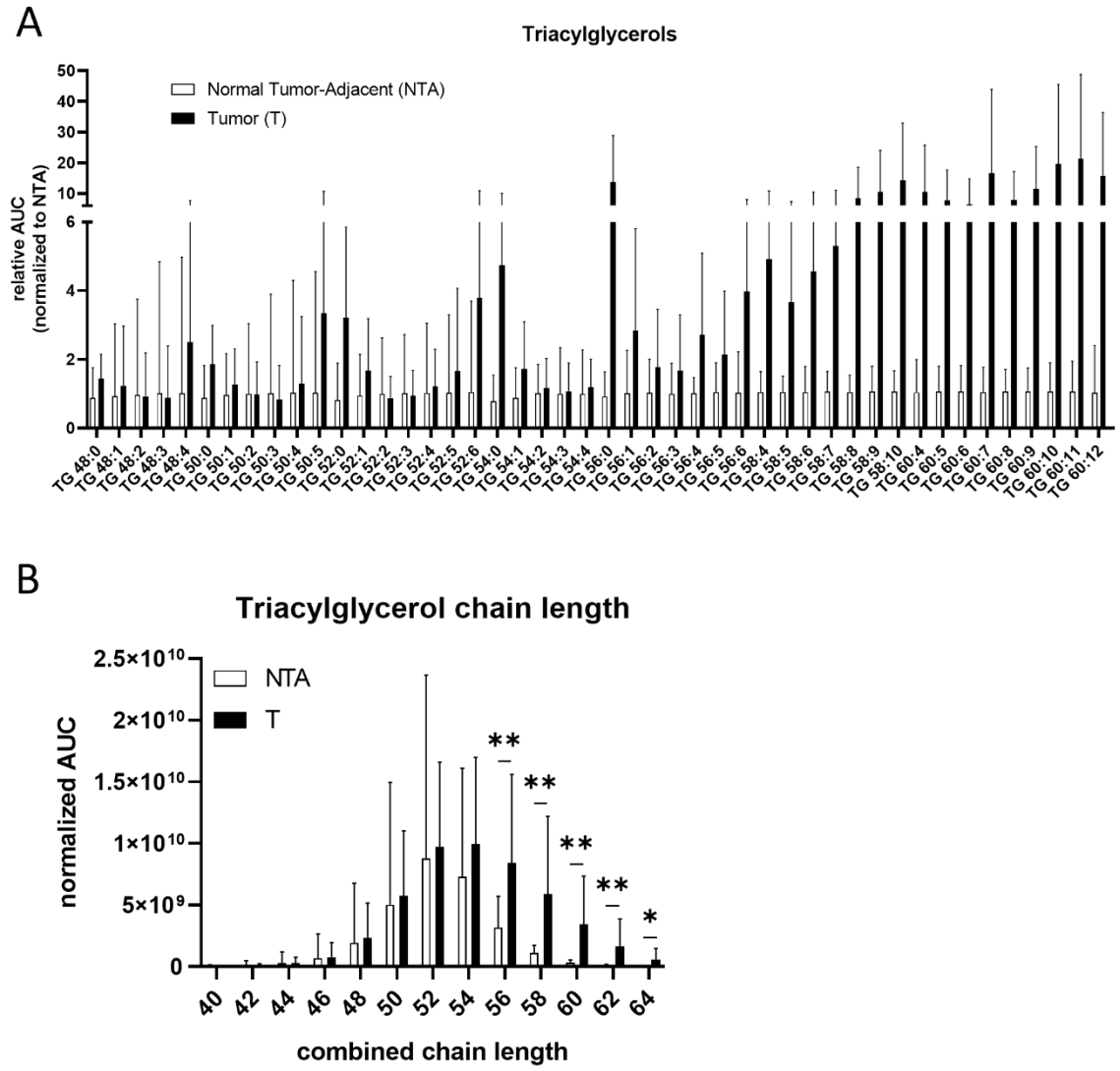

Figure 25: altered triglyceride (TG) species in tumors (T) compared to normal tumor-adjacent (NTA) tissue from NSCLC patients. A: abundance (AUC) of individual TG species was normalized to internal standard (IS) and total ion chromatogram (TIC) and is shown normalized to mean NTA of each individual species; B: sum of all TGs with a given combined side chain length, AUC normalized to IS and TIC; (n = 23 biological replicates, paired t-tests, * $p < 0.05$, ** $p < 0.01$, *** $p < 0.001$)

8.3 Analysis of the proteome of lung tumors and tumor-adjacent tissue reveals changes in pathways involved in lipid hydrolysis and metabolism

In addition to the gene expression and lipid analysis we aimed to explore changes on the protein level between tumors and NTA tissue through label-free quantitative proteomics. The proteomics data were pre-processed as described in the methods section and obtained LFQ intensities were log2 transformed and reduced to contain only proteins with at least 90 % valid values in total (matrix reduction from 8912 proteins to 5381 proteins). The remaining missing data were not imputed (histograms in Appendix Figure 40). The data was then subjected to two sample t-test with permutation-based false-discovery rate of 5 % and is visualized as volcano plot in Figure 26.

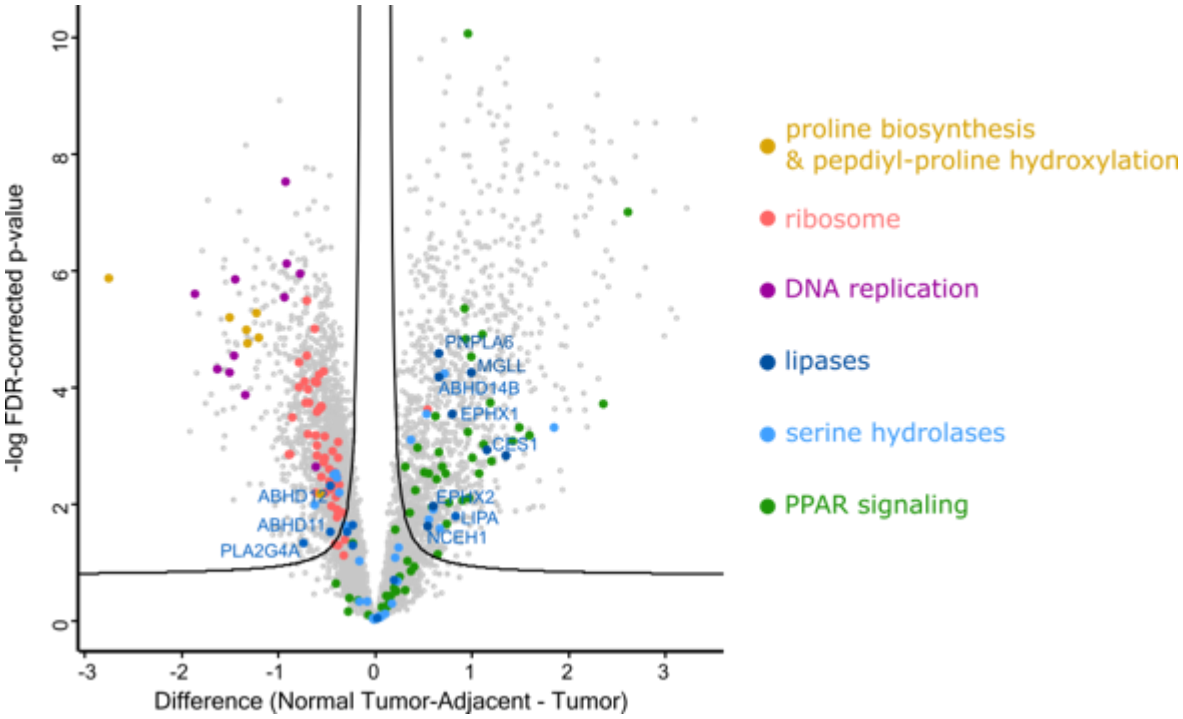

Figure 26: LFQ shotgun proteomics of paired Tumor (T) and Normal Tumor-Adjacent (NTA) tissue from NSCLC patients. Proteins of selected pathways (shown right to the volcano plot) are marked in color and selected lipases are shown in blue text – proteins were filtered to contain at least 90 % valid values; missing values were not imputed (n = 23 biological replicates, FDR: 5 %, s0: 0.1, 250 randomizations)

Statistical analysis revealed a high number of differentially expressed proteins. Due to the high number of statistically significant deregulated proteins, we employed pathway analysis using the “Proteins with Values” search function on the String functional protein

database (FDR stringency: high (1 %)). The functional enrichment analysis revealed “Ribosome” (proteins marked light red in Figure 26, Appendix Figure 41), “DNA replication” (proteins marked in purple in Figure 26, Appendix Figure 42), as well as “L-proline biosynthetic process” and “peptidyl-proline hydroxylation” (proteins marked in orange in Figure 26, Appendix Figure 43) to be upregulated in tumors compared to NTA tissue. Some pathways were found to be lower in tumors, including “PPAR signaling” (proteins marked green in Figure 26, Appendix Figure 44), “triglyceride catabolic pathway” (Appendix Figure 45) and “fatty acid degradation (Appendix Figure 46).

These pathway analyses indicate that tumors display elevated proliferation, as observed from increased DNA replication proteins as well as ribosomal proteins, which are involved in protein synthesis. More surprising, however, are the striking changes in proteins associated with PPAR signaling, including TG and FA catabolic pathways. These changes, however, are concomitant with our findings of changes in the lipidome, and overall suggest deregulated lipid hydrolysis. While some lipases (dark blue) are elevated in tumors, including phospholipase PLA2G4A and alpha beta hydrolase domain containing 11 (ABHD11) and 12 (ABHD12), several lipases are significantly lower in the tumors (Figure 26). This finding is concomitant with our previously observed changes in gene expression and changes in the lipidome. Although neither HSL, nor ATGL or its coregulators were identified in this proteomics analysis, we found that MGL expression was also lower on a protein level. Among the other lipases that were significantly lower expressed in the lung tumors are ABDH14B, epoxide hydrolases 1 (EPHX1) and 2 (EPHX2), carboxylesterase 1 (CES1), LIPA and neutral cholesterol esterase 1 (NCEH1). Taken together, these findings in combination with the observed changes in the lipidome and gene expression point towards deregulation of lipid hydrolysis in lung tumors.

8.4 Activity-based proteomic profiling reveals reduction of lipid hydrolase activity levels in lung tumors

Although the analysis of the proteome of lung tumor and NTA tissues revealed some changes in lipase abundance, we aimed to employ activity-based proteomic profiling (ABPP)

to identify the activities of important lipases by targeting serine hydrolases in fresh tissue immediately after its excision, through incubation with a small serine hydrolase-directed activity-based probe (ABP) (Figure 21A). By employing this serine hydrolase-directed ABP, which is covalently bound only by active enzymes, and subsequent enrichment of these bound proteins prior to label-free quantitative proteomics, the resulting protein abundance (LFQ intensity) corresponds to enzyme activity.

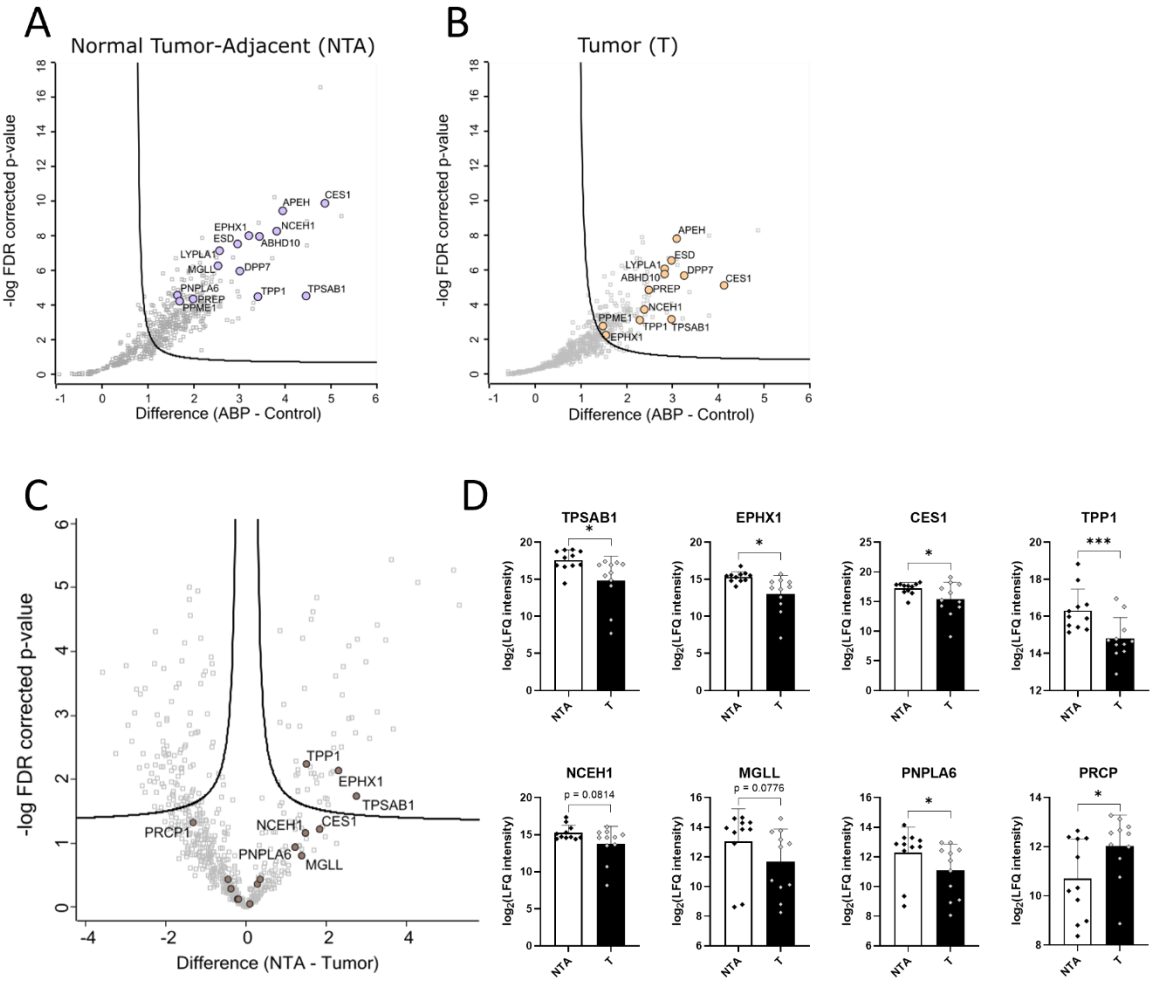

Figure 27: activity-based proteomic profiling of paired Tumor (T) and Normal Tumor-Adjacent (NTA) tissue from NSCLC patients. A: one-sided volcano plot of NTA ABP versus NTA Control samples (FDR: 0.01 %, s0: 0.1, 250 randomizations), serine hydrolases (enriched in NTA ABP samples) marked in light purple; one-sided volcano plot of Tumor ABP versus Tumor Control samples (FDR: 0.01 %, s0: 0.1, 250 randomizations), serine hydrolases

(enriched in Tumor ABP samples) marked in light orange; C: volcano plot of NTA versus T samples (ABP only) (FDR: 0.05 %, s0: 0.1, 250 randomizations), serine hydrolases marked in brown; D: activity of selected serine hydrolases represented as log2(LFQ intensities), (n = 23 biological replicates, paired t-tests, * $p < 0.05$, ** $p < 0.01$, *** $p < 0.001$)

We first checked for serine hydrolase enrichment in ABP-treated samples by comparing Control (no probe treatment) with ABP samples within each group (NTA or Tumor). Several serine hydrolases, including some lipases, were identified through this method in both NTA tissue (Figure 27A, enriched serine hydrolases shown in light purple, histograms in Appendix Figure 47) as well as Tumor tissue (Figure 27B, enriched serine hydrolases shown in light orange, histograms in Appendix Figure 47).

Furthermore, the abundances (log2LFQ intensities) of proteins, which in ABPP correspond to activities, were compared between NTA tissue and Tumors by two-sample t-test. The resulting volcano plot is shown in Figure 27C and histograms are shown in Appendix Figure 48. There were a few non-lipase serine hydrolases with changed activity in lung tumors. These included the neutral protease TPSAB1 and lysosomal protease TPP1 (higher in NTA), as well as PRCP, a lysosomal peptidase (higher in tumors) (Figure 27C and 27D). More interestingly, however, all the identified lipases showed decreased activity in tumors (Figure 27C). Among them was MGL, which provides further evidence for impaired MG hydrolysis in lung tumors (Figure 27C and 27D). Some of the enzymes that were identified in the proteomics experiment were also identified in the ABPP data, and all of them were found to be lower in tumors at the enzyme activity level. These include CES1, PNPLA6, EPHX1 and NCEH1 (Figure 27C and 27D). Overall, these data provide evidence that not only the expression of some lipases is altered in lung tumors, but also their activity is lower.

Taken together, our multifaceted approach allowed us to identify changes in gene expression that align with changes in the proteome as well as changes in the activity of some enzymes, and finally some of these changes were corroborated by changes in levels of certain lipids.

9 Discussion

"Omics" technologies, including genomics, transcriptomics, proteomics and metabolomics have revolutionized clinical research by enabling the detection of vast numbers of genes, transcripts, proteins or metabolites all at once (199). Through technological advances in recent years and decades, these approaches have become faster, more robust, and thus more applicable in the biomedical field. Whole genome information of most types of cancers are nowadays readily available in large repositories like the Cancer Genome Atlas (TCGA) database. However, a gene's function is reliant on the existence of functional proteins. This insight has spurred a growing need for an integration of functional genomics with detailed protein-level investigation, leading to the increasing prominence of proteomics.

About a decade ago, the Clinical Proteomic Tumor Analysis Consortium was established with the goal to generate comprehensive quantitative proteomics data to better understand the molecular basis of cancer. Until now this effort generated data across 11 primary sites of cancer and includes two large-scale lung proteogenomic studies, one study on lung adenocarcinoma (193), and one on lung squamous cell carcinoma (194). Although these data are an important addition to better understand cancer, some aspects of tumors, like the enzymatic activities of some classes of enzymes (i.e., lipases that are strongly regulated at the post-translational level) or the metabolic status are not captured by those methods and require additional techniques.

Previous studies from our lab and others suggest the deregulation of lipolysis to play a role in lung cancer (1, 152, 154), and we hypothesize that lipid hydrolysis is changed in tumors of the lung. Although we have thoroughly investigated some lipolytic enzymes in the context of lung cancer cell lines by conventional cell culture techniques, as well as more *in-vivo*-like techniques like 3D cell culture and CAM assay, we have not investigated lipid hydrolysis in an *in-vivo* model. Therefore, the second part of this thesis aims to explore lipid hydrolases in lung cancer within an *in-vivo* human context. Through analysis of tumor and normal tumor-adjacent (NTA) samples from NSCLC patients, we aim to uncover potential deregulation in lipid hydrolysis pathways in tumors within the tumor microenvironment. To understand these mechanisms comprehensively, a multifaceted approach was adopted,

combining gene expression analyses, lipidomics, and (activity-based) proteomics techniques.

Our data revealed that tumors of NSCLC patients already show altered lipid hydrolysis at a gene expression level. While the expression of the genes encoding for ATGL (*PNPLA2*) and HSL (*LIPE*) were unchanged, *MGLL* expression was lower in tumors. Moreover, the gene expression of the ATGL inhibitory protein HILPDA (*HIG2*), was increased in tumors, while the gene encoding for the major ATGL activator CGI-58 (ABHD5) was lower in tumors, overall suggesting downregulated ATGL activity in tumors.

Lipidomic analyses unveiled alterations in the lipid profiles, notably indicating changes in specific lipid species between tumor and NTA tissues. Variations in triglycerides (TG), diglycerides (DG) and monoglycerides (MG) hinted at decreased TG and MG hydrolysis activities within tumors. Sphingomyelins and ceramides also exhibited significant changes, possibly linked to altered sphingomyelinase activity. The changes observed in TGs indicate heightened levels of lipid droplets, which is an observed phenotype of cancer in solid tumors and is also upregulated upon hypoxia (99, 122, 139). Moreover, the pattern of TGs in tumors was different from that in NTA tissues, with significantly higher levels of TGs with longer overall chain length in tumors (Figure 25).

Proteomic investigations of tumors and NTA tissue highlight several differentially expressed proteins and pathways. In particular, we found elevated DNA replication and ribosomal protein levels in tumors, implying heightened cellular proliferation. These alterations were accompanied by changes in proteins associated with lipid catabolic pathways (lower expression in tumors), suggesting potential disruptions in lipid metabolism in the lung tumors. Strikingly, the majority of proteins associated with PPAR signaling, including many lipid metabolism proteins, were found to be decreased in tumors (Figure 26). Additionally, varied expression of several lipases suggests a collective decrease in lipase activity in lung tumors.

As previously mentioned, protein abundance does not readily reflect protein activity, especially for proteins regulated through post-translational mechanisms like phosphorylation or coregulators. Especially for this purpose, we employed serine hydrolases-directed activity-based proteomic profiling (ABPP), which enables the detection

of lipid hydrolase activities. While our ABPP dataset did not include all of the lipases that were detected in our proteomics dataset, the lipases that were detected (and thus were active) were exclusively lower active in tumors compared to paired NTA tissue. This further corroborates the findings from gene expression analysis, lipidomics as well as proteomics analysis.

It has to be noted, that one limitation of this study is the lack of spatial/cell specific information because all analyses were performed on bulk tissue. To address this problem, immunofluorescent staining of paired tissue samples from NSCLC patients will be performed to show the distribution of lipid droplets (through staining of PLIN2) as well as of a number of lipases (MGL, ATGL) within different cells that are found in the tissue (e.g., tumor cells vs. immune cells).

Taken together, the effectively integrated diverse analytical methods provide a comprehensive understanding of lipid hydrolysis deregulation in lung tumors. The findings collectively imply significant alterations in the expression and activity of critical lipid hydrolases, supporting the hypothesis that lipid hydrolysis pathways are perturbed within lung tumors. The study underscores the importance of investigating lipid metabolism comprehensively in understanding the complexities of cancer progression and highlights some lipid hydrolases that can be further explored in the context of lung cancer in future investigations.

10 Bibliography

1. Honeder S, Tomin T, Nebel L, Gindlhuber J, Fritz-Wallace K, Schinagl M, et al. Adipose Triglyceride Lipase Loss Promotes a Metabolic Switch in A549 Non-Small Cell Lung Cancer Cell Spheroids. Mol Cell Proteomics. 2021;20:100095.
2. Honeder SE, Tomin T, Schinagl M, Pfleger R, Hoehlschen J, Darnhofer B, et al. Research Advances Through Activity-Based Lipid Hydrolase Profiling. Israel Journal of Chemistry. 2023;63(3-4).
3. Tomin T, Schittmayer M, Honeder S, Heininger C, Birner-Gruenberger R. Irreversible oxidative post-translational modifications in heart disease. Expert Rev Proteomics. 2019;16(8):681-93.
4. Schittmayer M, Vujic N, Darnhofer B, Korbelius M, Honeder S, Kratky D, et al. Spatially Resolved Activity-based Proteomic Profiles of the Murine Small Intestinal Lipases. Mol Cell Proteomics. 2020;19(12):2104-15.
5. Schinagl M, Tomin T, Gindlhuber J, Honeder S, Pfleger R, Schittmayer M, et al. Proteomic Changes of Activated Hepatic Stellate Cells. Int J Mol Sci. 2021;22(23).
6. Tomin T, Schittmayer M, Sedej S, Bugger H, Gollmer J, Honeder S, et al. Mass Spectrometry-Based Redox and Protein Profiling of Failing Human Hearts. Int J Mol Sci. 2021;22(4).
7. Waldherr L, Seitanidou M, Jakesova M, Handl V, Honeder S, Nowakowska M, et al. Targeted Chemotherapy of Glioblastoma Spheroids with an Iontronic Pump. Adv Mater Technol. 2021;6(5):2001302.
8. Bradic I, Kuentzel KB, Honeder S, Grabner GF, Vujic N, Zimmermann R, et al. Off-target effects of the lysosomal acid lipase inhibitors Lalistat-1 and Lalistat-2 on neutral lipid hydrolases. Mol Metab. 2022;61:101510.
9. Abbott KL, Ali A, Casalena D, Do BT, Ferreira R, Cheah JH, et al. Screening in serum-derived medium reveals differential response to compounds targeting metabolism. Cell Chem Biol. 2023;30(9):1156-68 e7.
10. Sung H, Ferlay J, Siegel RL, Laversanne M, Soerjomataram I, Jemal A, et al. Global Cancer Statistics 2020: GLOBOCAN Estimates of Incidence and Mortality Worldwide for 36 Cancers in 185 Countries. CA Cancer J Clin. 2021;71(3):209-49.
11. World Population Prospects 2022: Summary of Results. United Nations Department of Economic and Social Affairs, Population Division; 2022.
12. Network GBoDC. Global Burden of Disease Study 2019 (GBD 2019) Results. In: (IHME) IfHMaE, editor. Seattle, United States2021.
13. King RJB, Robins MW. Cancer Biology. 3rd edition ed: Pearson Education Limited; 2006. 311 p.
14. Cooper GM. The Cell: A Molecular Approach. 2nd edition ed: Sunderland (MA): Sinauer Associates; 2000.
15. Hanahan D, Weinberg RA. The hallmarks of cancer. Cell. 2000;100(1):57-70.
16. Hanahan D, Weinberg RA. Hallmarks of cancer: the next generation. Cell. 2011;144(5):646-74.
17. Hanahan D. Hallmarks of Cancer: New Dimensions. Cancer Discov. 2022;12(1):31-46.

18. Herold G. Innere Medizin. Köln: Herold, Gerd; 2024. 1003 p.

19. Makinoshima H, Takita M, Matsumoto S, Yagishita A, Owada S, Esumi H, et al. Epidermal growth factor receptor (EGFR) signaling regulates global metabolic pathways in EGFR-mutated lung adenocarcinoma. J Biol Chem. 2014;289(30):20813-23.

20. Muller PA, Vousden KH. Mutant p53 in cancer: new functions and therapeutic opportunities. Cancer Cell. 2014;25(3):304-17.

21. Schwartz AM, Rezaei MK. Lung Cancer. Clinical Respiratory Medicine2012. p. 776-87.

22. Cox AD, Fesik SW, Kimmelman AC, Luo J, Der CJ. Drugging the undruggable RAS: Mission possible? Nat Rev Drug Discov. 2014;13(11):828-51.

23. Micucci C, Orciari S, Catalano A. Hyperglycemia promotes K-Ras-induced lung tumorigenesis through BASCs amplification. PLoS One. 2014;9(8):e105550.

24. Forbes SA, Beare D, Bindal N, Bamford S, Ward S, Cole CG, et al. COSMIC: High-Resolution Cancer Genetics Using the Catalogue of Somatic Mutations in Cancer. Curr Protoc Hum Genet. 2016;91:10 1 1- 1 37.

25. DeBerardinis RJ, Lum JJ, Hatzivassiliou G, Thompson CB. The biology of cancer: metabolic reprogramming fuels cell growth and proliferation. Cell Metab. 2008;7(1):11-20.

26. Brunner JS, Finley LWS. Metabolic determinants of tumour initiation. Nat Rev Endocrinol. 2023;19(3):134-50.

27. Castell F, Cook GJ. Quantitative techniques in 18FDG PET scanning in oncology. Br J Cancer. 2008;98(10):1597-601.

28. Warburg O, Posener K, Negelein E. Über den Stoffwechsel der Carcinomzelle. Naturwissenschaften. 1924;12:7.

29. Weinhouse S. On respiratory impairment in cancer cells. Science. 1956;124(3215):267-9.

30. Vander Heiden MG, Cantley LC, Thompson CB. Understanding the Warburg Effect: The Metabolic Requirements of Cell Proliferation. Science. 2009;324:5.

31. Ancey PB, Contat C, Meylan E. Glucose transporters in cancer - from tumor cells to the tumor microenvironment. FEBS J. 2018;285(16):2926-43.

32. Hay N. Reprogramming glucose metabolism in cancer: can it be exploited for cancer therapy? Nat Rev Cancer. 2016;16(10):635-49.

33. Yun JY, Rago C, Cheong I, Pagliarini R, Angenendt P, Rajagopalan H, et al. Glucose Deprivation Contributes to the Development of Pathway Mutations in Tumor Cells. Science. 2009;325(5947):1555-9.

34. Kawauchi K, Araki K, Tobiume K, Tanaka N. p53 regulates glucose metabolism through an IKK-NF-kappaB pathway and inhibits cell transformation. Nat Cell Biol. 2008;10(5):611-8.

35. Schwartzenberg-Bar-Yoseph F, Armoni M, Karnieli E. The tumor suppressor p53 down-regulates glucose transporters GLUT1 and GLUT4 gene expression. Cancer Res. 2004;64(7):2627-33.

36. Zhang C, Liu J, Liang Y, Wu R, Zhao Y, Hong X, et al. Tumour-associated mutant p53 drives the Warburg effect. Nat Commun. 2013;4:2935.

37. Hirschey MD, DeBerardinis RJ, Diehl AME, Drew JE, Frezza C, Green MF, et al. Dysregulated metabolism contributes to oncogenesis. Semin Cancer Biol. 2015;35 Suppl:S129-S50.

38. Counihan JL, Grossman EA, Nomura DK. Cancer Metabolism: Current Understanding and Therapies. Chem Rev. 2018;118(14):6893-923.

39. Mathupala SP, Ko YH, Pedersen PL. Hexokinase-2 bound to mitochondria: cancer's stygian link to the "Warburg Effect" and a pivotal target for effective therapy. Semin Cancer Biol. 2009;19(1):17-24.

40. Bustamante E, Pedersen PL. High aerobic glycolysis of rat hepatoma cells in culture: role of mitochondrial hexokinase. Proc Natl Acad Sci U S A. 1977;74(9):3735-9.

41. Nakashima RA, Mangan PS, Colombini M, Pedersen PL. Hexokinase receptor complex in hepatoma mitochondria: evidence from N,N'-dicyclohexylcarbodiimide-labeling studies for the involvement of the pore-forming protein VDAC. Biochemistry. 1986;25(5):1015-21.

42. Van Schaftingen E, Jett MF, Hue L, Hers HG. Control of liver 6-phosphofructokinase by fructose 2,6-bisphosphate and other effectors. Proc Natl Acad Sci U S A. 1981;78(6):3483-6.

43. Yalcin A, Telang S, Clem B, Chesney J. Regulation of glucose metabolism by 6-phosphofructo-2-kinase/fructose-2,6-bisphosphatases in cancer. Exp Mol Pathol. 2009;86(3):174-9.

44. Atsumi T, Chesney J, Metz C, Leng L, Donnelly S, Makita Z, et al. High expression of inducible 6-phosphofructo-2-kinase/fructose-2,6-bisphosphatase (iPFK-2; PFKFB3) in human cancers. Cancer Res. 2002;62(20):5881-7.

45. Chesney J, Mitchell R, Benigni F, Bacher M, Spiegel L, Al-Abed Y, et al. An inducible gene product for 6-phosphofructo-2-kinase with an AU-rich instability element: role in tumor cell glycolysis and the Warburg effect. Proc Natl Acad Sci U S A. 1999;96(6):3047-52.

46. Mazurek S, Boschek CB, Hugo F, Eigenbrodt E. Pyruvate kinase type M2 and its role in tumor growth and spreading. Semin Cancer Biol. 2005;15(4):300-8.

47. Bluemlein K, Gruning NM, Feichtinger RG, Lehrach H, Kofler B, Ralser M. No evidence for a shift in pyruvate kinase PKM1 to PKM2 expression during tumorigenesis. Oncotarget. 2011;2(5):393-400.

48. Mazurek S. Pyruvate kinase type M2: a key regulator of the metabolic budget system in tumor cells. Int J Biochem Cell Biol. 2011;43(7):969-80.

49. Anastasiou D, Poulogiannis G, Asara JM, Boxer MB, Jiang JK, Shen M, et al. Inhibition of pyruvate kinase M2 by reactive oxygen species contributes to cellular antioxidant responses. Science. 2011;334(6060):1278-83.

50. Locasale JW. Serine, glycine and one-carbon units: cancer metabolism in full circle. Nat Rev Cancer. 2013;13(8):572-83.

51. Dorneburg C, Fischer M, Barth TFE, Mueller-Klieser W, Hero B, Gecht J, et al. LDHA in Neuroblastoma Is Associated with Poor Outcome and Its Depletion Decreases Neuroblastoma Growth Independent of Aerobic Glycolysis. Clin Cancer Res. 2018;24(22):5772-83.

52. Feng Y, Xiong Y, Qiao T, Li X, Jia L, Han Y. Lactate dehydrogenase A: A key player in carcinogenesis and potential target in cancer therapy. Cancer Med. 2018;7(12):6124-36.

53. Hirschhaeuser F, Sattler UG, Mueller-Klieser W. Lactate: a metabolic key player in cancer. Cancer Res. 2011;71(22):6921-5.

54. Yao F, Zhao T, Zhong C, Zhu J, Zhao H. LDHA is necessary for the tumorigenicity of esophageal squamous cell carcinoma. Tumour Biol. 2013;34(1):25-31.

55. McFate T, Mohyeldin A, Lu H, Thakar J, Henriques J, Halim ND, et al. Pyruvate dehydrogenase complex activity controls metabolic and malignant phenotype in cancer cells. J Biol Chem. 2008;283(33):22700-8.

56. Owen OE, Kalhan SC, Hanson RW. The key role of anaplerosis and cataplerosis for citric acid cycle function. J Biol Chem. 2002;277(34):30409-12.

57. Hatzivassiliou G, Zhao F, Bauer DE, Andreadis C, Shaw AN, Dhanak D, et al. ATP citrate lyase inhibition can suppress tumor cell growth. Cancer Cell. 2005;8(4):311-21.

58. Mullen AR, DeBerardinis RJ. Genetically-defined metabolic reprogramming in cancer. Trends Endocrinol Metab. 2012;23(11):552-9.

59. Dang L, White DW, Gross S, Bennett BD, Bittinger MA, Driggers EM, et al. Cancer-associated IDH1 mutations produce 2-hydroxyglutarate. Nature. 2009;462(7274):739-44.

60. Wise DR, Ward PS, Shay JE, Cross JR, Gruber JJ, Sachdeva UM, et al. Hypoxia promotes isocitrate dehydrogenase-dependent carboxylation of alpha-ketoglutarate to citrate to support cell growth and viability. Proc Natl Acad Sci U S A. 2011;108(49):19611-6.

61. DeBerardinis RJ, Chandel NS. Fundamentals of cancer metabolism. Sci Adv. 2016;2(5):e1600200.

62. Frieden C. Glutamate Dehydrogenase: V. The Relation of Enzyme Structure to the Catalytic Function. Journal of Biological Chemistry. 1963;238(10):3286-99.

63. Brunner JS, Finley LWS. SnapShot: Cancer metabolism. Mol Cell. 2021;81(18):3878- e1.

64. Inigo M, Deja S, Burgess SC. Ins and Outs of the TCA Cycle: The Central Role of Anaplerosis. Annu Rev Nutr. 2021;41:19-47.

65. Wise DR, Thompson CB. Glutamine addiction: a new therapeutic target in cancer. Trends Biochem Sci. 2010;35(8):427-33.

66. Das SK, Lewis BA, Levens D. MYC: a complex problem. Trends Cell Biol. 2023;33(3):235-46.

67. Eales KL, Hollinshead KE, Tennant DA. Hypoxia and metabolic adaptation of cancer cells. Oncogenesis. 2016;5(1):e190.

68. Wise DR, DeBerardinis RJ, Mancuso A, Sayed N, Zhang XY, Pfeiffer HK, et al. Myc regulates a transcriptional program that stimulates mitochondrial glutaminolysis and leads to glutamine addiction. Proc Natl Acad Sci U S A. 2008;105(48):18782-7.

69. Reitzer LJ, Wice BM, Kennell D. Evidence that glutamine, not sugar, is the major energy source for cultured HeLa cells. Journal of Biological Chemistry. 1979;254(8):2669-76.

70. Ahn CS, Metallo CM. Mitochondria as biosynthetic factories for cancer proliferation. Cancer Metab. 2015;3(1):1.

71. DeBerardinis RJ, Cheng T. Q's next: the diverse functions of glutamine in metabolism, cell biology and cancer. Oncogene. 2010;29(3):313-24.

72. DeBerardinis RJ, Mancuso A, Daikhin E, Nissim I, Yudkoff M, Wehrli S, et al. Beyond aerobic glycolysis: transformed cells can engage in glutamine metabolism that exceeds the requirement for protein and nucleotide synthesis. Proc Natl Acad Sci U S A. 2007;104(49):19345-50.

73. Medes G, Thomas A, Weinhouse S. Metabolism of neoplastic tissue. IV. A study of lipid synthesis in neoplastic tissue slices in vitro. Cancer Res. 1953;13(1):27-9.

74. Ookhtens M, Kannan R, Lyon I, Baker N. Liver and adipose tissue contributions to newly formed fatty acids in an ascites tumor. Am J Physiol. 1984;247(1 Pt 2):R146-53.

75. Currie E, Schulze A, Zechner R, Walther TC, Farese RV, Jr. Cellular fatty acid metabolism and cancer. Cell Metab. 2013;18(2):153-61.

76. Guertin DA, Wellen KE. Acetyl-CoA metabolism in cancer. Nat Rev Cancer. 2023;23(3):156-72.

77. Koundouros N, Poulogiannis G. Reprogramming of fatty acid metabolism in cancer. Br J Cancer. 2020;122(1):4-22.

78. Mashima T, Seimiya H, Tsuruo T. De novo fatty-acid synthesis and related pathways as molecular targets for cancer therapy. Br J Cancer. 2009;100(9):1369-72.

79. Menendez JA, Lupu R. Fatty acid synthase and the lipogenic phenotype in cancer pathogenesis. Nat Rev Cancer. 2007;7(10):763-77.

80. Lien EC, Westermark AM, Zhang Y, Yuan C, Li Z, Lau AN, et al. Low glycaemic diets alter lipid metabolism to influence tumour growth. Nature. 2021;599(7884):302-7.

81. Igal RA. Stearoyl-CoA desaturase-1: a novel key player in the mechanisms of cell proliferation, programmed cell death and transformation to cancer. Carcinogenesis. 2010;31(9):1509-15.

82. Kamphorst JJ, Cross JR, Fan J, de Stanchina E, Mathew R, White EP, et al. Hypoxic and Ras-transformed cells support growth by scavenging unsaturated fatty acids from lysophospholipids. Proc Natl Acad Sci U S A. 2013;110(22):8882-7.

83. Wymann MP, Schneiter R. Lipid signalling in disease. Nat Rev Mol Cell Biol. 2008;9(2):162-76.

84. Takeuchi K, Reue K. Biochemistry, physiology, and genetics of GPAT, AGPAT, and lipin enzymes in triglyceride synthesis. Am J Physiol Endocrinol Metab. 2009;296(6):E1195-209.

85. Carracedo A, Cantley LC, Pandolfi PP. Cancer metabolism: fatty acid oxidation in the limelight. Nat Rev Cancer. 2013;13(4):227-32.

86. Pucci S, Zonetti MJ, Fisco T, Polidoro C, Bocchinfuso G, Palleschi A, et al. Carnitine palmitoyl transferase-1A (CPT1A): a new tumor specific target in human breast cancer. Oncotarget. 2016;7(15):19982-96.

87. Sadeghi RN, Karami-Tehrani F, Salami S. Targeting prostate cancer cell metabolism: impact of hexokinase and CPT-1 enzymes. Tumour Biol. 2015;36(4):2893-905.

88. Ricciardi MR, Mirabilii S, Allegretti M, Licchetta R, Calarco A, Torrisi MR, et al. Targeting the leukemia cell metabolism by the CPT1a inhibition: functional preclinical effects in leukemias. Blood. 2015;126(16):1925-9.

89. Fado R, Zagmutt S, Herrero L, Muley H, Rodriguez-Rodriguez R, Bi H, et al. To be or not to be a fat burner, that is the question for cpt1c in cancer cells. Cell Death Dis. 2023;14(1):57.

90. Schafer ZT, Grassian AR, Song L, Jiang Z, Gerhart-Hines Z, Irie HY, et al. Antioxidant and oncogene rescue of metabolic defects caused by loss of matrix attachment. Nature. 2009;461(7260):109-13.

91. Kaelin WG, Jr., Ratcliffe PJ. Oxygen sensing by metazoans: the central role of the HIF hydroxylase pathway. Mol Cell. 2008;30(4):393-402.

92. Marin-Hernandez A, Gallardo-Perez JC, Ralph SJ, Rodriguez-Enriquez S, Moreno-Sanchez R. HIF-1alpha modulates energy metabolism in cancer cells by inducing over-expression of specific glycolytic isoforms. Mini Rev Med Chem. 2009;9(9):1084-101.

93. Semenza GL. Targeting HIF-1 for cancer therapy. Nat Rev Cancer. 2003;3(10):721-32.

94. Minchenko A, Leshchinsky I, Opentanova I, Sang N, Srinivas V, Armstead V, et al. Hypoxia-inducible factor-1-mediated expression of the 6-phosphofructo-2-kinase/fructose-2,6-bisphosphatase-3 (PFKFB3) gene. Its possible role in the Warburg effect. J Biol Chem. 2002;277(8):6183-7.

95. Semenza GL, Jiang BH, Leung SW, Passantino R, Concordet JP, Maire P, et al. Hypoxia response elements in the aldolase A, enolase 1, and lactate dehydrogenase A gene promoters contain essential binding sites for hypoxia-inducible factor 1. J Biol Chem. 1996;271(51):32529-37.

96. Wigfield SM, Winter SC, Giatromanolaki A, Taylor J, Koukourakis ML, Harris AL. PDK-1 regulates lactate production in hypoxia and is associated with poor prognosis in head and neck squamous cancer. Br J Cancer. 2008;98(12):1975-84.

97. Kamphorst JJ, Chung MK, Fan J, Rabinowitz JD. Quantitative analysis of acetyl-CoA production in hypoxic cancer cells reveals substantial contribution from acetate. Cancer Metab. 2014;2:23.

98. Schug ZT, Peck B, Jones DT, Zhang Q, Grosskurth S, Alam IS, et al. Acetyl-CoA synthetase 2 promotes acetate utilization and maintains cancer cell growth under metabolic stress. Cancer Cell. 2015;27(1):57-71.

99. Bensaad K, Favaro E, Lewis CA, Peck B, Lord S, Collins JM, et al. Fatty acid uptake and lipid storage induced by HIF-1alpha contribute to cell growth and survival after hypoxia-reoxygenation. Cell Rep. 2014;9(1):349-65.

100. Furuta E, Pai SK, Zhan R, Bandyopadhyay S, Watabe M, Mo YY, et al. Fatty acid synthase gene is up-regulated by hypoxia via activation of Akt and sterol regulatory element binding protein-1. Cancer Res. 2008;68(4):1003-11.

101. Gold V. The IUPAC Compendium of Chemical Terminology2019.

102. Grabner GF, Xie H, Schweiger M, Zechner R. Lipolysis: cellular mechanisms for lipid mobilization from fat stores. Nat Metab. 2021;3(11):1445-65.

103. Schweiger M, Eichmann TO, Taschler U, Zimmermann R, Zechner R, Lass A. Measurement of lipolysis. Methods Enzymol. 2014;538:171-93.

104. Zechner R, Zimmermann R, Eichmann TO, Kohlwein SD, Haemmerle G, Lass A, et al. FAT SIGNALS--lipases and lipolysis in lipid metabolism and signaling. Cell Metab. 2012;15(3):279-91.

105. McDonald AG, Boyce S, Tipton KF. ExplorEnz: the primary source of the IUBMB enzyme list. Nucleic Acids Res. 2009;37(Database issue):D593-7.

106. Long JZ, Cravatt BF. The metabolic serine hydrolases and their functions in mammalian physiology and disease. Chem Rev. 2011;111(10):6022-63.

107. Dodson G, Wlodawer A. Catalytic triads and their relatives. Trends Biochem Sci. 1998;23(9):347-52.

108. Aranda J, Cerqueira NM, Fernandes PA, Roca M, Tunon I, Ramos MJ. The catalytic mechanism of carboxylesterases: a computational study. Biochemistry. 2014;53(36):5820-9.

109. Lass A, Zimmermann R, Oberer M, Zechner R. Lipolysis - a highly regulated multi-enzyme complex mediates the catabolism of cellular fat stores. Prog Lipid Res. 2011;50(1):14-27.

110. Warner TG, Dambach LM, Shin JH, O'Brien JS. Purification of the lysosomal acid lipase from human liver and its role in lysosomal lipid hydrolysis. J Biol Chem. 1981;256(6):2952-7.

111. Zimmermann R, Strauss JG, Haemmerle G, Schoiswohl G, Birner-Gruenberger R, Riederer M, et al. Fat mobilization in adipose tissue is promoted by adipose triglyceride lipase. Science. 2004;306(5700):1383-6.

112. Kienesberger PC, Oberer M, Lass A, Zechner R. Mammalian patatin domain containing proteins: a family with diverse lipolytic activities involved in multiple biological functions. J Lipid Res. 2009;50 Suppl(Suppl):S63-8.

113. Lehner R, Quiroga AD. Fatty Acid Handling in Mammalian Cells. Biochemistry of Lipids, Lipoproteins and Membranes2016. p. 149-84.

114. Eichmann TO, Kumari M, Haas JT, Farese RV, Jr., Zimmermann R, Lass A, et al. Studies on the substrate and stereo/regioselectivity of adipose triglyceride lipase, hormone-sensitive lipase, and diacylglycerol-O-acyltransferases. J Biol Chem. 2012;287(49):41446-57.

115. Yogosawa S, Mizutani S, Ogawa Y, Izumi T. Activin receptor-like kinase 7 suppresses lipolysis to accumulate fat in obesity through downregulation of peroxisome proliferator-activated receptor gamma and C/EBPalpha. Diabetes. 2013;62(1):115-23.

116. Rakhshandehroo M, Sanderson LM, Matilainen M, Stienstra R, Carlberg C, de Groot PJ, et al. Comprehensive analysis of PPARalpha-dependent regulation of hepatic lipid metabolism by expression profiling. PPAR Res. 2007;2007:26839.

117. Chakrabarti P, Kandror KV. FoxO1 controls insulin-dependent adipose triglyceride lipase (ATGL) expression and lipolysis in adipocytes. J Biol Chem. 2009;284(20):13296-300.

118. Lass A, Zimmermann R, Haemmerle G, Riederer M, Schoiswohl G, Schweiger M, et al. Adipose triglyceride lipase-mediated lipolysis of cellular fat stores is activated by CGI-58 and defective in Chanarin-Dorfman Syndrome. Cell Metab. 2006;3(5):309-19.

119. Gandotra S, Le Dour C, Bottomley W, Cervera P, Giral P, Reznik Y, et al. Perilipin deficiency and autosomal dominant partial lipodystrophy. N Engl J Med. 2011;364(8):740-8.

120. Yang A, Mottillo EP, Mladenovic-Lucas L, Zhou L, Granneman JG. Dynamic interactions of ABHD5 with PNPLA3 regulate triacylglycerol metabolism in brown adipocytes. Nat Metab. 2019;1(5):560-9.

121. Yang X, Lu X, Lombes M, Rha GB, Chi YI, Guerin TM, et al. The G(0)/G(1) switch gene 2 regulates adipose lipolysis through association with adipose triglyceride lipase. Cell Metab. 2010;11(3):194-205.

122. Gimm T, Wiese M, Teschemacher B, Deggerich A, Schodel J, Knaup KX, et al. Hypoxia-inducible protein 2 is a novel lipid droplet protein and a specific target gene of hypoxia-inducible factor-1. FASEB J. 2010;24(11):4443-58.

123. Zandbergen F, Mandard S, Escher P, Tan NS, Patsouris D, Jatkoe T, et al. The G0/G1 switch gene 2 is a novel PPAR target gene. Biochem J. 2005;392(Pt 2):313-24.

124. Mattijssen F, Georgiadi A, Andasarie T, Szalowska E, Zota A, Krones-Herzig A, et al. Hypoxia-inducible lipid droplet-associated (HILPDA) is a novel peroxisome proliferator-activated receptor (PPAR) target involved in hepatic triglyceride secretion. J Biol Chem. 2014;289(28):19279-93.

125. Vaughan M, Berger JE, Steinberg D. Hormone-sensitive Lipase and Monoglyceride Lipase Activities in Adipose Tissue. Journal of Biological Chemistry. 1964;239(2):401-9.

126. Lu X, Yang X, Liu J. Differential control of ATGL-mediated lipid droplet degradation by CGI-58 and G0S2. Cell Cycle. 2010;9(14):2719-25.

127. Steinberg D, Huttunen JK. The role of cyclic AMP in activation of hormone-sensitive lipase of adipose tissue. Adv Cyclic Nucleotide Res. 1972;1:47-62.

128. Kimmel AR, Sztalryd C. The Perilipins: Major Cytosolic Lipid Droplet-Associated Proteins and Their Roles in Cellular Lipid Storage, Mobilization, and Systemic Homeostasis. Annual Review of Nutrition, Vol 36. 2016;36:471-509.

129. Yu L, Li Y, Grise A, Wang H. CGI-58: Versatile Regulator of Intracellular Lipid Droplet Homeostasis. Adv Exp Med Biol. 2020;1276:197-222.

130. Tornqvist H, Belfrage P. Purification and Some Properties of a Monoacylglycerol-Hydrolyzing Enzyme of Rat Adipose-Tissue. Journal of Biological Chemistry. 1976;251(3):813-9.

131. Grabner GF, Zimmermann R, Schicho R, Taschler U. Monoglyceride lipase as a drug target: At the crossroads of arachidonic acid metabolism and endocannabinoid signaling. Pharmacol Ther. 2017;175:35-46.

132. Savinainen JR, Kansanen E, Pantsar T, Navia-Paldanius D, Parkkari T, Lehtonen M, et al. Robust hydrolysis of prostaglandin glycerol esters by human monoacylglycerol lipase (MAGL). Mol Pharmacol. 2014;86(5):522-35.

133. Heier C, Taschler U, Radulovic M, Aschauer P, Eichmann TO, Grond S, et al. Monoacylglycerol Lipases Act as Evolutionarily Conserved Regulators of Non-oxidative Ethanol Metabolism. J Biol Chem. 2016;291(22):11865-75.

134. Thomas G, Betters JL, Lord CC, Brown AL, Marshall S, Ferguson D, et al. The serine hydrolase ABHD6 Is a critical regulator of the metabolic syndrome. Cell Rep. 2013;5(2):508-20.

135. Walther TC, Farese RV, Jr. Lipid droplets and cellular lipid metabolism. Annu Rev Biochem. 2012;81:687-714.

136. Buhman KK, Chen HC, Farese RV, Jr. The enzymes of neutral lipid synthesis. J Biol Chem. 2001;276(44):40369-72.

137. Walther TC, Chung J, Farese RV, Jr. Lipid Droplet Biogenesis. Annu Rev Cell Dev Biol. 2017;33:491-510.

138. Kory N, Farese RV, Jr., Walther TC. Targeting Fat: Mechanisms of Protein Localization to Lipid Droplets. Trends Cell Biol. 2016;26(7):535-46.

139. Cruz ALS, Barreto EA, Fazolini NPB, Viola JPB, Bozza PT. Lipid droplets: platforms with multiple functions in cancer hallmarks. Cell Death Dis. 2020;11(2):105.

140. Zoula S, Rijken PF, Peters JP, Farion R, Van der Sanden BP, Van der Kogel AJ, et al. Pimonidazole binding in C6 rat brain glioma: relation with lipid droplet detection. Br J Cancer. 2003;88(9):1439-44.

141. Saarikoski ST, Rivera SP, Hankinson O. Mitogen-inducible gene 6 (MIG-6), adipophilin and tuftelin are inducible by hypoxia. FEBS Lett. 2002;530(1-3):186-90.

142. Ackerman D, Tumanov S, Qiu B, Michalopoulou E, Spata M, Azzam A, et al. Triglycerides Promote Lipid Homeostasis during Hypoxic Stress by Balancing Fatty Acid Saturation. Cell Rep. 2018;24(10):2596-605 e5.

143. Wang D, Dubois RN. Eicosanoids and cancer. Nat Rev Cancer. 2010;10(3):181-93.

144. Finetti F, Travelli C, Ercoli J, Colombo G, Buoso E, Trabalzini L. Prostaglandin E2 and Cancer: Insight into Tumor Progression and Immunity. Biology (Basel). 2020;9(12).

145. Accioly MT, Pacheco P, Maya-Monteiro CM, Carrossini N, Robbs BK, Oliveira SS, et al. Lipid bodies are reservoirs of cyclooxygenase-2 and sites of prostaglandin-E2 synthesis in colon cancer cells. Cancer Res. 2008;68(6):1732-40.

146. Fujimoto T, Kogo H, Ishiguro K, Tauchi K, Nomura R. Caveolin-2 is targeted to lipid droplets, a new "membrane domain" in the cell. J Cell Biol. 2001;152(5):1079-85.

147. Yu W, Cassara J, Weller PF. Phosphatidylinositide 3-kinase localizes to cytoplasmic lipid bodies in human polymorphonuclear leukocytes and other myeloid-derived cells. Blood. 2000;95(3):1078-85.

148. Yu WG, Bozza PT, Tzizik DM, Gray JP, Cassara J, Dvorak AM, et al. Co-compartmentalization of MAP kinases and cytosolic phospholipase A at cytoplasmic arachidonate-rich lipid bodies. Am J Pathol. 1998;152(3):759-69.

149. Fischer J, Lefevre C, Morava E, Mussini JM, Laforet P, Negre-Salvayre A, et al. The gene encoding adipose triglyceride lipase (PNPLA2) is mutated in neutral lipid storage disease with myopathy. Nat Genet. 2007;39(1):28-30.

150. Radner FP, Streith IE, Schoiswohl G, Schweiger M, Kumari M, Eichmann TO, et al. Growth retardation, impaired triacylglycerol catabolism, hepatic steatosis, and lethal skin barrier defect in mice lacking comparative gene identification-58 (CGI-58). J Biol Chem. 2010;285(10):7300-11.

151. Haemmerle G, Moustafa T, Woelkart G, Buttner S, Schmidt A, van de Weijer T, et al. ATGL-mediated fat catabolism regulates cardiac mitochondrial function via PPAR-alpha and PGC-1. Nat Med. 2011;17(9):1076-85.

152. Al-Zoughbi W, Pichler M, Gorkiewicz G, Guertl-Lackner B, Haybaeck J, Jahn SW, et al. Loss of adipose triglyceride lipase is associated with human cancer and induces mouse pulmonary neoplasia. Oncotarget. 2016;7(23):33832-40.

153. Kanti MM, Striessnig-Bina I, Wieser BI, Schauer S, Leitinger G, Eichmann TO, et al. Adipose triglyceride lipase-mediated lipid catabolism is essential for bronchiolar regeneration. JCI Insight. 2022;7(9).

154. Tomin T, Fritz K, Gindlhuber J, Waldherr L, Pucher B, Thallinger GG, et al. Deletion of Adipose Triglyceride Lipase Links Triacylglycerol Accumulation to a More-Aggressive Phenotype in A549 Lung Carcinoma Cells. J Proteome Res. 2018;17(4):1415-25.

155. Xie H, Heier C, Kien B, Vesely PW, Tang Z, Sexl V, et al. Adipose triglyceride lipase activity regulates cancer cell proliferation via AMP-kinase and mTOR signaling. Biochim Biophys Acta Mol Cell Biol Lipids. 2020;1865(9):158737.

156. Ou J, Miao H, Ma Y, Guo F, Deng J, Wei X, et al. Loss of abhd5 promotes colorectal tumor development and progression by inducing aerobic glycolysis and epithelial-mesenchymal transition. Cell Rep. 2014;9(5):1798-811.

157. Chen G, Zhou G, Lotvola A, Granneman JG, Wang J. ABHD5 suppresses cancer cell anabolism through lipolysis-dependent activation of the AMPK/mTORC1 pathway. J Biol Chem. 2021;296:100104.

158. Bombarda-Rocha V, Silva D, Badr-Eddine A, Nogueira P, Goncalves J, Fresco P. Challenges in Pharmacological Intervention in Perilipins (PLINs) to Modulate Lipid Droplet Dynamics in Obesity and Cancer. Cancers (Basel). 2023;15(15).

159. Fujimoto M, Yoshizawa A, Sumiyoshi S, Sonobe M, Menju T, Hirata M, et al. Adipophilin expression in lung adenocarcinoma is associated with apocrine-like features and poor clinical prognosis: an immunohistochemical study of 328 cases. Histopathology. 2017;70(2):232-41.

160. Povero D, Johnson SM, Liu J. Hypoxia, hypoxia-inducible gene 2 (HIG2)/HILPDA, and intracellular lipolysis in cancer. Cancer Lett. 2020;493:71-9.

161. Zagani R, El-Assaad W, Gamache I, Teodoro JG. Inhibition of adipose triglyceride lipase (ATGL) by the putative tumor suppressor G0S2 or a small molecule inhibitor attenuates the growth of cancer cells. Oncotarget. 2015;6(29):28282-95.

162. Vegliante R, Di Leo L, Ciccarone F, Ciriolo MR. Hints on ATGL implications in cancer: beyond bioenergetic clues. Cell Death Dis. 2018;9(3):316.

163. Nomura DK, Long JZ, Niessen S, Hoover HS, Ng SW, Cravatt BF. Monoacylglycerol lipase regulates a fatty acid network that promotes cancer pathogenesis. Cell. 2010;140(1):49-61.

164. Sun H, Jiang L, Luo X, Jin W, He Q, An J, et al. Potential tumor-suppressive role of monoglyceride lipase in human colorectal cancer. Oncogene. 2013;32(2):234-41.

165. Liu R, Wang X, Curtiss C, Landas S, Rong R, Sheikh MS, et al. Monoglyceride lipase gene knockout in mice leads to increased incidence of lung adenocarcinoma. Cell Death Dis. 2018;9(2):36.

166. Hosios AM, Li Z, Lien EC, Heiden MVG. Preparation of Lipid-Stripped Serum for the Study of Lipid Metabolism in Cell Culture. Bio Protoc. 2018;8(11):e2876.

167. Schindelin J, Arganda-Carreras I, Frise E, Kaynig V, Longair M, Pietzsch T, et al. Fiji: an open-source platform for biological-image analysis. Nat Methods. 2012;9(7):676-82.

168. Qiu B, Simon MC. BODIPY 493/503 Staining of Neutral Lipid Droplets for Microscopy and Quantification by Flow Cytometry. Bio Protoc. 2016;6(17).

169. Deryugina EI, Quigley JP. Chapter 2. Chick embryo chorioallantoic membrane models to quantify angiogenesis induced by inflammatory and tumor cells or purified effector molecules. Methods Enzymol. 2008;444:21-41.

170. Adusumilli R, Mallick P. Data Conversion with ProteoWizard msConvert. Methods Mol Biol. 2017;1550:339-68.

171. Agrawal S, Kumar S, Sehgal R, George S, Gupta R, Poddar S, et al. El-MAVEN: A Fast, Robust, and User-Friendly Mass Spectrometry Data Processing Engine for Metabolomics. Methods Mol Biol. 2019;1978:301-21.

172. Heinrich P, Kohler C, Ellmann L, Kuerner P, Spang R, Oefner PJ, et al. Correcting for natural isotope abundance and tracer impurity in MS-, MS/MS- and high-resolution-multiple-tracer-data from stable isotope labeling experiments with IsoCorrectoR. Sci Rep. 2018;8(1):17910.

173. Bache N, Geyer PE, Bekker-Jensen DB, Hoerning O, Falkenby L, Treit PV, et al. A Novel LC System Embeds Analytes in Pre-formed Gradients for Rapid, Ultra-robust Proteomics. Molecular & Cellular Proteomics. 2018;17(11):2284-96.

174. Cox J, Matic I, Hilger M, Nagaraj N, Selbach M, Olsen JV, et al. A practical guide to the MaxQuant computational platform for SILAC-based quantitative proteomics. Nat Protoc. 2009;4(5):698-705.

175. Tyanova S, Temu T, Sinitcyn P, Carlson A, Hein MY, Geiger T, et al. The Perseus computational platform for comprehensive analysis of (prote)omics data. Nat Methods. 2016;13(9):731-40.

176. Perez-Riverol Y, Bai J, Bandla C, Garcia-Seisdedos D, Hewapathirana S, Kamatchinathan S, et al. The PRIDE database resources in 2022: a hub for mass spectrometry-based proteomics evidences. Nucleic Acids Res. 2022;50(D1):D543-D52.

177. Demichev V, Messner CB, Vernardis SI, Lilley KS, Ralser M. DIA-NN: neural networks and interference correction enable deep proteome coverage in high throughput. Nat Methods. 2020;17(1):41-4.

178. Riffle S, Hegde RS. Modeling tumor cell adaptations to hypoxia in multicellular tumor spheroids. J Exp Clin Cancer Res. 2017;36(1):102.

179. Bochman ML, Schwacha A. The Mcm complex: unwinding the mechanism of a replicative helicase. Microbiol Mol Biol Rev. 2009;73(4):652-83.

180. Jagarlamudi KK, Shaw M. Thymidine kinase 1 as a tumor biomarker: technical advances offer new potential to an old biomarker. Biomark Med. 2018;12(9):1035-48.

181. Zhang C, Xu J, Xue S, Ye J. Prognostic Value of L-Type Amino Acid Transporter 1 (LAT1) in Various Cancers: A Meta-Analysis. Mol Diagn Ther. 2020;24(5):523-36.

182. Vriens K, Christen S, Parik S, Broekaert D, Yoshinaga K, Talebi A, et al. Evidence for an alternative fatty acid desaturation pathway increasing cancer plasticity. Nature. 2019;566(7744):403-6.

183. Kim WY, Jang JY, Jeon YK, Chung DH, Kim YG, Kim CW. Syntenin increases the invasiveness of small cell lung cancer cells by activating p38, AKT, focal adhesion kinase and SP1. Exp Mol Med. 2014;46(4):e90.

184. Sun Y, Zhang J, Ma L. alpha-catenin. A tumor suppressor beyond adherens junctions. Cell Cycle. 2014;13(15):2334-9.

185. Bartlett K, Eaton S. Mitochondrial beta-oxidation. Eur J Biochem. 2004;271(3):462-9.

186. Yang C, Zhao Y, Wang L, Guo Z, Ma L, Yang R, et al. De novo pyrimidine biosynthetic complexes support cancer cell proliferation and ferroptosis defence. Nat Cell Biol. 2023;25(6):836-47.

187. Jin Y, Tan Y, Wu J, Ren Z. Lipid droplets: a cellular organelle vital in cancer cells. Cell Death Discovery. 2023;9(1).

188. Di Leo L, Vegliante R, Ciccarone F, Salvatori I, Scimeca M, Bonanno E, et al. Forcing ATGL expression in hepatocarcinoma cells imposes glycolytic rewiring through PPAR-alpha/p300-mediated acetylation of p53. Oncogene. 2019;38(11):1860-75.

189. Rao S, Oyang L, Liang J, Yi P, Han Y, Luo X, et al. Biological Function of HYOU1 in Tumors and Other Diseases. Onco Targets Ther. 2021;14:1727-35.

190. Boukalova S, Hubackova S, Milosevic M, Ezrova Z, Neuzil J, Rohlena J. Dihydroorotate dehydrogenase in oxidative phosphorylation and cancer. Biochim Biophys Acta Mol Basis Dis. 2020;1866(6):165759.

191. Luengo A, Li Z, Gui DY, Sullivan LB, Zagorulya M, Do BT, et al. Increased demand for NAD(+) relative to ATP drives aerobic glycolysis. Mol Cell. 2021;81(4):691-707 e6.

192. Gunawardana Y, Niranjan M. Bridging the gap between transcriptome and proteome measurements identifies post-translationally regulated genes. Bioinformatics. 2013;29(23):3060-6.

193. Gillette MA, Satpathy S, Cao S, Dhanasekaran SM, Vasaikar SV, Krug K, et al. Proteogenomic Characterization Reveals Therapeutic Vulnerabilities in Lung Adenocarcinoma. Cell. 2020;182(1):200-25 e35.

194. Satpathy S, Krug K, Jean Beltran PM, Savage SR, Petralia F, Kumar-Sinha C, et al. A proteogenomic portrait of lung squamous cell carcinoma. Cell. 2021;184(16):4348-71 e40.

195. Hartler J, Trotzmuller M, Chitraju C, Spener F, Kofeler HC, Thallinger GG. Lipid Data Analyzer: unattended identification and quantitation of lipids in LC-MS data. Bioinformatics. 2011;27(4):572-7.

196. Green DR. Apoptosis and sphingomyelin hydrolysis. The flip side. J Cell Biol. 2000;150(1):F5-7.

197. Haimovitz-Friedman A, Kolesnick RN, Fuks Z. Ceramide signaling in apoptosis. Br Med Bull. 1997;53(3):539-53.

198. Liu P, Zhu W, Chen C, Yan B, Zhu L, Chen X, et al. The mechanisms of lysophosphatidylcholine in the development of diseases. Life Sciences. 2020;247.

199. Sajjad W, Rafiq M, Ali B, Hayat M, Zada S, Sajjad W, et al. Proteogenomics: New Emerging Technology. HAYATI Journal of Biosciences. 2016;23(3):97-100.

Appendix

All MS proteomics data reported in this thesis have been deposited to the ProteomeXchange Consortium via the PRIDE (176) with the following dataset identifiers: PXD021105 for 3D spheroid and spheroid on CAM data; PXD046912 for ATGL-KO, MGL-KO and Control in A549, H1299, H358 and H441 NSCLC cell lines; PXD046998 for NSCLC tumor and normal tumor-adjacent tissue DIA shotgun proteomics experiment; and PXD046934 for NSCLC tumor and normal tumor-adjacent tissue ABPP DDA proteomics experiment.

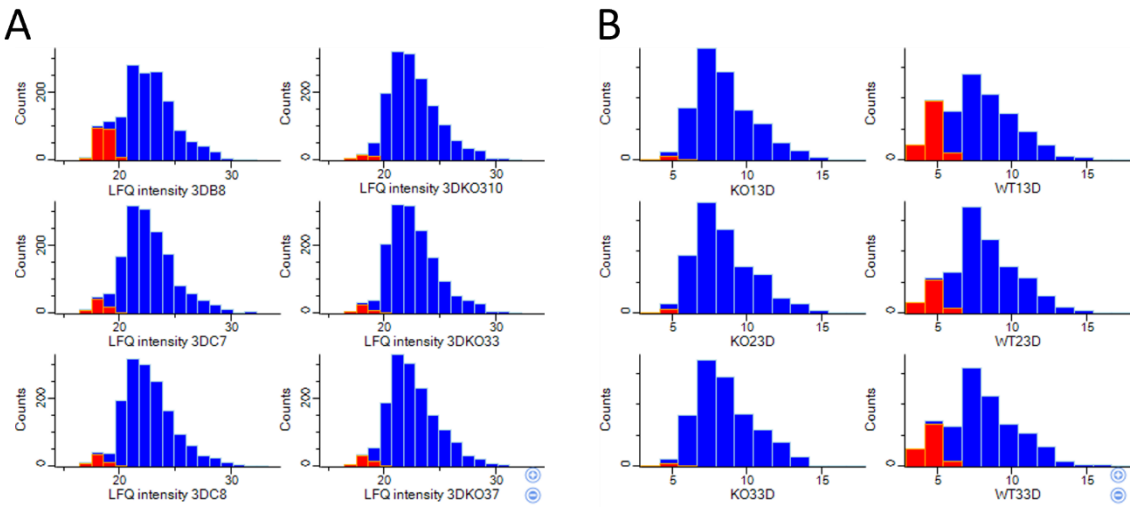

Appendix. Figure 28: histograms of proteomics data. A: 3D spheroids ATGL-KO and Control, proteins were filtered to contain at least 3 valid values in at least one group (ATGL-KO or Control), missing values were then imputed from normal distribution with a downshift of 2 and width of 0.3; B: 3D spheroids on CAM, proteins were filtered to contain at least 3 valid values in at least one group (ATGL-KO or Control), missing values were then imputed from normal distribution with a downshift of 2 and width of 0.3

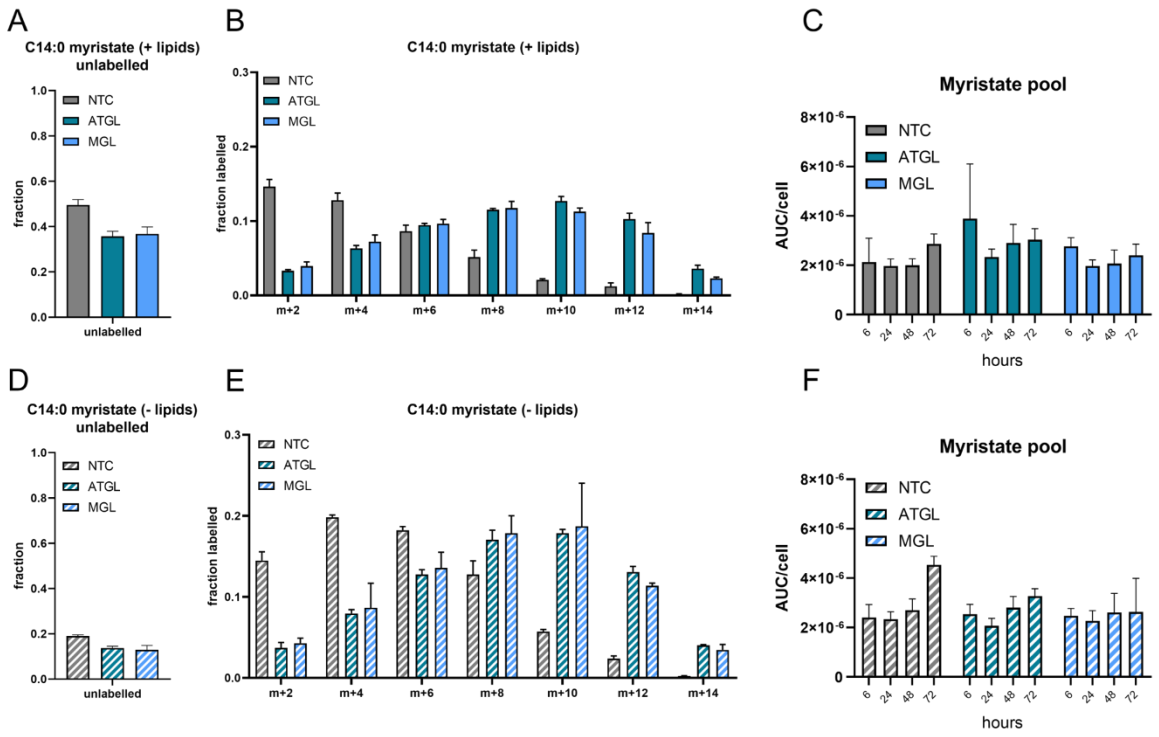

Appendix. Figure 29: metabolic tracing data of uniformly ^{13}C-labelled glucose into myristate in A549 (Cas9) cell lines. A: the fraction of measured myristate containing no ^{13}C-label and thus is not derived from glucose, cells grown in regular (lipid containing) medium; B: distribution of fractions of myristate with increasing amount of ^{13}C-label, cells grown in regular (lipid containing) medium; C: myristate pool at t = 6 h, 24 h, 48 h or 72 h of cells grown in regular (lipid containing) medium; D: the fraction of measured myristate containing no ^{13}C-label and thus is not derived from glucose, cells grown in lipid depleted medium; E: distribution of fractions of myristate with increasing amount of ^{13}C-label; F: myristate pool at t = 6 h, 24 h, 48 h or 72 h of cells grown in lipid depleted medium; G: fractions (A, B, D, E) are shown as unlabelled or m+n, where n corresponds to the number of ^{13}C labels derived from glucose that were incorporated; Cells were cultured in respective media for 72 hours, and metabolite levels were normalized to cell counts as well as an internal standard. Metabolite pools (C, F) were determined by combining the peak areas (AUC) of each fraction of myristate normalized to internal standard and cell counts.

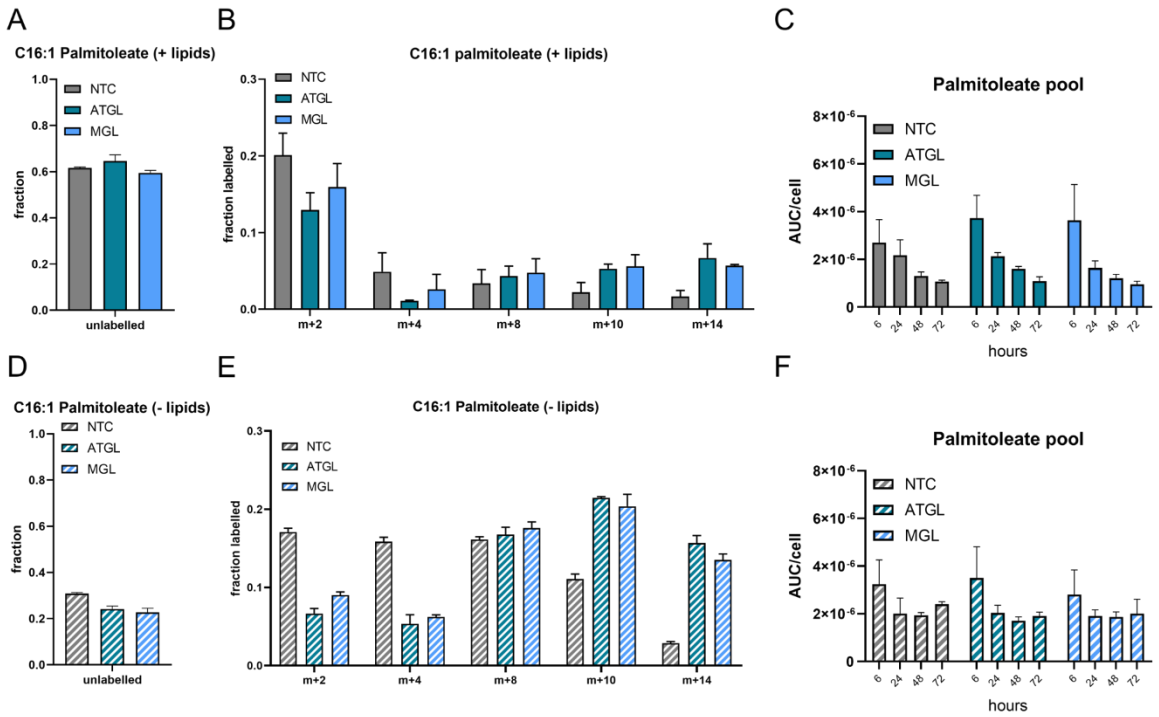

Appendix. Figure 30: metabolic tracing data of uniformly ^{13}C-labelled glucose into palmitoleate in A549 (Cas9) cell lines. A: the fraction of measured palmitoleate containing no ^{13}C-label and thus is not derived from glucose, cells grown in regular (lipid containing) medium; B: distribution of fractions of palmitoleate with increasing amount of ^{13}C-label, cells grown in regular (lipid containing) medium; C: palmitoleate pool at t = 6 h, 24 h, 48 h or 72 h of cells grown in regular (lipid containing) medium; D: the fraction of measured palmitate containing no ^{13}C-label and thus is not derived from glucose, cells grown in lipid depleted medium; E: distribution of fractions of palmitoleate with increasing amount of ^{13}C-label; F: palmitoleate pool at t = 6 h, 24 h, 48 h or 72 h of cells grown in lipid depleted medium; G: fractions (A, B, D, E) are shown as unlabelled or m+n, where n corresponds to the number of ^{13}C labels derived from glucose that were incorporated; Cells were cultured in respective media for 72 hours, and metabolite levels were normalized to cell counts as well as an internal standard. Metabolite pools (C, F) were determined by combining the peak areas (AUC) of each fraction of palmitoleate normalized to internal standard and cell counts.

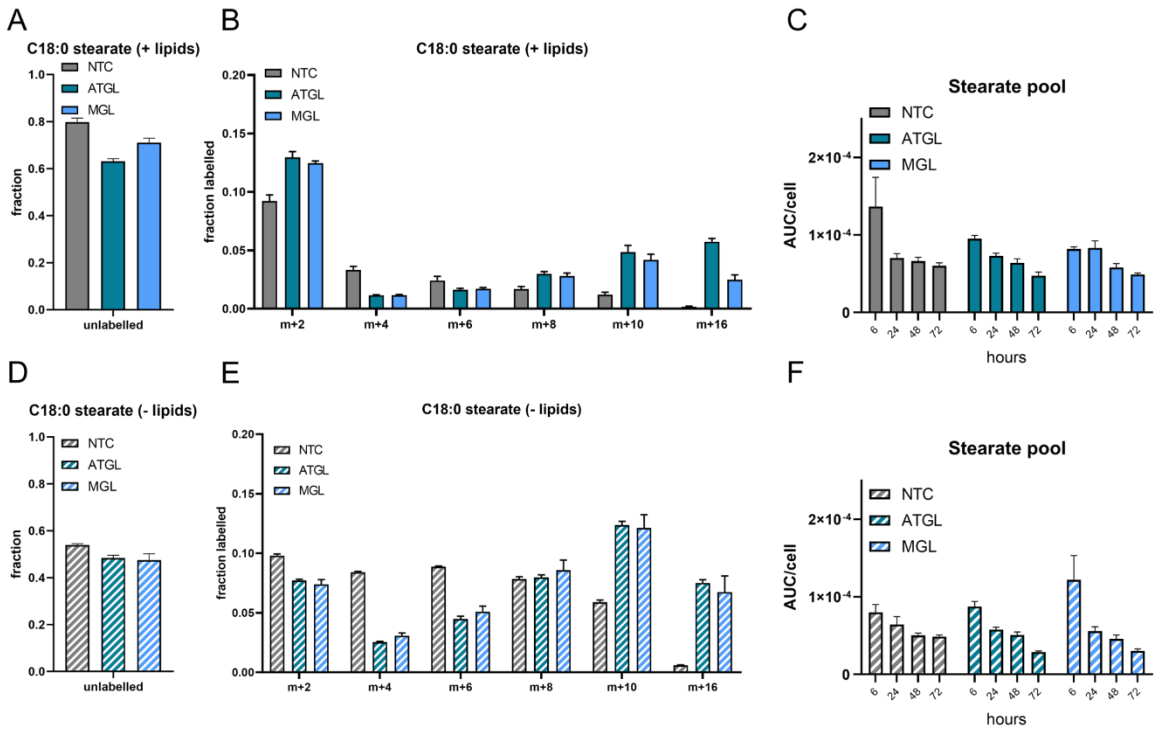

Appendix. Figure 31: metabolic tracing data of uniformly ^{13}C-labelled glucose into stearate in A549 (Cas9) cell lines. A: the fraction of measured stearate containing no ^{13}C-label and thus is not derived from glucose, cells grown in regular (lipid containing) medium; B: distribution of fractions of stearate with increasing amount of ^{13}C-label, cells grown in regular (lipid containing) medium; C: stearate pool at t = 6 h, 24 h, 48 h or 72 h of cells grown in regular (lipid containing) medium; D: the fraction of measured stearate containing no ^{13}C-label and thus is not derived from glucose, cells grown in lipid depleted medium; E: distribution of fractions of stearate with increasing amount of ^{13}C-label; F: stearate pool at t = 6 h, 24 h, 48 h or 72 h of cells grown in lipid depleted medium; G: Fractions (A, B, D, E) are shown as unlabelled or m+n, where n corresponds to the number of ^{13}C labels derived from glucose that were incorporated; Cells were cultured in respective media for 72 hours, and metabolite levels were normalized to cell counts as well as an internal standard. Metabolite pools (C, F) were determined by combining the peak areas (AUC) of each fraction of stearate normalized to internal standard and cell counts

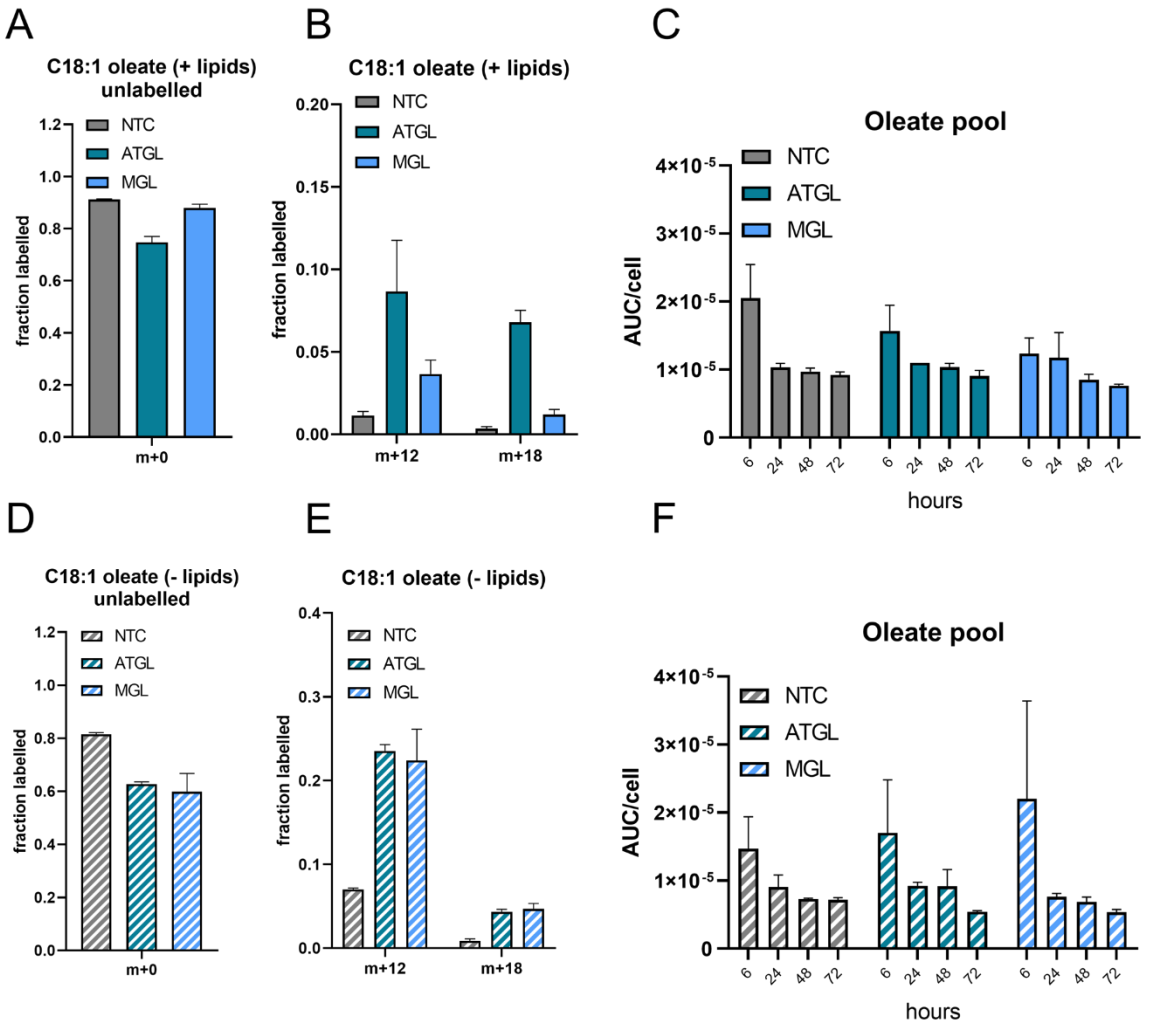

Appendix. Figure 32: metabolic tracing data of uniformly ^{13}C-labelled glucose into oleate in A549 (Cas9) cell lines. A: the fraction of measured oleate containing no ^{13}C-label and thus is not derived from glucose, cells grown in regular (lipid containing) medium; B: distribution of fractions of oleate with increasing amount of ^{13}C-label, cells grown in regular (lipid containing) medium; C: oleate pool at t = 6 h, 24 h, 48 h or 72 h of cells grown in regular (lipid containing) medium; D: the fraction of measured oleate containing no ^{13}C-label and thus is not derived from glucose, cells grown in lipid depleted medium; E: distribution of fractions of oleate with increasing amount of ^{13}C-label; F: oleate pool at t = 6 h, 24 h, 48 h or 72 h of cells grown in lipid depleted medium; G: fractions (A, B, D, E) are shown as unlabelled or m+n, where n corresponds to the number of ^{13}C labels derived from glucose that were incorporated; Cells were cultured in respective media for 72 hours, and metabolite levels were normalized to cell counts as well as an internal

standard. Metabolite pools (C, F) were determined by combining the peak areas (AUC) of each fraction of oleate normalized to internal standard and cell counts

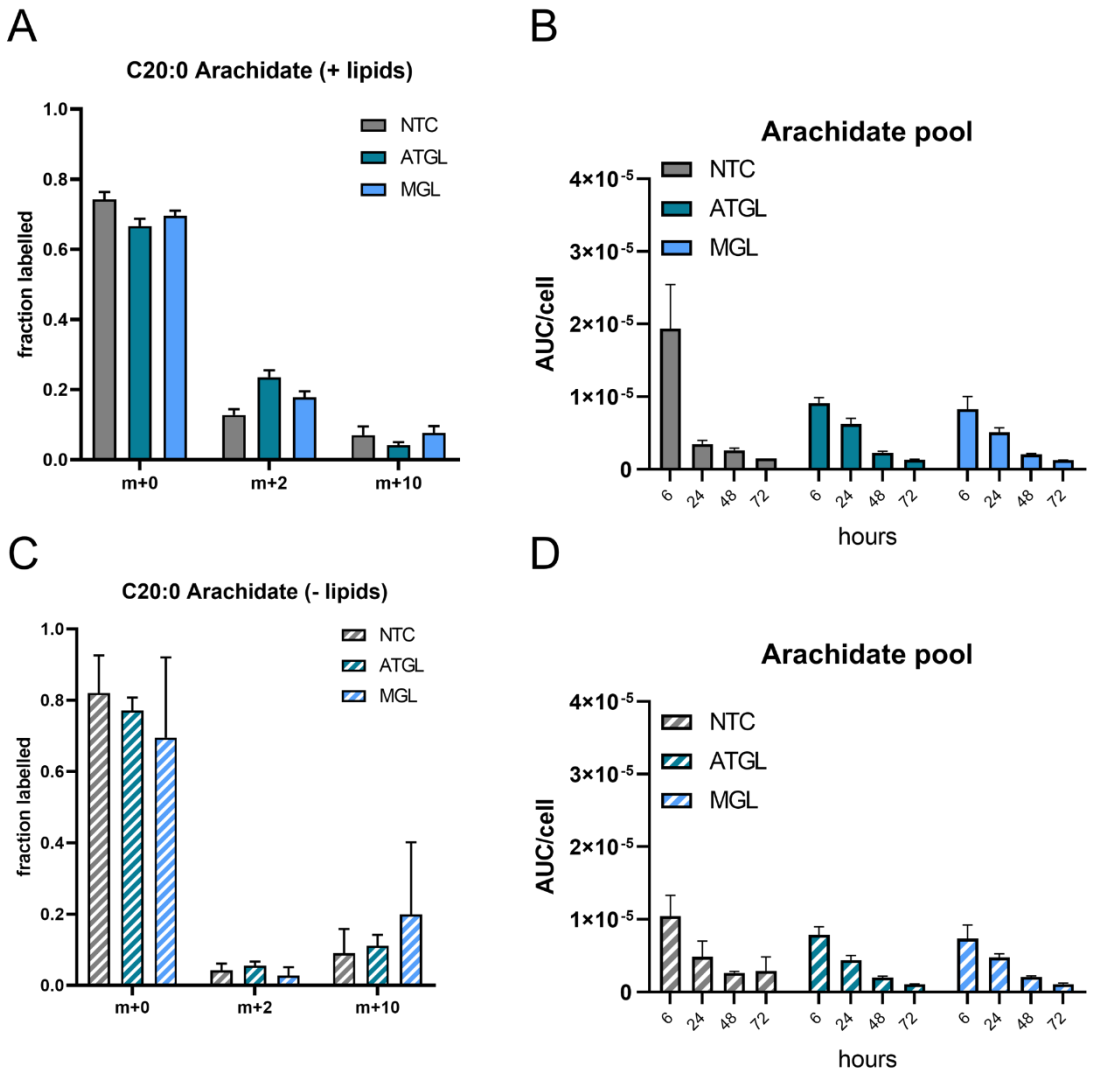

Appendix. Figure 33: metabolic tracing data of uniformly ^{13}C-labelled glucose into arachidate in A549 (Cas9) cell lines. A: the fraction of measured arachidate containing no ^{13}C-label and thus is not derived from glucose, cells grown in regular (lipid containing) medium and distribution of fractions of arachidate with increasing amount of ^{13}C-label, cells grown in regular (lipid containing) medium; B: arachidate pool at t = 6 h, 24 h, 48 h or 72 h of cells grown in regular (lipid containing) medium; C: the fraction of measured arachidate containing no ^{13}C-label and thus is not derived from glucose, cells grown in lipid depleted medium and distribution of fractions of arachidate with increasing amount of ^{13}C-label; D: arachidate pool at t = 6 h, 24 h, 48 h or 72 h of cells grown in lipid depleted

medium. Fractions (A, C) are shown as unlabelled or m+n, where n corresponds to the number of ^{13}C labels derived from glucose that were incorporated; Cells were cultured in respective media for 72 hours, and metabolite levels were normalized to cell counts as well as an internal standard. Metabolite pools (B, D) were determined by combining the peak areas (AUC) of each fraction of arachidate normalized to internal standard and cell counts

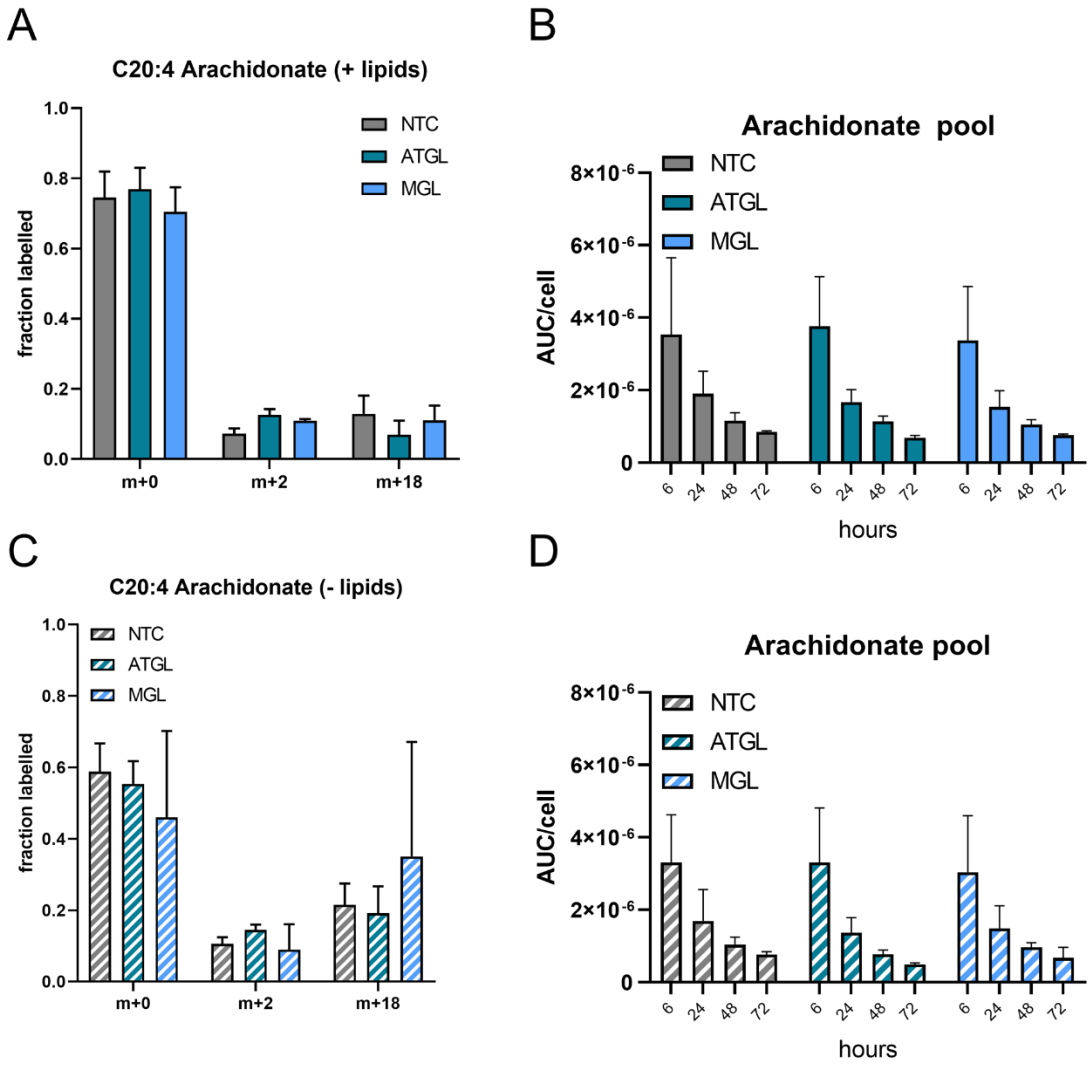

Appendix. Figure 34: metabolic tracing data of uniformly ^{13}C-labelled glucose into arachidonate in A549 (Cas9) cell lines. A: the fraction of measured arachidonate containing no ^{13}C-label and thus is not derived from glucose, cells grown in regular (lipid containing) medium and distribution of fractions of arachidonate with increasing amount of ^{13}C-label, cells grown in regular (lipid containing) medium; B: arachidonate pool at t = 6

h, 24 h, 48 h or 72 h of cells grown in regular (lipid containing) medium; C: the fraction of measured arachidonate containing no ^{13}C-label and thus is not derived from glucose, cells grown in lipid depleted medium and distribution of fractions of arachidonate with increasing amount of ^{13}C-label; D: arachidonate pool at t = 6 h, 24 h, 48 h or 72 h of cells grown in lipid depleted medium. Fractions (A, C) are shown as unlabelled or m+n, where n corresponds to the number of ^{13}C labels derived from glucose that were incorporated; Cells were cultured in respective media for 72 hours, and metabolite levels were normalized to cell counts as well as an internal standard. Metabolite pools (B, D) were determined by combining the peak areas (AUC) of each fraction of arachidonate normalized to internal standard and cell counts

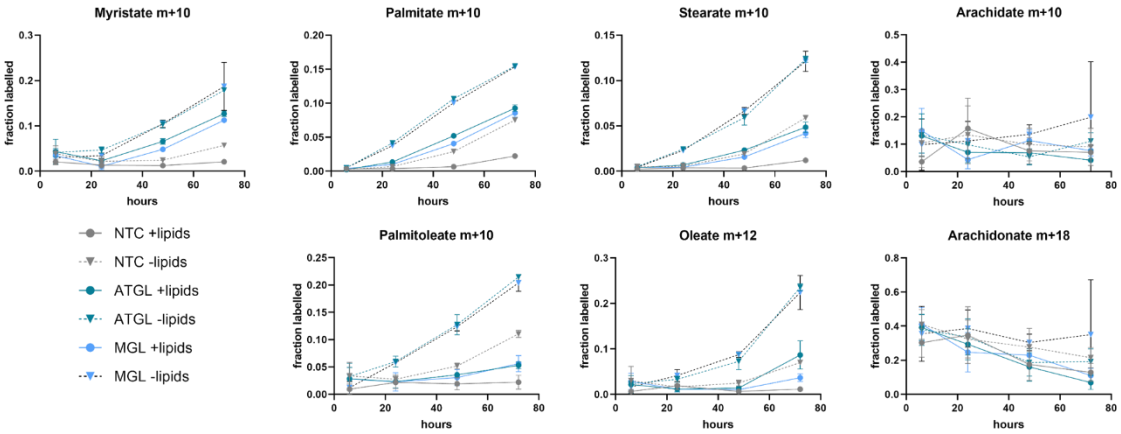

Appendix. Figure 35: metabolic tracing data of uniformly ^{13}C-labelled glucose into myristate, palmitate, stearate, arachidate, palmitoleate, oleate and arachidonate. Depicted are one fraction (m+n, where n is the number of carbon atoms derived from labelled glucose) per each fatty acid species over the period of 72 h in each of the different cell lines (A549 (Cas9) NTC (grey), ATGL-KO (dark blue), MGL-KO (light blue)) and culture conditions (+ lipids, full lines; - lipids, dashed lines)

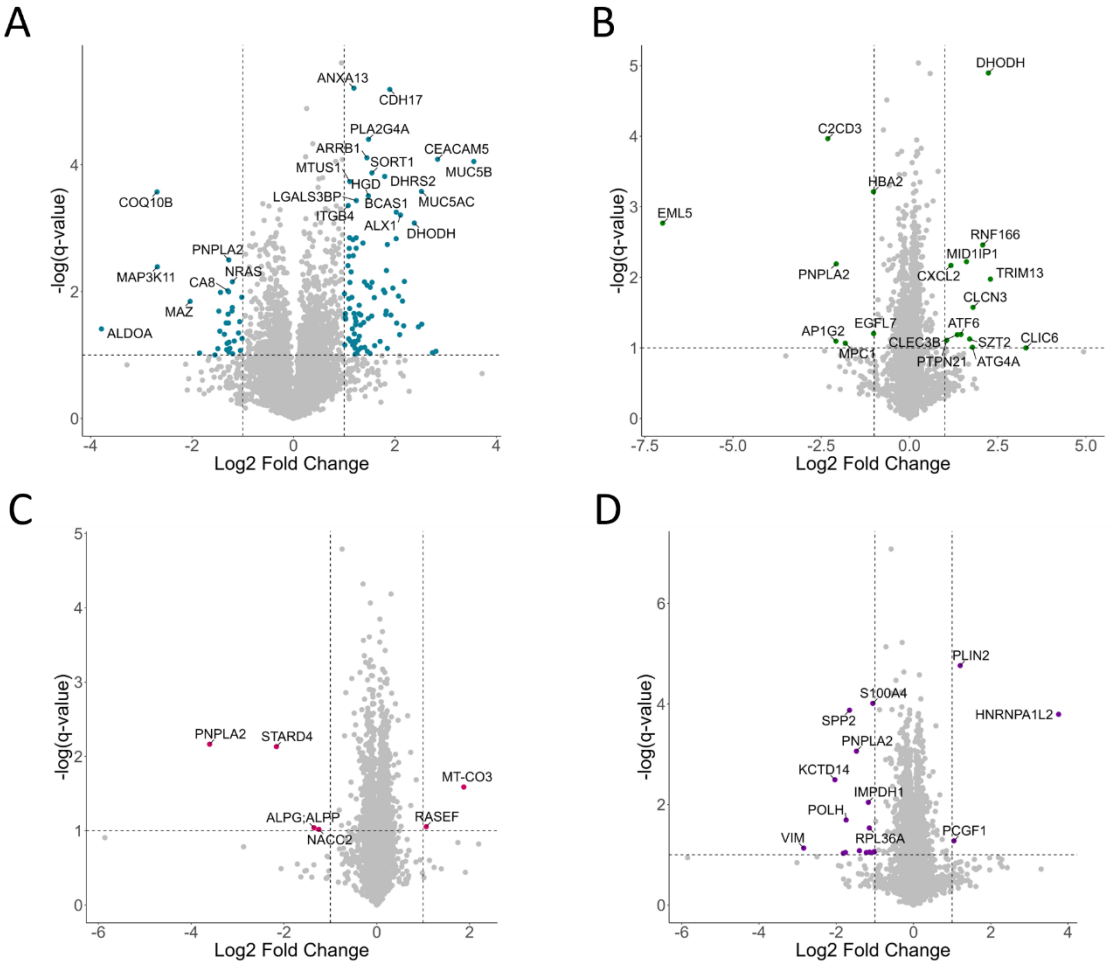

Appendix. Figure 36: LFQ shotgun proteomics of NSCLC cell lines (2D (Cas9) polyclonal cell lines) ATGL-KO vs. NTC – volcano plots. Data were filtered to contain proteins with at least 3 valid values in at least one group (ATGL-KO or Control), proteins in the upper left-hand corners of volcano plots are higher in Controls, proteins in the upper right-hand corners of volcano plots are higher in ATGL-KO cells. A: A549 ATGL-KO vs. Control; B: H1299 ATGL-KO vs. Control; C: H358 ATGL-KO vs. Control; D: H441 ATGL-KO vs. Control

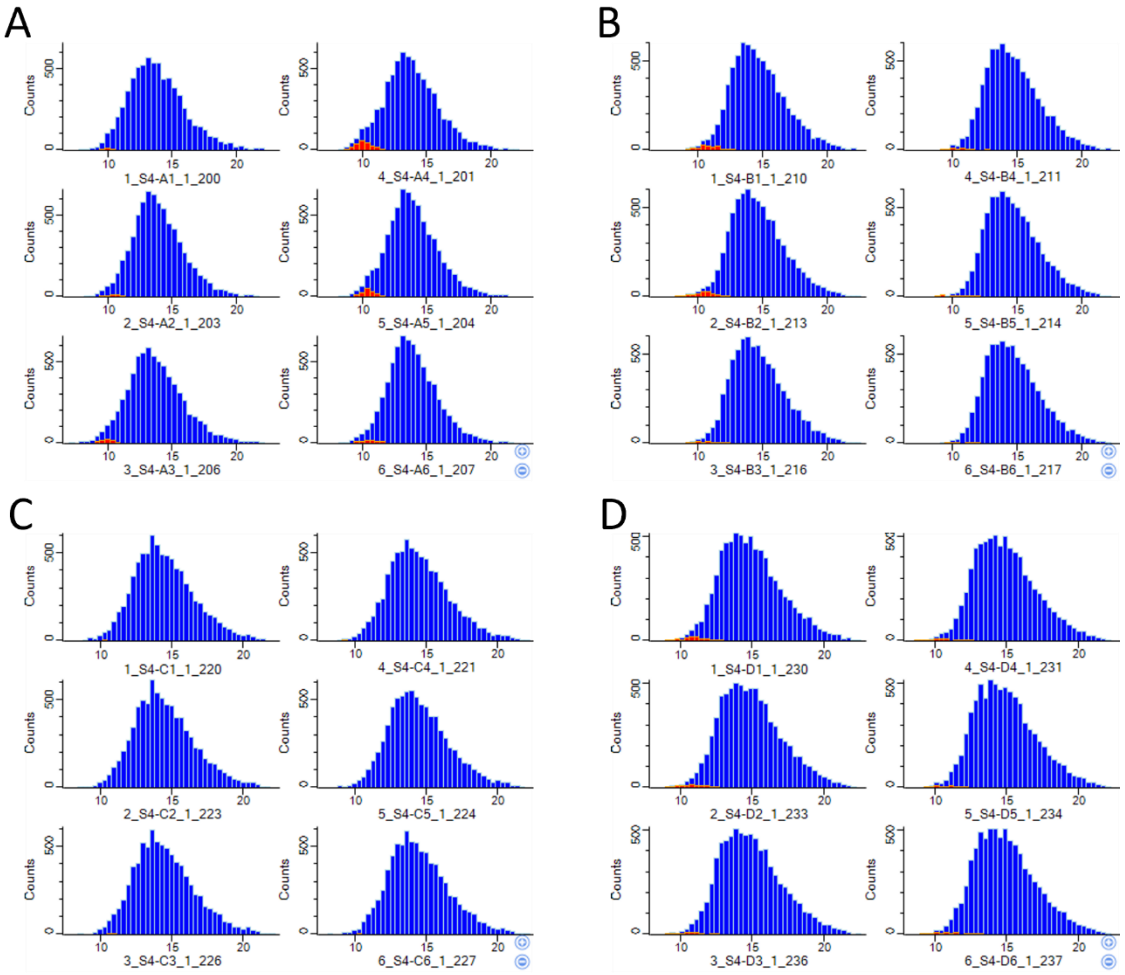

Appendix. Figure 37: LFQ shotgun proteomics of NSCLC cell lines (2D (Cas9) polyclonal cell lines) ATGL-KO vs. NTC – histograms. Samples filtered for proteins with at least 3 valid values in at least one group (ATGL-KO or Control), missing values imputed from normal distribution with 0.3 width and 1.8 downshift

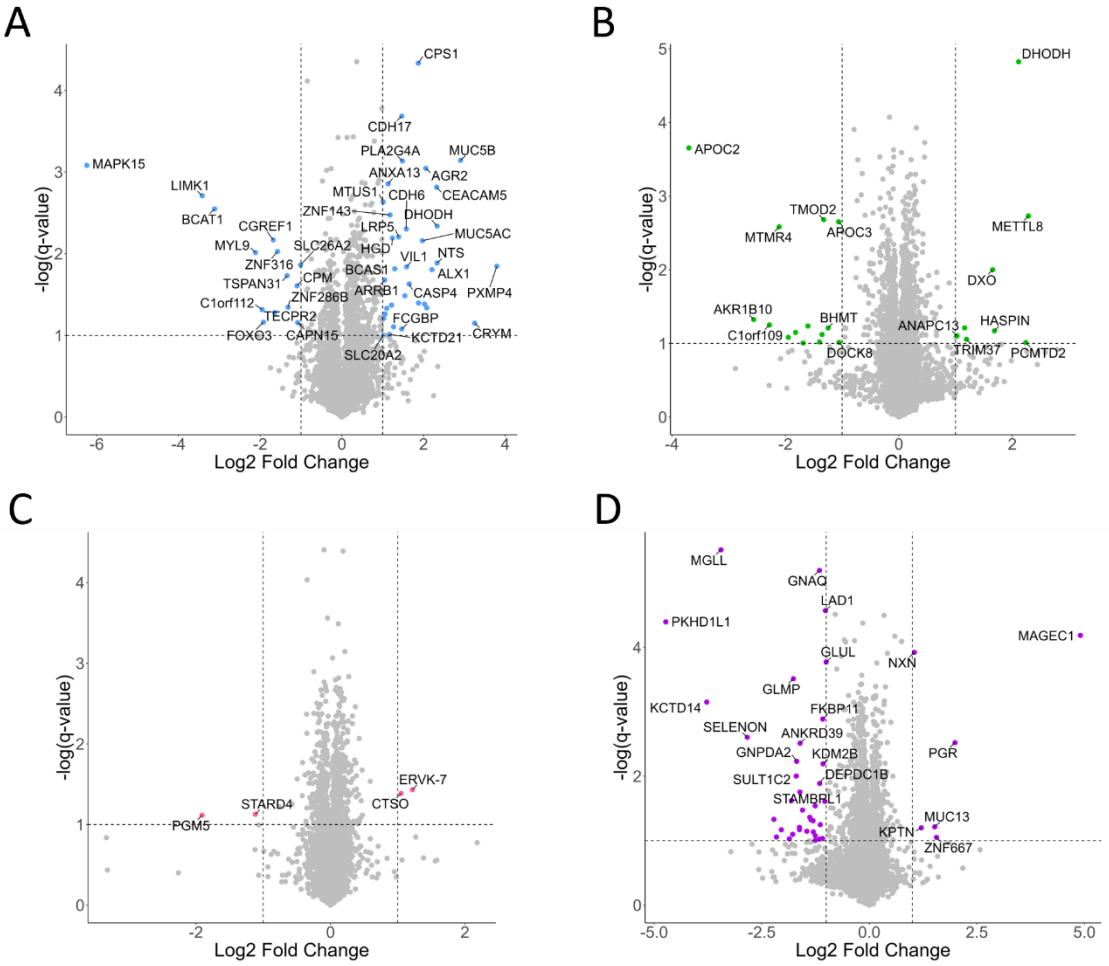

Appendix. Figure 38: LFQ shotgun proteomics of NSCLC cell lines (2D (Cas9) polyclonal cell lines) MGL-KO vs. NTC – volcano plots. Data were filtered to contain proteins with at least 3 valid values in at least one group (MGL-KO or Control), proteins in the upper left-hand corners of volcano plots are higher in Controls, proteins in the upper right-hand corners of volcano plots are higher in MGL-KO cells. A: A549 MGL-KO vs. Control; B: H1299 MGL-KO vs. Control; C: H358 MGL-KO vs. Control; D: H441 MGL-KO vs. Control

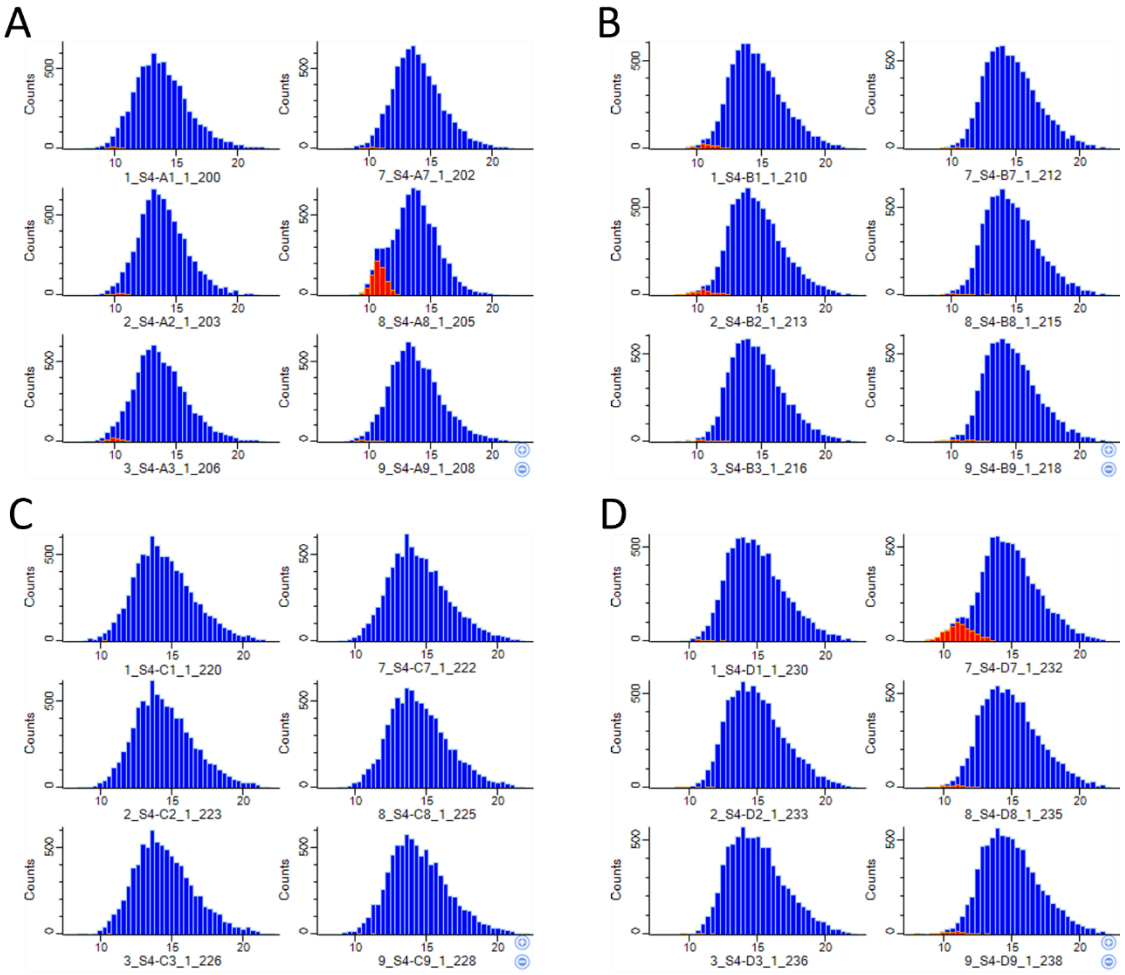

Appendix. Figure 39: LFQ shotgun proteomics of NSCLC cell lines (2D (Cas9) polyclonal cell lines) MGL-KO vs. NTC – histograms. Samples filtered for proteins with at least 3 valid values in at least one group (MGL-KO or Control), missing values imputed from normal distribution with 0.3 width and 1.8 downshift

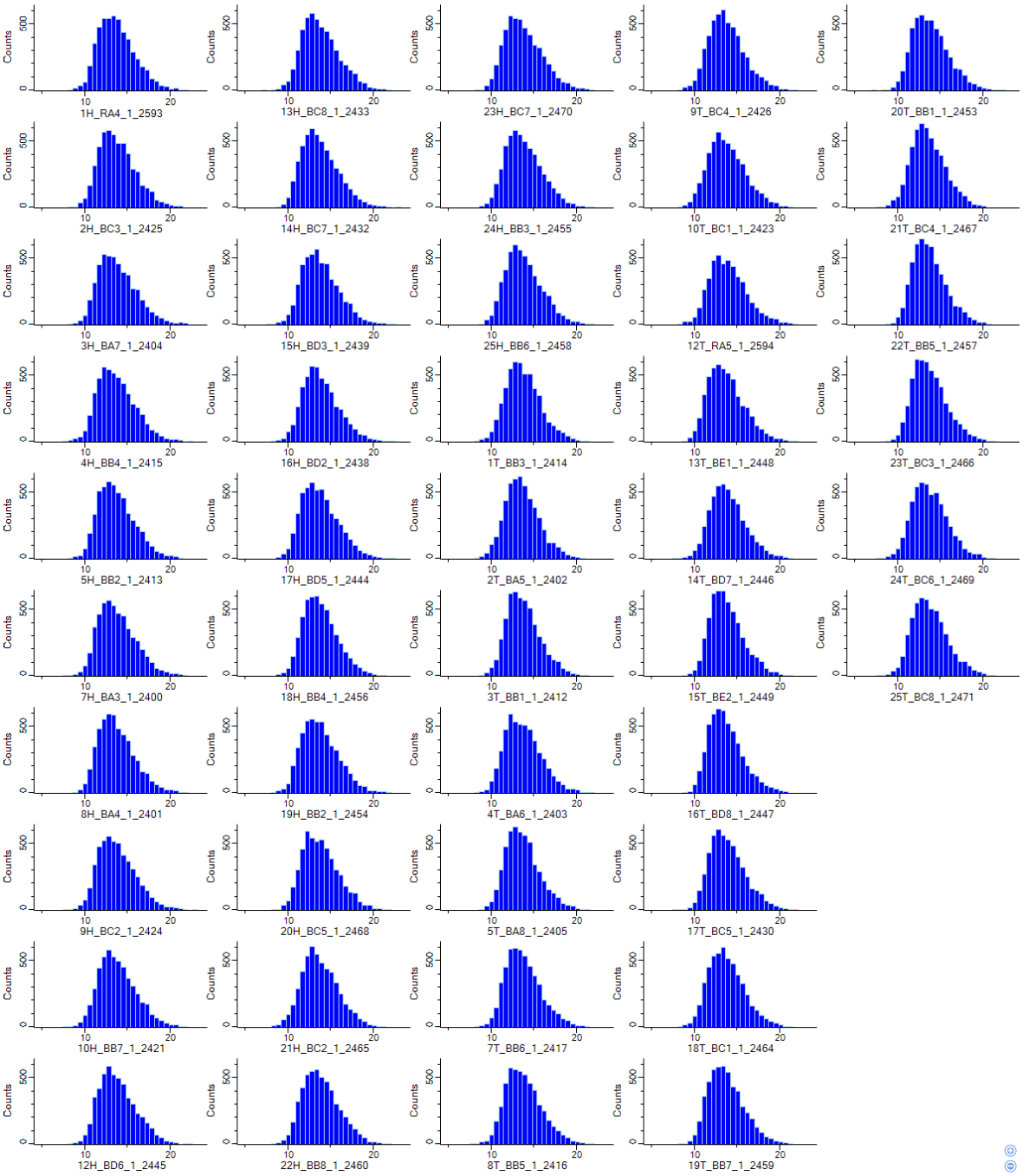

Appendix. Figure 40: LFQ shotgun proteomics of Tumors (T) and Normal Tumor-Adjacent (NTA) samples from NSCLC patients – histograms. Samples filtered for proteins with at least 90 % valid values, no imputation (DIA data)

Table 6: LFQ shotgun proteomics of Tumors (T) and Normal Tumor-Adjacent (NTA) samples from NSCLC patients, string functional enrichment analysis of all proteins submitted with their corresponding fold change between T and NTA: list of first 50 enriched Biological Processes GO terms (based on enrichment score); top = upregulated in tumors, bottom = downregulated in tumors

#term ID	term description	genes mapped	enrichment score	direction	FDR
GO:1902975	Mitotic DNA replication initiation	3	5.67	top	2.20E-04
GO:0000727	Double-strand break repair via break-induced replication	6	5.64	top	1.37E-06
GO:0006267	Pre-replicative complex assembly involved in nuclear cell cycle DNA replication	6	5.64	top	1.37E-06
GO:0055129	L-proline biosynthetic process	5	5.40	top	1.37E-06
GO:0015669	Gas transport	8	5.27	bottom	1.37E-06
GO:1902969	Mitotic DNA replication	5	4.81	top	1.57E-05
GO:0020027	Hemoglobin metabolic process	4	4.75	bottom	1.70E-03
GO:0006270	DNA replication initiation	7	4.50	top	1.37E-06
GO:0010885	Regulation of cholesterol storage	5	4.21	bottom	1.20E-03
GO:0015701	Bicarbonate transport	10	4.13	bottom	4.74E-06
GO:0001765	Membrane raft assembly	8	4.04	bottom	4.39E-05
GO:0006271	DNA strand elongation involved in DNA replication	7	4.02	top	1.22E-05
GO:0019511	Peptidyl-proline hydroxylation	8	3.85	top	5.78E-06
GO:0019433	Triglyceride catabolic process	6	3.83	bottom	8.80E-04
GO:0018401	Peptidyl-proline hydroxylation to 4-hydroxy-L-proline	6	3.77	top	1.90E-04
GO:0045916	Negative regulation of complement activation	7	3.74	bottom	4.40E-04
GO:1900264	Positive regulation of DNA-directed DNA polymerase activity	5	3.41	top	2.40E-03
GO:0033260	Nuclear DNA replication	19	3.40	top	1.37E-06
GO:0051004	Regulation of lipoprotein lipase activity	7	3.32	bottom	1.60E-03
GO:0044786	Cell cycle DNA replication	20	3.32	top	1.37E-06
GO:0072010	Glomerular epithelium development	7	3.25	bottom	2.50E-03
GO:0031581	Hemidesmosome assembly	9	3.16	bottom	5.00E-04
GO:0071711	Basement membrane organization	15	3.14	bottom	4.74E-06
GO:0033700	Phospholipid efflux	7	3.12	bottom	4.10E-03
GO:0034371	Chylomicron remodeling	7	3.08	bottom	4.70E-03
GO:0031664	Regulation of lipopolysaccharide-mediated signaling pathway	7	3.03	bottom	5.90E-03
GO:0022616	DNA strand elongation	10	2.97	top	7.86E-05
GO:0010875	Positive regulation of cholesterol efflux	8	2.93	bottom	4.00E-03
GO:0043691	Reverse cholesterol transport	9	2.91	bottom	1.30E-03
GO:0006465	Signal peptide processing	6	2.88	top	4.70E-03

GO:0007263	Nitric oxide mediated signal transduction	8	2.82	bottom	5.60E-03
GO:0032835	Glomerulus development	12	2.81	bottom	2.70E-04
GO:0033344	Cholesterol efflux	12	2.81	bottom	2.70E-04
GO:0002921	Negative regulation of humoral immune response	9	2.81	bottom	2.10E-03
GO:0006067	Ethanol metabolic process	10	2.79	bottom	9.20E-04
GO:0032376	Positive regulation of cholesterol transport	10	2.79	bottom	9.70E-04
GO:0042744	Hydrogen peroxide catabolic process	17	2.76	bottom	1.22E-05
GO:0018126	Protein hydroxylation	13	2.73	top	2.31E-05
GO:0035633	Maintenance of blood-brain barrier	16	2.67	bottom	4.24E-05
GO:0006641	Triglyceride metabolic process	21	2.60	bottom	6.12E-06
GO:0034375	High-density lipoprotein particle remodeling	10	2.60	bottom	2.80E-03
GO:0072009	Nephron epithelium development	17	2.59	bottom	3.83E-05
GO:0034369	Plasma lipoprotein particle remodeling	13	2.55	bottom	5.00E-04
GO:0000463	Maturation of LSU-rRNA from tricistronic rRNA transcript (SSU-rRNA, 5.8S rRNA, LSU-rRNA)	9	2.52	top	1.40E-03
GO:0071709	Membrane assembly	16	2.50	bottom	1.40E-04
GO:0032201	Telomere maintenance via semi-conservative replication	12	2.48	top	2.40E-04
GO:0042730	Fibrinolysis	13	2.45	bottom	9.20E-04
GO:0018149	Peptide cross-linking	12	2.45	both ends	3.90E-04
GO:0007597	Blood coagulation, intrinsic pathway	11	2.42	bottom	3.10E-03
GO:0032374	Regulation of cholesterol transport	19	2.42	bottom	3.88E-05

Table 7: LFQ shotgun proteomics of Tumors (T) and Normal Tumor-Adjacent (NTA) samples from NSCLC patients, string functional enrichment analysis of all proteins submitted with their corresponding fold change between T and NTA: list of first 50 enriched KEGG Pathways (based on enrichment score); top = upregulated in tumors, bottom = downregulated in tumors

#term ID	**term description**	**genes mapped**	**enrichment score**	**direction**	**FDR**
hsa03030	DNA replication	20	3.27	top	5.82E-07
hsa00512	Mucin type O-glycan biosynthesis	4	3.13	top	6.40E-03
hsa04512	ECM-receptor interaction	44	2.70	bottom	5.19E-10
hsa04640	Hematopoietic cell lineage	23	2.46	bottom	4.18E-06
hsa05320	Autoimmune thyroid disease	11	2.43	bottom	1.10E-03
hsa05330	Allograft rejection	11	2.43	bottom	1.10E-03
hsa05332	Graft-versus-host disease	11	2.43	bottom	1.10E-03
hsa03430	Mismatch repair	13	2.33	top	1.20E-04

hsa05310	Asthma	10	2.26	bottom	4.80E-03
hsa04975	Fat digestion and absorption	12	2.25	bottom	1.50E-03
hsa04964	Proximal tubule bicarbonate reclamation	9	2.24	bottom	8.50E-03
hsa04080	Neuroactive ligand-receptor interaction	14	2.16	bottom	8.60E-04
hsa04940	Type I diabetes mellitus	12	2.08	bottom	3.90E-03
hsa03060	Protein export	19	2.04	top	5.64E-05
hsa05032	Morphine addiction	19	2.01	bottom	3.80E-04
hsa04610	Complement and coagulation cascades	56	1.97	bottom	1.24E-13
hsa04924	Renin secretion	25	1.89	bottom	5.63E-05
hsa04713	Circadian entrainment	28	1.88	bottom	9.31E-08
hsa04979	Cholesterol metabolism	23	1.87	bottom	9.30E-04
hsa03320	PPAR signaling pathway	32	1.86	bottom	4.99E-05
hsa00982	Drug metabolism - cytochrome P450	16	1.86	bottom	2.20E-03
hsa04976	Bile secretion	14	1.80	bottom	5.20E-03
hsa05143	African trypanosomiasis	17	1.79	bottom	2.40E-03
hsa04971	Gastric acid secretion	25	1.71	bottom	2.56E-05
hsa05416	Viral myocarditis	29	1.66	bottom	1.22E-05
hsa04510	Focal adhesion	107	1.61	bottom	6.95E-11
hsa04514	Cell adhesion molecules	44	1.59	bottom	1.30E-06
hsa03008	Ribosome biogenesis in eukaryotes	35	1.56	top	2.63E-05
hsa05150	Staphylococcus aureus infection	31	1.55	bottom	5.54E-06
hsa04726	Serotonergic synapse	36	1.54	bottom	3.18E-07
hsa05204	Chemical carcinogenesis	18	1.54	bottom	6.40E-03
hsa03010	Ribosome	106	1.50	top	1.48E-27
hsa04725	Cholinergic synapse	33	1.49	bottom	7.88E-06
hsa00071	Fatty acid degradation	29	1.44	bottom	4.85E-06
hsa04270	Vascular smooth muscle contraction	50	1.43	bottom	3.88E-07
hsa05146	Amoebiasis	52	1.38	bottom	6.07E-06
hsa05414	Dilated cardiomyopathy	32	1.33	bottom	1.40E-03
hsa04925	Aldosterone synthesis and secretion	25	1.32	bottom	6.90E-04
hsa04970	Salivary secretion	29	1.30	bottom	5.64E-05
hsa05410	Hypertrophic cardiomyopathy	34	1.30	bottom	7.80E-03
hsa03013	RNA transport	105	1.26	top	7.11E-20
hsa03018	RNA degradation	43	1.26	top	4.66E-06
hsa04730	Long-term depression	30	1.25	bottom	2.70E-04
hsa04916	Melanogenesis	24	1.24	bottom	3.30E-03
hsa03015	mRNA surveillance pathway	56	1.24	top	3.01E-06
hsa04961	Endocrine and other factor-regulated calcium reabsorption	25	1.23	bottom	2.64E-05
hsa04724	Glutamatergic synapse	33	1.22	bottom	2.42E-05
hsa00330	Arginine and proline metabolism	27	1.22	both ends	7.40E-03
hsa04540	Gap junction	41	1.21	bottom	8.97E-05
hsa04670	Leukocyte transendothelial migration	58	1.17	bottom	7.84E-05

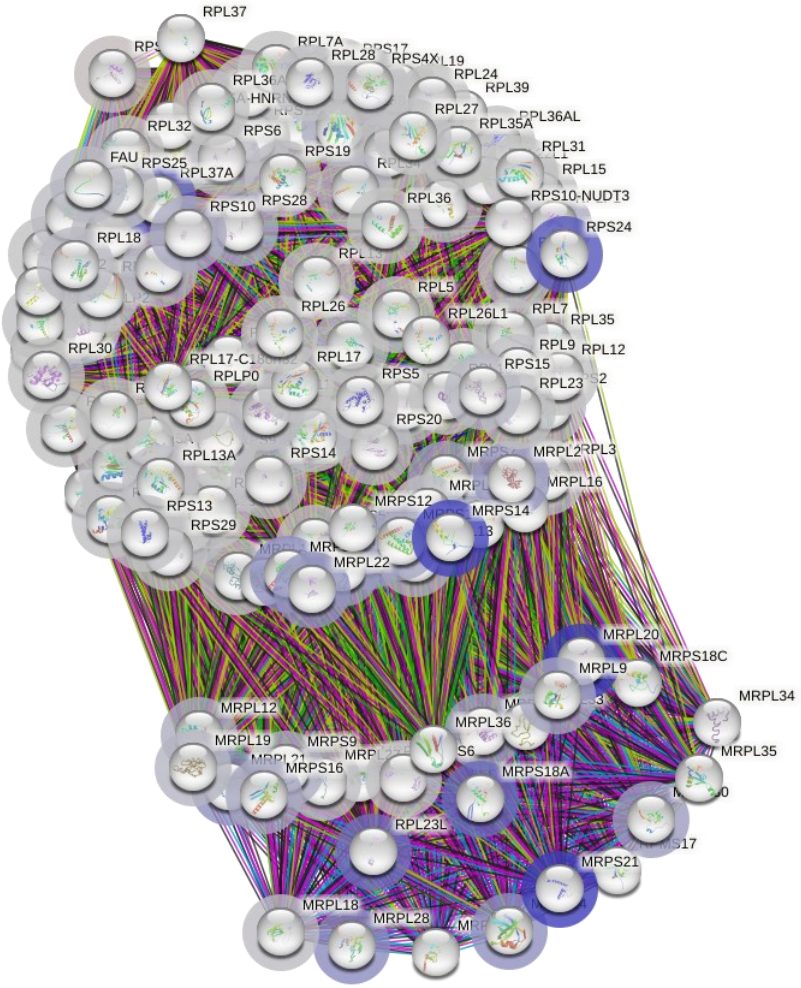

Appendix. Figure 41: LFQ shotgun proteomics of Tumors (T) and Normal Tumor-Adjacent (NTA) samples from NSCLC patients, string functional enrichment analysis: Ribosome KEGG pathway (hsa03010): upregulated in tumor; enrichment score: 1.49517; pathway size: 130; FDR: 1.48e-27

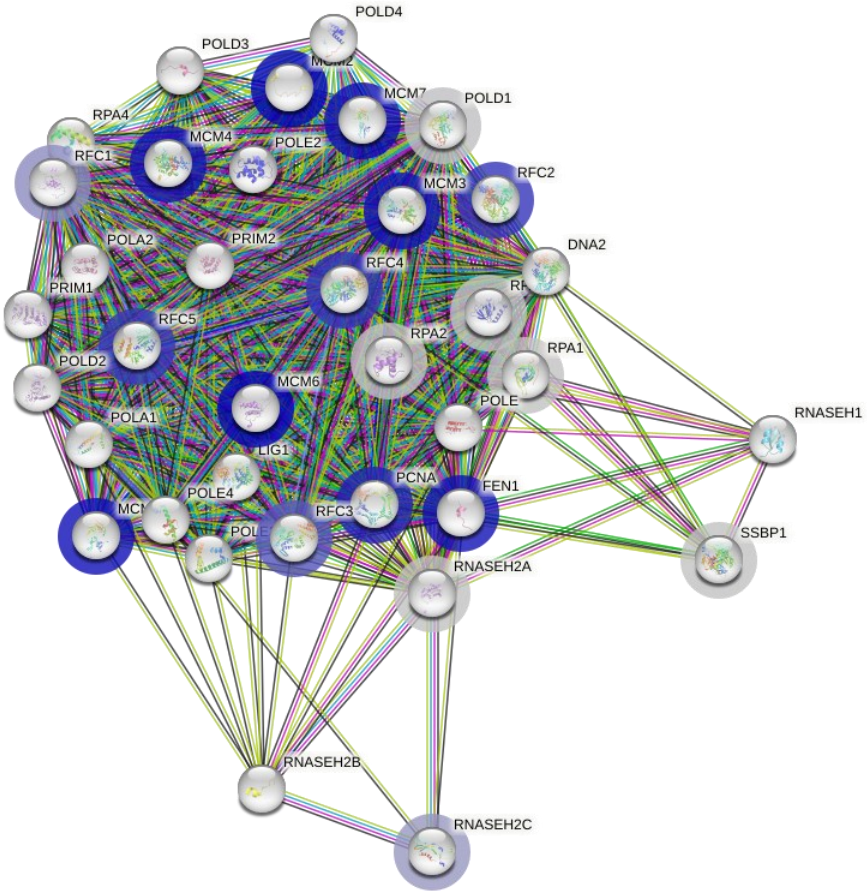

Appendix. Figure 42: LFQ shotgun proteomics of Tumors (T) and Normal Tumor-Adjacent (NTA) samples from NSCLC patients, string functional enrichment analysis: DNA replication KEGG pathway (hsa03030): up in tumor; enrichment score: 3.27354; pathway size: 36; FDR: 5.82e-07

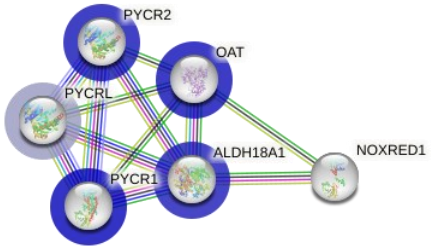

Appendix. Figure 43: LFQ shotgun proteomics of Tumors (T) and Normal Tumor-Adjacent (NTA) samples from NSCLC patients, string functional enrichment analysis: L-proline biosynthetic process (GO:0055129): upregulated in tumors; enrichment score: 5.39639; pathway size: 6; FDR: 1.37e-06

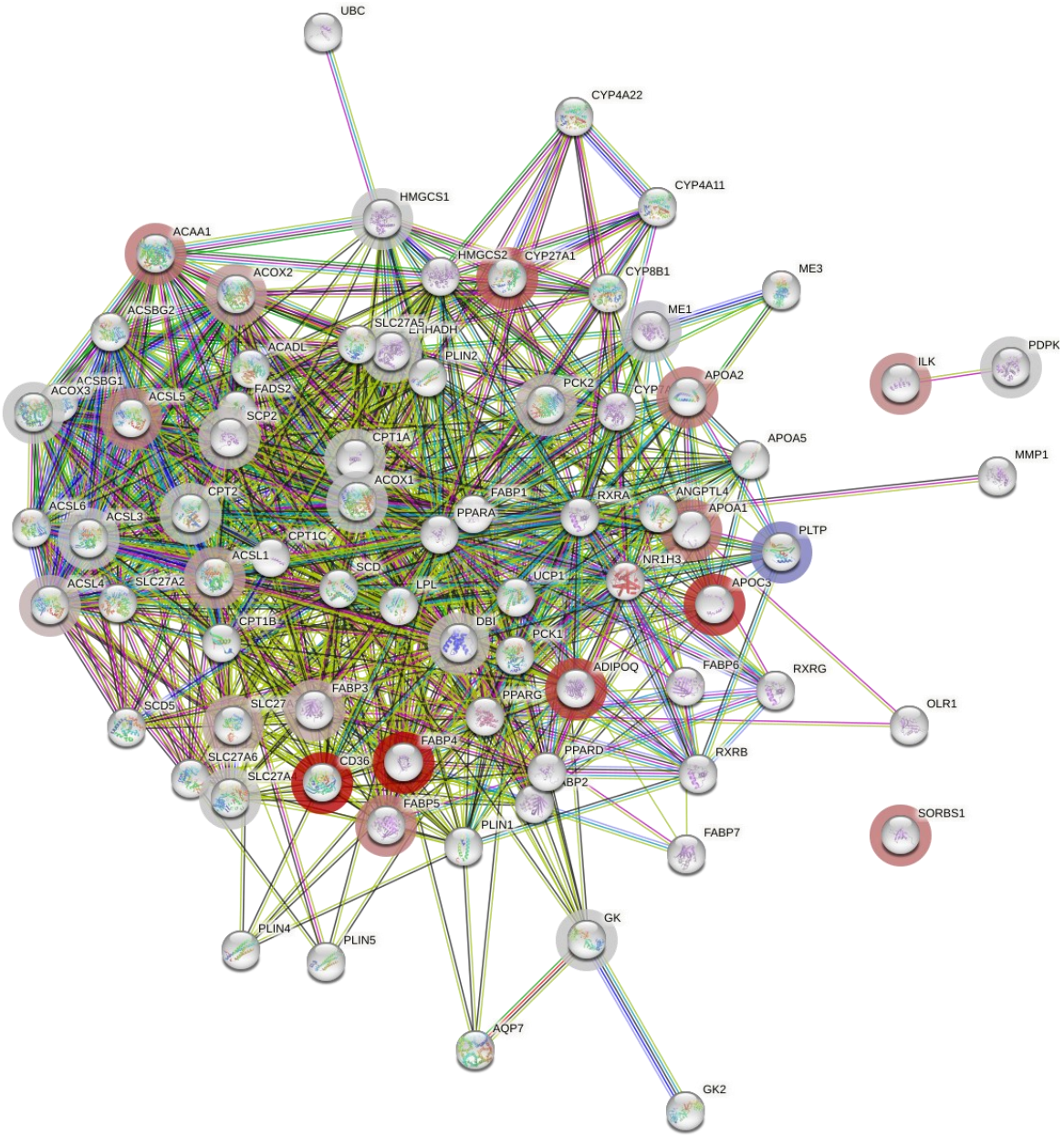

Appendix. Figure 44: LFQ shotgun proteomics of Tumors (T) and Normal Tumor-Adjacent (NTA) samples from NSCLC patients, string functional enrichment analysis: PPAR signaling pathway (hsa03320): low in tumor; enrichment score: 1.8568; pathway size:75; FDR: 4.99e-05

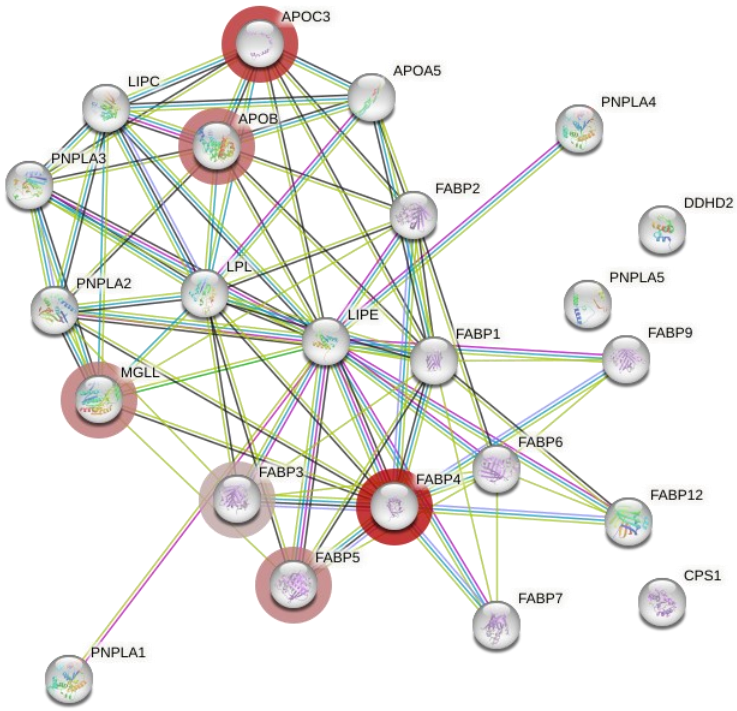

Appendix. Figure 45: LFQ shotgun proteomics of Tumors (T) and Normal Tumor-Adjacent (NTA) samples from NSCLC patients, string functional enrichment analysis: Triglyceride catabolic process (GO:0019433): downregulated in tumor; enrichment score: 3.83168; pathway size: 23; FDR: 0.00088

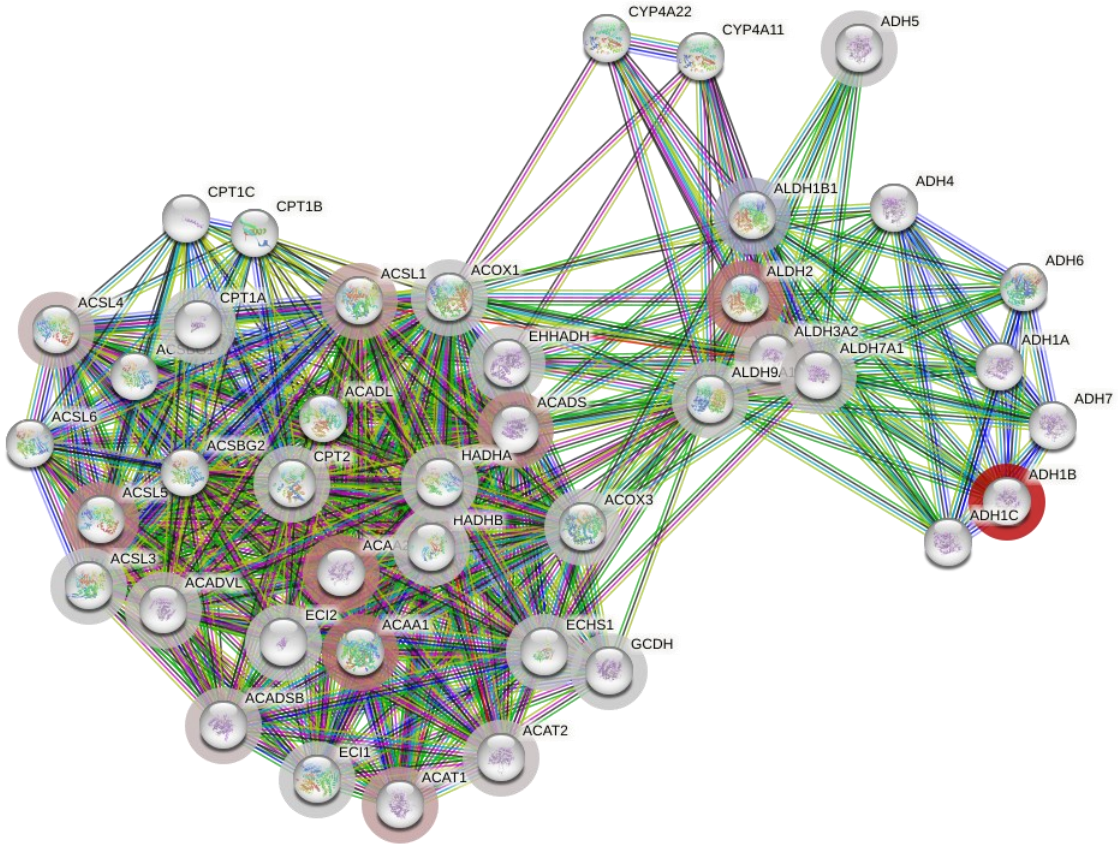

Appendix. Figure 46: LFQ shotgun proteomics of Tumors (T) and Normal Tumor-Adjacent (NTA) samples from NSCLC patients, string functional enrichment analysis: Fatty Acid Degradation KEGG pathway (hsa00071): downregulated in tumor; enrichment score: 1.44015; pathway size: 42; FDR: 4.85e-06

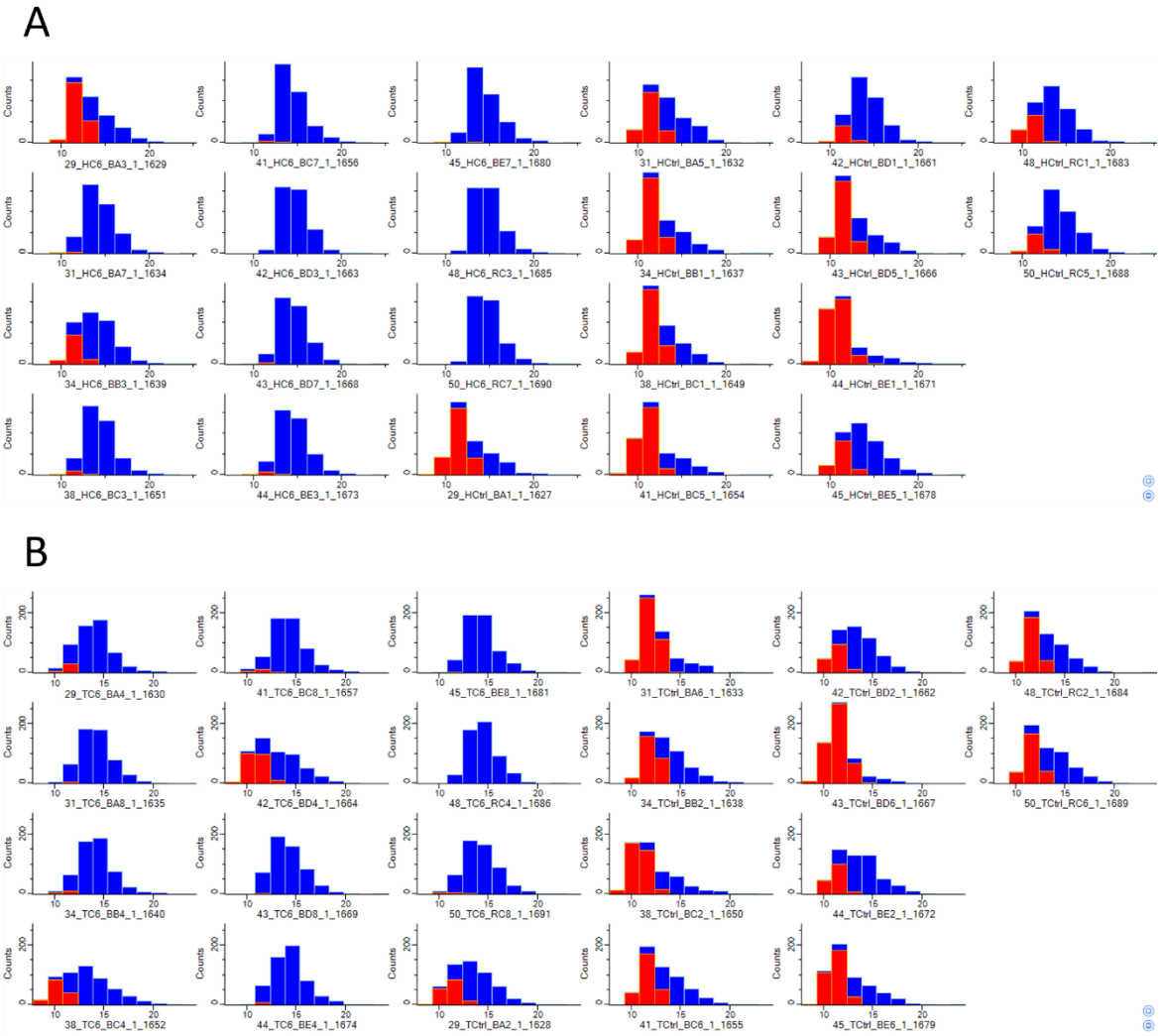

Appendix. Figure 47: activity-based proteomic profiling data of NSCLC patients – histograms. A: Normal Tumor-Adjacent (NTA) samples (ABP and Control); B: Tumor (T) samples (ABP and Control); both groups were filtered for proteins with at least 9 valid values (out of 11 in at least one group – Control or ABP) –missing values imputed from normal distribution with a downward shift of 1.6 and width of 0.4

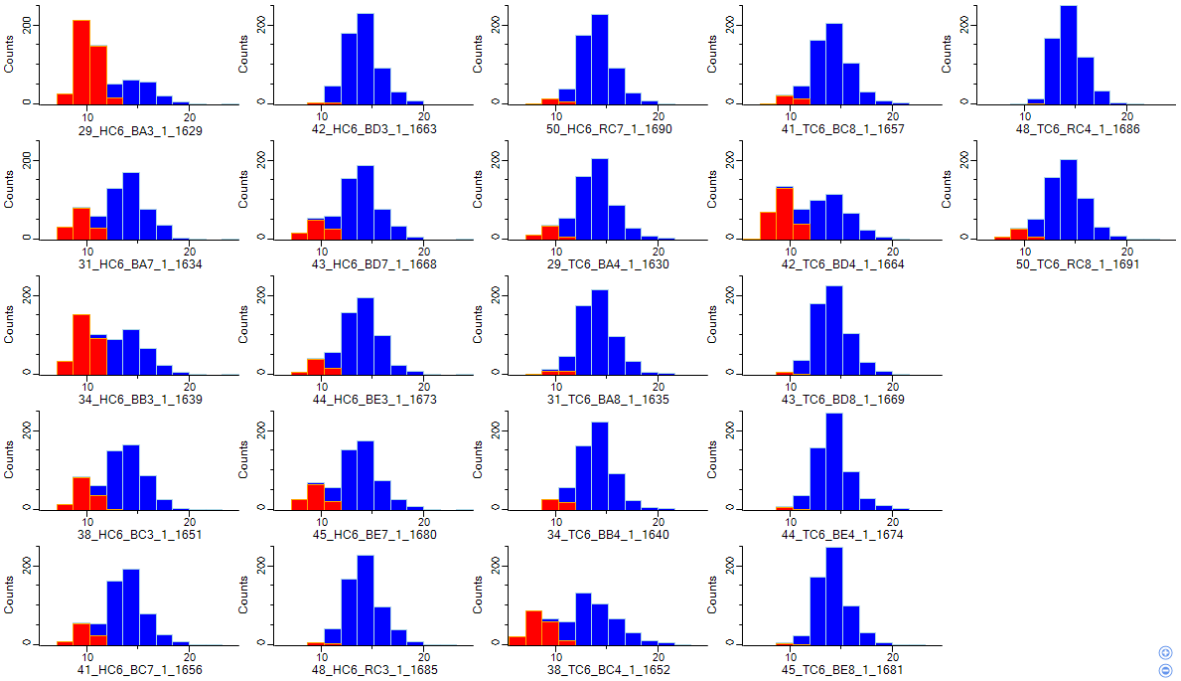

Appendix. Figure 48: activity-based proteomic profiling data of NSCLC patients – histograms. Normal Tumor-Adjacent (NTA) and Tumor (T) ABP samples filtered for proteins with at least 9 valid values (out of 11 in at least one group – NTA or T) – missing values imputed from normal distribution with a downward shift of 2.5 and width of 0.5